Tomografía muónica de alta resolución aplicada a la evaluación de la densidad de materiales en el contexto de la industria, la ingeniería civil y la hidrología

Tesis presentada por **Aitor Orio Alonso**
a la Universidad de Cantabria
para la obtención del grado de
Doctor
y supervisada por
Pablo Martínez Ruiz del Árbol
y **Pablo Gómez García**

Muon Tomography Systems
Instituto de Física de Cantabria (IFCA) - Universidad de Cantabria (UC)

Santander, noviembre 2023

High resolution scattering muography applied to material density assessment in the context of the industry, civil engineering and hydrology

Thesis presented by **Aitor Orio Alonso**
to the University of Cantabria for the degree of
Doctor of Philosophy
and supervised by
Pablo Martínez Ruiz del Árbol
and **Pablo Gómez García**

Muon Tomography Systems
Instituto de Física de Cantabria (IFCA) - Universidad de Cantabria (UC)

Santander, November 2023

Nire guraso, arreba, senide, lagun eta bidea nirekin partekatu duzuen guztiei, azken lan urte hauetan batez ere.

Acknowledgements

Lehenik eta behin, eskerrik asko nire senideei, lagunei, eta nire ondoan egon zareten guztiei. Zuen laguntza eta babesa ezinbestekoa izan da, eta egunez egun aurrera egiten lagundu dit.

Sin duda gran parte de culpa de que este trabajo haya salido adelante la tienen mis compañeros de trabajo: Carlos, y los dos Pablos, que además han tenido la valentía de dirigir este doctorado y que desde el principio me han apoyado. Gracias a la empresa por apoyar este proyecto. Sería injusto no destacar el importante apoyo que he recibido por vuestra parte en las diferentes cuestiones técnicas de este trabajo. Carlos, aunque desde la distancia, siempre has estado para ayudarme en cualquier tema. Y los Pablos, cada uno más centrado en su especialidad, en el hardware o en la algoritmia, me habéis aclarado el camino. Muchas gracias por todo. No quiero olvidarme de Aurel, y de la ayuda proporcionada por los demás trabajadores de Denipa con el hardware. Gracias. Esteban, muchas gracias por tu colaboración en la investigación sobre la nieve. Te agradezco tu ayuda con los experimentos, su publicación, y todos los consejos que me has dado.

I would like to thank also the people who welcomed me in Louvain-la-Neuve. Thank you Ishan for being there both the first day and the last, as well as throughout all my stay. Thanks to all the friends with whom I have shared my time in Belgium. Thanks to my office mate Vishal for helping me with the accomodation, and for the interesting discussions. Thank you Andrea for managing and coordinating my scientific stay, I am very grateful. Maxime, your help and intense collaboration have been indispensable in the work developed for the TomOpt project. I do not want to forget the other collaborators of TomOpt: Giles, Tomasso, Pietro, Haitham...Thanks to all for your warm welcome and cooperation.

Este proyecto de doctorado ha sido cofinanciado por el Ministerio de Ciencia e Innovación a través del programa “Ayudas para contratos para la formación de doctores en empresas (Doctorados Industriales) 2018” (Referencia de la subvención: DIN2018-009886). Un sincero agradecimiento por el apoyo prestado. Gracias también a la Universidad de Cantabria por la formación y ayuda durante este doctorado. Finalmente, agradecer la disponibilidad de las muestras de hormigón al Grupo de Tecnología de la Edificación de la Universidad de Cantabria (GTED-UC).

Resumen

La tomografía muónica, usualmente conocida en el campo como muografía (muography, en inglés), es una técnica capaz de determinar la distribución de la densidad de la materia, valiéndose de los datos aportados por los muones que la atraviesan. Es posible aplicarla por medio de la atenuación de los muones, pero esta tesis está enfocada en la muografía de scattering. Esta modalidad hace uso del scattering múltiple que sufren los muones para, mediante la medición de sus desviaciones, inferir las propiedades del material atravesado. Por ello, y en comparación con la modalidad de absorción, la muografía de scattering es idónea en aplicaciones sobre objetivos de dimensiones más limitadas y que requieren una mayor resolución.

En la aplicación de la tomografía muónica resulta indispensable la comprensión profunda del funcionamiento de los detectores de muones utilizados. Además, su correcta calibración y puesta a punto son factores de suma importancia. En esta tesis se analiza el diseño de detectores basados en cámaras multi-hilo (MWPCs, por sus siglas en inglés), en concreto los desarrollados y construidos por la empresa Muon Systems. Se explica también el procedimiento utilizado para la reconstrucción de eventos y se estudian las eficiencias y resolución de los detectores, entre otros aspectos.

Desde la introducción de la radiografía de muones a principios de la década de 1950, tanto la absorción como la desviación de los muones se han utilizado para mapear la densidad de estructuras de diferente naturaleza. En esta tesis, se presentan estudios de viabilidad de la detección de objetivos específicos en diversos contextos. Se exponen resultados de experimentos y análisis relacionados con el ámbito de la industria, la ingeniería civil, y la hidrología. En el desarrollo de las investigaciones han sido de suma importancia la puesta a punto y calibración de los detectores de muones, así como la implementación y validación de los algoritmos utilizados para reconstruir las propiedades del material de los objetivos. De esta manera, la tomografía muónica ha sido desarrollada con el objetivo de resolver nuevas aplicaciones utilizando enfoques eficientes, efectivos, e innovadores.

Abstract

Muon tomography, usually referred to in the field as muography, is a technique capable of determining the density distribution of matter using the data provided by the muons passing through it. It can be applied by means of muon attenuation, but this thesis focuses on scattering muography. This modality makes use of the multiple scattering of muons to infer the properties of the material traversed by measuring their deflections. Therefore, compared to absorption, scattering muography is suitable for applications on targets with more limited dimensions and requiring higher resolution.

In the application of muon tomography, a thorough understanding of the functioning of the muon detectors used is indispensable. In addition, their correct calibration and tuning are of utmost importance. In this thesis, the design of detectors based on Multi-Wire Proportional Chambers (MWPCs), specifically those developed and built by Muon Systems, is analysed. The procedure used for event reconstruction is also explained, and the efficiencies and resolution of the detectors are studied, among other aspects.

Since the introduction of muon radiography in the early 1950s, both muon absorption and scattering have been used to map the density of structures of different nature. In this thesis, feasibility studies of the detection of specific targets in various contexts are presented. Results of experiments and analyses related to the fields of industry, civil engineering, and hydrology are presented. In the development of the investigations, the tuning and calibration of the muon detectors, as well as the implementation and validation of the algorithms used to reconstruct the material properties of the targets have been key aspects. Through them, muon tomography has been developed with the aim of solving new applications using efficient, effective, and innovative approaches.

Contents

List of Figures

List of Tables

Chapter 1

Introduction

Muons are elementary particles created when cosmic rays coming from distant regions of the universe collide with the upper atmosphere of the Earth. In these collisions, particle showers are generated and some of them manage to reach the Earth's surface. Among the particles involved in those processes, muons are those producing a larger flux at sea level, and they can even penetrate distances close to 1 Km underground. Muons are deviated due to coulomb scattering and attenuated because of ionisation energy losses when crossing matter. These effects have a strong dependency on the materials crossed, which, together with their constant flux, and their penetration power, make them a suitable source to inspect the internal structure of diverse targets.

Muon Tomography, or Muon Radiography, or also simply synthesised as Muography, is the technique that measures muon deflections and attenuation in order to determine the density distribution of the crossed materials. It is applied in two modalities: transmission muography, in which muon absorption is exploited, and scattering muography, where muon deviations are measured to estimate the scattering undergone by the muons. Transmission muography is usually utilized for very large or ultra-dense targets, while scattering muography is more often used for lower dimension targets, where a higher resolution is needed. Both techniques are being applied nowadays in different fields, including manufacturing industry, civil engineering, archaeology, vulcanology, nuclear energy and recently in hydrology problems.

This work is focused in high resolution scattering muography applied to problems existing in manufacturing industry, hydrology and civil engineering. In this project, a gaseous muon detector based in MWPC (Multi-Wire Proportional Chambers) has been utilised for the exploration of these applications. The detection system is composed of several sensitive planes. These layers are conformed by two cathode planes and a plane of equally-separated wires and immersed in a convenient gas mixture. When a large voltage difference is applied between the wires and the planes, a jail-like electric field is formed pointing to the wires. Particles crossing the sensitive layers ionise the gas, and generate electrons that drift towards the wires producing a detectable signal. This setup, with the corresponding electronic synchronisation and acquisition system, allows to identify and reconstruct muon trajectories. This information is interpreted with the help of algorithms to obtain the final results of the muography, that can be density maps in image format or numerical estimations of parameters of interest describing the target.

The main objective of this work is to improve the resolution and performance of a complete muon tomography system by means of hardware commissioning and fine-tuning. The exploration of innovative applications of muography, is also a key aspect of this work. Research related to hardware and software parts of the muography detector system has been developed, finally applying it to problems which currently exist in the fields mentioned above. The progress made in the studied use cases contribute to the process of making muography a useful tool for society.

All the mentioned work is summarised and reported in this thesis, which is divided into 8 chapters:

- **Chapter 1: Introduction.** This initial chapter, introducing the main ideas of the thesis.
- **Chapter 2: Muon tomography.** Description of the state-of-the-art of the field of muography, beginning with the historical process that yielded to the discovery of cosmic rays and muons, continuing with the nature of muons as elementary particles and their interaction with matter, and finishing with muography concepts: its fundamentals, detection technologies, algorithms, simulation and applications.
- **Chapter 3: Commissioning of a MWPC-based muon detection system.** Section describing the detection system used in this doctorate and its commissioning process. Strategies based on the addition of redundant chambers to improve the final resolution and reconstruction efficiency of the detector are presented. Finally, the calibration of the system, and the application of the aforementioned strategies are discussed.
- **Chapter 4: Detection of cracks in concrete cylinders using scattering muography.** Experiments performed to detect cracks in concrete cylinders are presented. Density estimations are performed within the volume of the cylinders by means of a reconstruction algorithm implemented specifically for such application.
- **Chapter 5: Estimation of the *Snow Water Equivalent* (SWE), based on the root-mean-square of scattering angles.** In this chapter, research performed about the estimation of the SWE using scattering muography is summarised. This work represents, to the best of the authors' knowledge, the first publication about a SWE-based scattering muography.
- **Chapter 6: Estimation of the liquid steel fill level in a ladle furnace using scattering muography.** This chapter proposes an algorithm to determine the fill level of liquid steel in a ladle furnace. The work is presented in the context of the contribution made to the TomOpt software, done in collaboration with other partners. Several inference methods and detector performance loss functions are analysed and proposed for the TomOpt optimisation algorithm.
- **Chapter 7: Conclusions.** Explanation of the main conclusions extracted from this PhD project.
- **Chapter 8: Conclusiones.** Explicación de las principales conclusiones extraídas de este proyecto de doctorado.

Chapter 2

Muon Tomography and its origins

This chapter describes the state of the art of the technology used in this research. It is divided in three different sections. In the first of them (section 2.1), the process of scientific research that lead to the discovery of muons is exposed. In the second (section 2.2), the current knowledge about the nature of muons as elementary particles is described, in addition to the type of interactions they experience when traversing matter. In the third (section 2.3), the technique that uses muon measurements to obtain density maps or extract information about a target is discussed. This technique, as previously mentioned in this document, is usually named *Muon Tomography*, *Muon Radiography* or symply *Muography*. Regarding the technology necessary for its application, the existing types of detection systems are enumerated in this third section, with particular emphasis on the type of detectors used in the studies contained in this thesis, the ones formed of Multi-Wire Proportional Chambers (MWPC). Moreover, the algorithms that interpret the information contained in the muon measurements, and representative application cases conducted with the aim of solving issues in diverse fields, are also presented.

2.1 Discovery of Cosmic Rays and Muons

2.1.1 Measuring the discharge of electroscopes

The first clue of the existence of cosmic radiation was found and reported by Charles-Augustin de Coulomb around 1785, officer of the French army and member of the Académie des sciences, when he realised that his electroscope undergone spontaneous discharges in the air [1]. Later, Michael Faraday addressed the same problem and observed the same effect, even with higher accuracy, therefore reinforcing Coulomb's conclusions [2]. Furthermore, in 1879, Crookes discovered that there was a relation between the velocity of the discharge the electroscopes experimented in the air, and its pressure. He observed lower discharge velocities when the air pressure was smaller [3]. Then, it was understood that the cause of the discharge of the electroscopes should be related with something happening in the air contained within the instrument, something that was causing ionisation inside the electroscopes. However, the origin of this phenomenon was still a mystery.

Some years later, in 1896, Antoine-Henri Becquerel found natural ionising radiation when he was researching about phosphorescence [4]. Marie and Pierre Curie continued the exploration in this emerging field, discovering a generation of natural radiation produced by Polonium and Radium [5]. The electroscopes were discharged when they were located close to this elements, and therefore, it seemed that some elements emitted charged particles discharging them.

Scientists continued researching the peculiar discharge of the electroscopes, and as a consequence, by 1900, Julius Elster and Hans Geitel suggested that the discharges were caused by penetrating and ionising agents [6]. These conclusions were extracted after an experiment in which they performed a measurement of the discharges putting a electroscope inside a thick metal box. Even in that occasion, they measured the same spontaneous discharges in the electroscope. At that time, Elster and Geitel in Germany, as well as Charles Thomson Rees Wilson in England, managed to improve the sensitivity of electroscopes using a insulation system based on a closed vessel. This improvement allowed them to make measurements that quantified the rates of discharge undergone by the electroscopes.

At this point, the main question that had no answer was whether the radiation was coming from the already found radioactive elements or it was generated in the atmosphere or in further origins in the outer space. In 1901, the previously mentioned Scottish physicist Charles Thomson Rees Wilson, observed the same behaviour in the discharges as Elster and Geitel, and suggested that the origin of the radiation producing them was possibly extraterrestrial [7]. He measured with his electroscope inside a tunnel in Scotland, looking for a drop in the radioactivity presumably produced by the rock over the location of the electroscope. Unfortunately, he could not observe it due to experimental uncertainties. Thus, he could not prove his extraterrestrial hypothesis.

2.1.2 Balloon flights and other experiments

Between 1900 and 1903, Franz Linke, as a PhD student, performed 12 balloon flights and measured radioactivity with an electroscope built by Elster and Geitel [8]. He flew up to 5500 metres gathering ionisation measurements. Although the purpose of his thesis was other, he did an exceptional work which could have solved the doubts about the cause of the spontaneous discharges of the electroscopes, but his conclusions were wrong. Indeed, he concluded that the source of radioactivity was terrestrial, confused by the low ionisation rates he observed at heights between 1000 and 3000 metres comparing to the ones at the Earth surface, and not interpreting correctly the intense ionisation he measured at altitudes around 5500m.

The question was still without answer, and the research continued. In 1909, Theodor Wulf, a scientist and jesuit priest, designed a more robust electrometer, which could be also more easily transported. He replaced the gold leaves of the normal electroscopes by two metalised glass strips in tension. Wulf tested and validated his instrument performing several measurements in different places of Germany, Holland and Belgium. In his opinion, all the results and validations were consistent with the hypothesis that the ionisation measured by the electroscopes was mainly due to a generation of radiation in the upper layers of the Earth's crust. That year and the next one, he travelled to Paris with the aim of performing measurements in the top of the Eiffel Tower with his electroscope [9] [10]. He wanted to prove his hypothesis, but the results of the experiments showed that the decrease of the radiation in the top of the Eiffel tower, at around 300 metres above the ground level, was smaller than the one predicted by the terrestrial hypothesis. If the radiation generated in the Earth's surface was dominant, it should be a significant drop of ionisation at that height.

During that years, other kind of measurements were made in order to explore the relation between

Figure 2.1: Original Wulf electroscope used by himself around 1912. [1]

that mysterious radiation and the altitude at which it was observed: balloon flights. The first explorer who had this purpose in mind and flew with a balloon to research it, was Karl Bergwitz, supported by Elster and Geitel, who were his teachers. He gathered dubious and scarce results due to a damage suffered by the electrometer during his flight in Braunschweig area (Germany), and he finally concluded that the measurements showed a decrease in the ionisation rate at 1300 metres of altitude, and although it was not as pronounced as the predictions of the terrestrial hypothesis, he thought that it was a sufficient evidence to validate the terrestrial origin of the radiation [11]. The professor Albert Gockel, who worked in the University of Fribourg, also performed several balloon flights during the same years. He measured the ionisation decreasing up to 2500 metres, but to a lesser extent than Bergwitz. At higher altitudes he got strange measurements that he related to a malfunctioning of the electrometer. In any case, he already suspected that there had to be another source of radiation in addition to that of the earth [12] [13].

Gockel's thoughts were in agreement with the research made also around 1910 by Domenico Pacini, an Italian physicist who questioned the terrestrial hypothesis with his experiments. Pacini measured the radiation in a ship of the Italian Navy, in a location close to the Naval Academy of Livorno at a distance of 300 metres from the coast, with the intention of moving away from the radiation emitted by the elements of the Earth's crust. In that situation, he observed a non-negligible 70% of the radiation measured on dry land, a result which supported the idea of the existence of an additional radiation source [14]. He continued exploring the behaviour of this radiation measuring it underwater. For that purpose, he used a pioneer technique, enclosing the electroscope in a copper box. The application of this method represented a remarkable milestone in the history of physics. Using the mentioned technique, he discovered that when the electroscope was submerged a few metres in the water, the amount of measured radiation was significantly reduced. He observed that effect both in the Gulf of Genoa, close to Livorno, and in the Lake of Bracciano. His conclusions were clear, an important proportion of the mysterious radiation was not originated by the radioactive substances in the upper layers of the Earth's crust. He rightly thought that the measured reduction was a proof of the existence of a penetrating radiation coming from the atmosphere.

2.1.3 Discovery of comic Rays, reactions and further research

Despite the evidences that Wulf, Bergwitz, Goeckel and Pacini gathered, the origin of that penetrating radiation was still not clear for the scientific community. In 1911, the Austrian physicist Victor Franz Hess reviewed the work done by some of the aforementioned researchers and he decided to improve the sealed electrometers they were using to get more precise measurements. In his first balloon flight, he observed radiation rates not matching the terrestrial hypothesis calculations and he planned a series of balloon flights to search the physical phenomenon behind the radiation they were measuring. During 1911 and 1912, he flew up to 9 times, in order to collect enough data which could explain the mystery. He reached a height of more than 5000 metres in one of his flights, registering a radiation six times more intense that the one measured at the Earth's surface. In 1913, Victor Hess completed the analysis and interpretation of these balloon flight measurements, and published his work, in which he stated, as the main conclusion, that an extremely penetrating radiation coming from outer space existed [15]. The previous studies of pioneering researchers should be kept in mind, but Victor Hess is considered the main discoverer of Cosmic Rays. It also must be mentioned that the term Cosmic Rays was introduced with posterity by the American physicist Robert Millikan.

From the moment of Hess' discovery and until the year of his Nobel prize, the data and conclusions of his research were questioned, although there were also scientists who believed in their truthfulness. Bergwitz, Milikan, and two German and one Swiss physicists, Werner Heinrich Gustav Kolhörster, Erich Rudolf Alexander Regener and Auguste Antoine Piccard had an important role in that process. Bergwitz stated that temperature fluctuations could cause spurious measurements of the electrometers [16], while Kolhörster tried to demonstrate that this fact was not decisive in the research of Victor Hess, performed additional balloon experiments. He even reached an altitude of 9300 metres, confirming Hess' results [17] [18]. Millikan also proved that the radiation detected by Hess was of extraterrestrial origin [19]. However, he was wrong about their composition. Conditioned by religious beliefs, he thought that they were "birth cries of atoms" related to ongoing creation in the universe, and that they were formed by high-energy photons. In 1932, Arthur Holly Compton shed light on this issue, leading a cooperative worldwide research which showed that the intensity of Cosmic Rays was correlated with geomagnetic latitude (latitude effect) [20]. Then, Compton correctly interpreted that Cosmic Rays were made up of charged particles, instead of photons, as Millikan stated.

During the same year, Regener, Millikan and Piccard also made great contributions to the atmospheric measurements of the radiation. Erich Regener, a German physicist, used a self-recording electroscope carried by a balloon to reach the altitude of 26000 metres, and get excellent and accurate measurements of cosmic-ray ionisation as a function of altitude [21] [22]. He avoided the temperature effects that significantly affected previous experiments of Millikan enclosing the electroscope in a plastic container which retained the heat produced by the sun rays and kept the temperature between +15C°and +37C°. Regener is also known due to its deep underwater radiation measurements and the discovery of the height of maximum ionisation production in the atmosphere [23] [24]. During the latter research he collaborated with the scientist Bernhard Gross [25], and with his student Georg Pfotzer [26]. The altitude where ionisation reaches the maximum in the atmosphere was named as Pfotzer maximum. Regener was not even mentioned, although he had been the researcher who led the discovery. The cause probably was the Jewish ancestry of his wife, that caused them severe problems with the nazi regime.

In 1932, Millikan also flew a unmanned balloon with an automatic electroscope. He tried to remove the temperature effects, like Regener, and improved the design of his electroscope to avoid them [27]. Auguste Piccard, a physics professor in the Université libre de Bruxelles, made an additional balloon flight, his second, flying with the Belgian physicist Max Cosyns up to 16000 metres. The data Piccard obtained was in accordance with Reneger's measurements, and both overlapped the Hess-Kolhörster curve validating their results. Then it became clear that Hess was right, his findings were already proven by several scientists using varied, and more developed and precise technologies.

Finally, in 1936, Victor Franz Hess received the Nobel prize in physics as the discoverer of cosmic rays. He shared it with the American physicist Carl David Anderson, who under the supervision of Robert Millikan himself, began to investigate cosmic rays and ended up proving the existence of the positron, fact that led him to share that prize. Compton nominated Hess, but he could not have nominated Pacini, since he had died two years before. Compton highlighted the importance of the discovery and the pioneering measurements and clear conclusions of Hess, who proved and stated that actually existed an increase of the ionisation related to the atmospheric height and that its cause was radiation originated out of the Earth. In any case, it should be also noted that his research was based on work of many other scientists. Some of them have been already mentioned in this document, together with their remarkable contributions. Elster and Geitel, and Wulf, developed the electroscopes, Wilson was the first one formulating the hypothesis of cosmic radiation, Linke, Bergwitz and Gockel contributed with several balloon flight measurements, and Pacini extracted the same conclusion as Hess, although his proofs were not so evident. On the other hand, the first world war, and the turbulent political situation of those times made it more difficult the research, communication, and information exchange between scientists from different countries.

2.1.4 Discovery of muons

Carl David Anderson, who shared the Nobel prize of 1936 with Victor Hess, was also, together with Seth Neddermeyer, one of the researchers who collaborated in the discovery of the muon, first elementary particle discovered that did not belong to conventional atoms. They measured "particles less massive than the protons, but more penetrating than electrons" [28, 29]. J. C. Street and E. C. Stevenson later confirmed their existence, by means of an experiment in which they proved that these particles deflected if a magnetic field is applied to them, forming an intermediate curvature between the electron and the proton [30]. Anderson and Neddermeyer assumed that those "singly occurring particles" were not protons, as the ionisation they produced was of different magnitude and they were more penetrating than what was due to them with their magnetic deflection. They predicted the existence of a charged particle with an intermediate mass, in between of the masses of the proton and the electron. What Street and Stevenson did was to measure and photograph the magnetic deflection of those particles using an apparatus which included a cloud chamber. In [30] they published photographs of two different tracks measured in that outstanding experiment. They concluded that one of them corresponded to a proton, and the other one to the new type of particle. In the detection event corresponding to the new particle, they observed such a high ionisation density that they could not determine it precisely. Nevertheless, they tried to estimate its mass, obtaining a value 130 times bigger than the rest mass of the electron, with an error of roughly the 25%.

Those experiments would not have been possible without Charles Wilson's invention, the cloud chamber, also called Wilson chamber. Wilson has been already mentioned in section 2.1.1 because of its work with the electroscopes and as the pioneer who first formulated the hypothesis of the extraterrestrial radiation. In 1927, he received the Nobel prize in physics. He shared it with Arthur Holly Compton, who received the prize as a result of the Compton effect discovery, and his research about cosmic and X rays.

At the time of their discovery, the muons were named mesotrons [31]. Beforehand, in 1935, Hideki Yukawa predicted the existence of mesons (originally called mesotrons), particles which would have an intermediate mass between of those of the electrons and the protons, and would be responsible for the strong nuclear force. Since the muons seemed to agree with that prediction, they were considered mesons. Later, more particles were discovered with similar characteristics and they were called mesons too. Then, in order to differentiate the muon, it was renamed as µ-meson. Finally, it would be discovered that the muons do not participate in the strong interaction. Therefore, such nomenclature was abandoned and they were started to be called as nowadays, muons.

2.1.5 East-West effect and absorption anomaly

Bruno Benedetto Rossi, an Italian experimental physicist graduated in the University of Bologna, was the scientist who, in 1930, made the first prediction of the"East-West effect" [32], that is to say, the different intensity that should be when comparing the cosmic rays arriving from the east, and those arriving from the west, due to the magnetic field of the Earth. He also tried to verify it experimentally, but his attempt was not satisfactory. The next years, other physicist such as Thomas Johnson [33], Luis Alvarez and Arthur Compton [34], and Rossi himself [35], proved with experimental data the existence of the effect and observed that the intensity was greater from the west. This azimuthal asymmetry, indicated that most primaries were positive. After those initial experimental proofs, over the next decade, the composition of cosmic rays was studied and it was widely confirmed that the majority of the primary cosmic rays were protons, and that secondaries which are produced in the atmosphere were mainly electrons, photons and muons.

In 1938, Rossi lost his professorship for political reasons and left Italy, but he did not stop working in cosmic ray research. Around 1940, physicists and researchers were already exploring the dependence of cosmic radiation intensity on the atmospheric depth, and a decrease in mesotron (term used to refer to muons at that time, see explanation in section 2.1.4) component when measuring at smaller heights above sea level was found. Furthermore, this absorption could not be explained by the energy loss produced in the ionisation of such particles. Scientists found that a layer of air produces a higher absorption comparing to a shallower layer equivalent in terms of ionisation losses, composed of denser material. Bruno Rossi interpreted this discovery and hypothesised that mesotrons may disintegrate in few microseconds. Their short lifetime could explain this absorption anomaly, introducing a factor which would not be connected to the ionisation losses caused by the medium traversed by the particles. Therefore, if particles with similar speed propagate through larger distances, it would be logical to expect a higher absorption due to the propagation time. On the other hand, when particles propagate short distances in dense medium, it would not be expected a significant absorption because of lifetime. The time needed to go through these short distances by particles is negligible compared to their lifespan. In [36], Rossi theorised about the dependence of the probability of muon decay on momentum, and experimentally demonstrated it. He analysed separately two groups of muons, a energetic group (range larger than 311 g/cm^2), and another group of softer muons (range between 196 g/cm^2 and 311 g/cm^2). He found that the disintegration of the less energetic muons occurred roughly three times faster, agreeing with the theoretical calculations considering theory of relativity. His experimental estimation for the lifetime of muons was of 2.4 microseconds.

Later, in the 1960s, Frisch and Smith measured μ-mesons (term used to refer to muons at that time, see explanation in section 2.1.4) on the top of Mt. Washington (New Hampshire) with the aim of demonstrating relativistic time dilation. They selected muons with velocities in between $0.9950c$ and 0.9954, and with the same requirements they measured also muons reaching the sea level, in Cambridge (Massachusetts). They observed a time dilation factor of 8.8, which was within the relativistic predictions [37]. In 1977, measurements of time dilation were also performed in the CERN (Conseil Européen pour la Recherche Nucléaire). Bailey and his team measured high energy muons ($\lambda = 29.33$) and obtained estimations for the lifetime of both positive and negative muons that agreed with special relativity. The estimated lifetime for negative muons was of 2.1948 microseconds [38].

2.2 Nature of cosmic muons and their interaction with matter

Cosmic muons are created in the interactions between cosmic radiation and the atmosphere. Cosmic rays are particles of high energy whose origin is outside the solar system. They are conformed mostly by protons and helium nuclei, but there are also electrons, carbon, oxygen and iron in very small proportions. Secondary cosmic rays, on the other hand, are the result of the interaction of the primary cosmic rays with interstellar gas, and are formed by lithium, beryllium and boron nuclei. Antiprotons and positrons are also part of secondary cosmic rays, although it is currently under study whether a small part of them could derive from the primary cosmic rays. This cosmic radiation reacts with the atoms present in the earth's atmosphere creating particle cascades, and muons are one of the types of particles which are present in the cascades. Muons are able to reach the earth despite its short lifetime. This is due to their propagation speed, close to the speed of light, which produces relativistic effects, allowing the muons to travel long distances. In fact, analysing the intensity of the cosmic cascades at the sea level, muons turn out to be the type of charged particle with the largest presence, although they are typically created at 15 km altitude and lose about 2 GeV as they pass through the atmosphere towards the Earth's crust [39].

Regarding the interaction with matter, the reaction of muons is described by two effects: the loss of energy they undergo when ionising the medium they cross, and the multiple coulomb scattering they suffer due to collisions with nuclei of matter [40]. Muons are charged fundamental particles similar to electrons, although they have a mass 200 times greater. This implies that they are unstable and have a life cycle τ_0 of approximately 2.2 μs [41]. However, due to the effects of relativity, this time is considerably dilated in the Earth's reference system and in their short lifetime muons are able to pass through the atmosphere and even penetrate the Earth's crust.

2.2.1 Particle showers in the atmosphere

The radiation which penetrates through the upper atmosphere consists of stable charged particles and nuclei with long lifetimes, roughly of 10^6 years. These rays have a nearly isotropic incidence in the atmosphere for most of the energy spectrum [39]. When the original particles arriving to the top of the atmosphere, the primary and secondary cosmic radiation, enters into the atmosphere, it starts to undergone interactions with electrons and nuclei of atoms and molecules which are present in the air. This is the reason why the nature of cosmic radiation is transformed while it is propagated through the atmosphere. The particles composing such radiation loss energy through hadronic and electromagnetic processes [42]. Note that within the framework of the atmosphere, both primary and secondary cosmic rays are named as primary. Atmospheric secondary radiation is composed of the new particles created when these radiations of cosmic origin penetrate the atmosphere and react with it.

In collisions of atmospheric nuclei (O, N) with cosmic hadrons, where the strong force is present, additional particle showers are produced, leading to the creation of secondary particles, such as mesons. Both, the rest of the primaries and the young secondaries, continue to propagate and interact downwards in the atmosphere. In hadronic collisions, pions (the most numerous) and kaons are produced, among other particles. This sort of particles can continue interacting or can decay, depending on their energy and average lifetime. For example, charged pions can decay into muons and neutrinos:

$$\pi^+ \rightarrow \mu^+ + \nu_\mu \tag{2.1}$$

$$\pi^- \rightarrow \mu^- + \overline{\nu}_\mu \tag{2.2}$$

Muons and neutrinos easily penetrate through the atmosphere, and as already pointed out, although their short life time, muons are able to reach the sea level thanks to the relativistic time dilation. However, some of them also decay, producing as a result electrons and more neutrinos:

$$\mu^+ \rightarrow e^+ + \nu_e + \overline{\nu}_\mu \tag{2.3}$$

$$\mu^- \rightarrow e^- + \overline{\nu}_e + \nu_\mu \tag{2.4}$$

The interaction and decay processes described above (consult [42] for more detailed information), as well as other main phenomena happening in atmospheric cosmic showers are shown in fig. 2.2. A primary collides with atmospheric nucleus, creating new particles, mainly pions, and kaons. These, in turn, decay into photons, which generate electron-positron pair production, and also into muon and neutrinos. Therefore, three different components are present in the atmospheric particle showers: the *hadron component*, basically consisting of nucleons, pions, and kaons, the *electromagnetic component*, showers composed of gamma rays and electron-positron pairs, and *muon component*, which includes neutrino generation and also contributes to electron-positron generation.

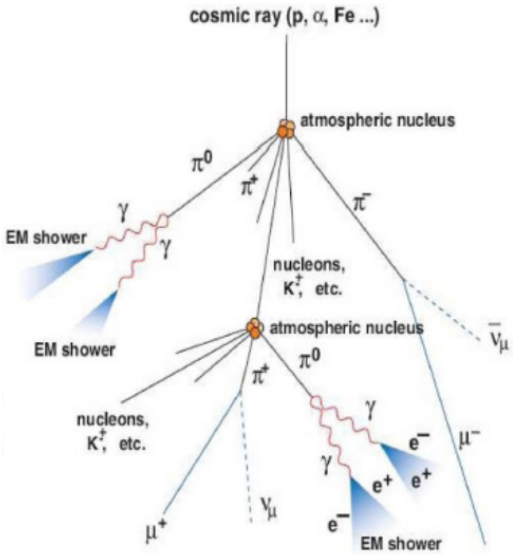

Figure 2.2: Atmospheric particle showers generated by a cosmic ray. The primary collides with atmospheric nucleous generating hadron, electromagnetic, and muonic components. [2]

2.2.2 Cosmic muon flux

It is essential to consider and exploit the knowledge about cosmic muon flux on the earth surface when testing the operation of detectors, or when using them to perform muography measurements. The expected intensity of muon flux is a useful reference to estimate detector efficiency and detect the presence of background noise. Other parameters describing the muon and background flux, such as the momentum, help also to manage the presence of noise and to filter it. A good understanding of cosmic muon flux properties helps designing optimal detector configurations and algorithms for the different applications of muography, as nowadays it is the only source of all the muography experiments and applications.

Intensity (I)

For muography experiments using horizontal detectors, the following quantitative approximation for the muon intensity (I) is widely used [43]:

$$I = 10000 \; [\frac{\mu}{m^2 \; min}] \tag{2.5}$$

Where μ represents the number of muons. Some research work results [44] [42] specify that at sea level, the integral intensity of vertical muons above $1 GeV/c$ is of about:

$$I_{0\ ma.s.l,\ p>1Gev/c} = 70\ [\frac{\mu}{m^2\ s\ sr}] \tag{2.6}$$

Although more recent measurements [45] [46] [47] suggest that muon flux is less intense, and that the integral intensity of vertical muons above $1GeV/c$ is within the range specified below:

$$I_{0\ ma.s.l,\ p>1Gev/c} = (59.5,\ 63)\ [\frac{\mu}{m^2\ s\ sr}] \tag{2.7}$$

Incidence angles (θ, ϕ) and momentum spectrum

The integral intensity of muons has negligible dependence on azimuth angle ϕ, while the zenith angle θ influence is strong, since the thickness of the atmosphere that the particles have to pass through depends on it [42]. Assuming a flat Earth, the dependence of the muon flux I on zenith angle θ can be represented by the following equation:

$$I(\theta) = I_0\ cos^{n-1}(\theta) \tag{2.8}$$

where n is a function of muon momenta, and I_0 the vertical muon intensity. Generalising the expression for a characteristic muon energy of $3\tilde{\mathrm{G}}\mathrm{eV}$, a relation of $cos^2(\theta)$ between $I(\theta)$ and I_0 is obtained [43]. Since the assumption of a flat Earth is taken to develop the eq. (2.8) it works well for small zenith angles, but is not accurate for large angles. In those cases, mathematical models considering curved Earth surface should be applied to calculate the muon flux as a function of zenith angle [48].

The angular and energy distribution of cosmic muons are a convolution of their production spectrum, propagation and energy loss trough the atmosphere, and decay probability. 4 GeV is approximately the mean energy of muons at the Earth surface, although the median and the peak of energy distribution are in lower values. In the fig. 2.3, measurements of cosmic muon momentum spectrum at sea level for two different zenith angles ($\theta = 0°$, and $\theta = 75°$) are shown, together with an extrapolation formula (valid for high energies and zenith angles smaller than 70°), which is applied for the case of $\theta = 0°$ [43].

In figure fig. 2.3, the muon momentum spectrum for $\theta = 0°$ and $\theta = 75°$ are clearly distinguished. At large zenith angles, muons have to travel longer distances through the atmosphere, undergoing larger energy losses, a fact which results in smaller muon differential intensities in low ranges of momentum spectrum. In figure fig. 2.4, measurements of muon intensity spectrum at other zenith angles ($\theta = 0°$, $\theta = 30°$, $\theta = 60°$, $\theta = 75°$) and in a momentum range that goes from 1.75 GeV to 22.5 GeV have been added, as an example of the mentioned atmospheric propagation effect.

Velocity

Knowing the muon momentum (p), the velocity (v) can be calculated applying momentum-velocity relation of relativistic mechanics eq. (2.9):

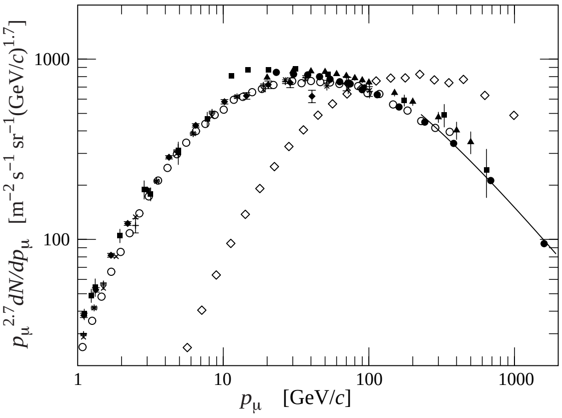

Figure 2.3: Measurements of muon momentum spectrum at $\theta = 75°$ ($\diamond$), and $\theta = 0°$ (rest of the markers). The line represents the result of an extrapolation formula valid for high energies and $\theta < 70°$, applied in this case for $\theta = 0°$. Additional information about measurements and the mentioned formula can be found in [43]. [3]

$$p = m\gamma\beta \tag{2.9}$$

Where γ is the Lorentz factor, and β the ratio between muon velocity and the speed of light:

$$\gamma = \frac{1}{\sqrt{1-\frac{v^2}{c^2}}} \tag{2.10}$$

$$\beta = \frac{v}{c} \tag{2.11}$$

Specifying the Lorentz factor, momentum-velocity relation becomes:

$$p = m\frac{1}{\sqrt{1-\beta^2}}\beta \tag{2.12}$$

Developing the equation:

$$\beta = \frac{p}{\sqrt{p^2+m^2}} \tag{2.13}$$

Which considering energy–momentum relation, or relativistic dispersion relation,

$$E^2 = p^2 + m^2 \tag{2.14}$$

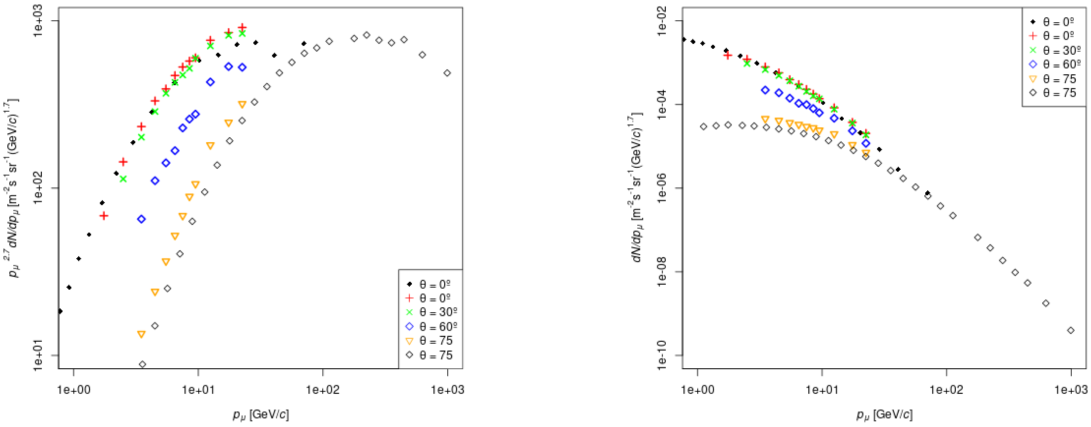

Figure 2.4: Measurements of muon momentum spectrum at different θ. The measurements of $\theta = 0°$ (♦) [44] and $\theta = 75°$ (⬨) [49] correspond with the data in the fig. 2.3. Additional measurements at other zenith angles ($\theta = 0°$, $\theta = 30°$, $\theta = 60°$, $\theta = 75°$) [50] have been added to this figure. On the graph of the right muon momentum spectrum is plotted, without multiplying it by $p^{2.7}$.

can be also written as:

$$\beta = \frac{p}{E} \tag{2.15}$$

Therefore, including muon mass μ [41],

$$m = m_\mu = 105.6583755 \pm 0.0000023\ [MeV] \tag{2.16}$$

the muon velocity is given by:

$$v_\mu = \frac{pc}{\sqrt{p^2 + m_\mu^2}} = \frac{pc}{E} \tag{2.17}$$

Muons arriving to the Earth surface with a common momentum p_μ, of for example 1 GeV, travel with a velocity around 0.9999472 c, while soft muons of $p_\mu = 0.1$ GeV travel at roughly 0.9947586 c. The speed of energetic muons of $p_\mu = 10 GeV$, is 0.9999995 c. From the point of view of muography, differences in speed have little influence, since, in general, the velocity of natural cosmic muons is close to the speed of light ($v_\mu > 0.99$).

Life time

As it has been mentioned before, muon life time expectation τ_0, is roughly 2.2 μs, but it is dilated depending on p [42]:

$$\tau_{\mu,dilated} = \tau_\mu \gamma \tag{2.18}$$

Where γ is the Lorentz factor. On the other hand, muon decay probability Pd_{μ}, is approximately directly proportional to its mass m_{μ}, and the material thickness traversed x, but inversely proportional to the density of the medium ρ, τ_0, and momentum p [42]:

$$Pd_{\mu} = 1 - exp\left(-\int \frac{m_{\mu}}{\rho \tau_0 p} dx\right) \simeq \frac{m_{\mu} x}{\rho \tau_0 p} \tag{2.19}$$

Note that this expression does not consider the continuous energy loss that muons undergo when crossing the atmosphere, which is produced by ionisation, nor the heterogeneous density profile of the atmosphere.

Altitude, geomagnetic, atmospheric, and heliospheric dependence

Comparing data of muon measurements at different altitudes above sea level, its influence on muon flux can be observed (see fig. 2.5). In the measurements summarised in the figure, where the altitude above sea level varies from 30 up to 2770 m, the muon flux intensity increases with altitude, especially below 30 GeV.

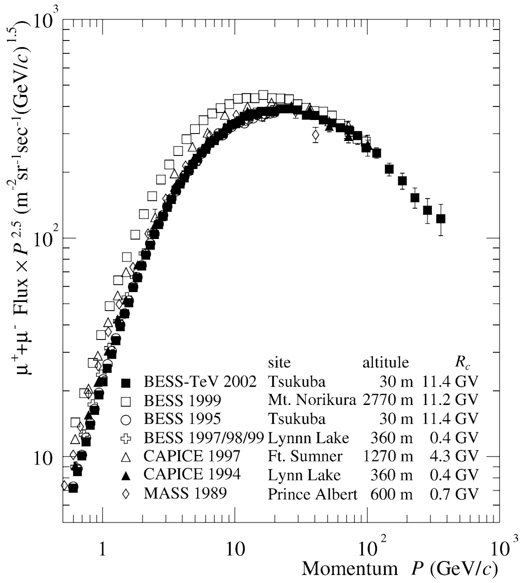

Figure 2.5: Absolute differential momentum spectrum of atmospheric muons. Check [47] for more information about the measurements. [4]

Regarding the geomagnetic dependence, note that the“East-West effect”, that is, the azimuthal asymmetry which exists due to the positive charge of primaries and the Earth’s magnetic field, has been already discussed in this thesis (see section 2.1.5). The cosmic ray incidence intensity is higher from the west.

Theoretical explanations of these, and also other effects that cosmic muon flux undergoes, which are produced by factors such as the latitude, longitude, temperature, pressure, and heliospheric influence can be found in [42].

2.2.3 Background noise

As seen in section 2.2.1, cosmic ray atmospheric showers include other charged particles, such as protons, electrons, and positrons, which in the same way as muons, arrive to the Earth surface, in spite of their stronger interactions with matter. Protons undergone nuclear interactions, unlike muons. The Bremsstrahlung energy loss depends on $1/m$, where m is the mass of the particle. Thus, it is much lower for muons. Furthermore, cosmic shower positrons are likely to disintegrate with electrons from atmospheric atoms. Those factors, at sea level, reduce significantly the background flux comparing it to the muon flux. However, their impact in measurements with no momentum cut is far from being negligible [51]. Above 1 GeV, and at sea level, the cosmic background particles are at least 2 orders of magnitude less numerous than muons (see fig. 2.6). Noise caused by the muons themselves should be also considered. Subsequent muons could arrive to the detection layers with time intervals which are not large enough to be accurately distinguished by the electronic systems.

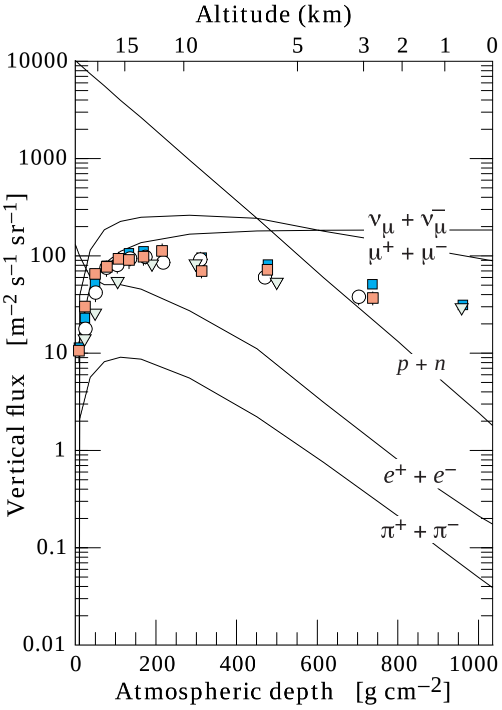

Figure 2.6: Vertical fluxes of cosmic ray particles with $E > 1GeV$ depending on the atmospheric depth, which are inferred from a nucleon flux model. The points correspond to experimental measurements. Check [43] for more information about the model and experiments. [5]

2.2.4 Muons within standard model

The Standard Model of particle physics describes the electromagnetic, weak and strong interactions, excluding gravity. It explains three out of the four fundamental forces that are known, and classifies the discovered elementary particles. Fermions are the type of particles which constitute the matter, and they have a spin of 1/2. There are 12 different fermions, and each of them has its corresponding antiparticle. Fermions are classified depending on their charge, which determines how they interact. The six quarks have charges of 2/3 or -1/3, while the six fermions carry -1, or null charges. Fermions, both leptons and quarks, are subdivided into generations or families. Particles of higher generations are more massive than those of lower generations, although this is not still neither demonstrated nor rejected for neutrinos, which have small non-zero masses that have not been precisely quantified yet.

Quarks are sensitive to the electromagnetic interactions, as well as to the strong, and weak nuclear forces. On the other hand, leptons intervene only in the electroweak interactions, i.e, electromagnetic and weak interactions. Gauge bossons (which are also vector bosons, since their spin equals one) are the force carriers of elemantary fermions, meaning that they are responsible of the interactions between those particles. Gluons conduct the strong force, photons the electromagnetic, and W as well as Z bossons the weak force. The Higgs bosson, whose first observation was announced by the CERN in 2012, constitutes the quantum, or in other words, the smallest possible excitation of the Higgs field. Both Higgs bosson and Higgs field are essential to explain the origin of the mass of elementary particles, which is generated when the Higgs mechanism is triggered.

The standard model has successfully predicted the Higgs boson and its characteristics, as well as top and bottom quarks, and Z, W, and gluon bosons. It also explains most of the physical processes, like decays or scatterings, matching with experimental measurements. However, there are certain phenomena which the model is not able to explain, such as issues about neutrino masses, or gravitation theory, among others. The hierarchy problem, i.e., the great differences between weak force and gravity, like the magnitude of their energy range, are still not understood completely. The weak force, is more than 20 orders of magnitude stronger than gravity.

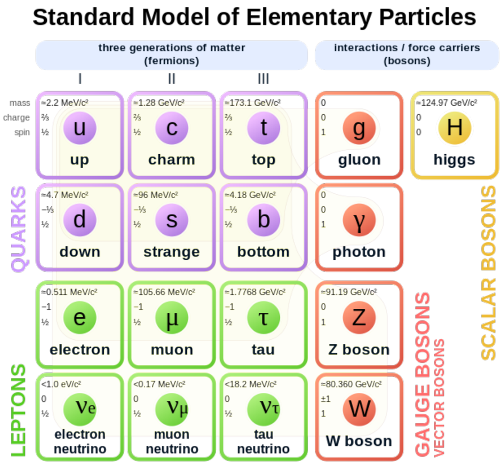

Figure 2.7: Elementary particles of the Standard Model. The muon is a second generation fermion, and a lepton.

The mass hierarchy of the different generation particles of the standard model, which is other point on which a lack of consensus exists about its explanation, is also an indicator of the life time of particles. The muon, is more unstable comparing to the less massive particle of the previous generation of its sub-type (leptons of charge -1), the electron. Having a life time expectation of 2.2

μs, obviously the muons can not be part of the long-lasting“every day terrestrial matter”, i.e. the atoms. The same happens with the other 2$^{\text{nd}}$, and 3$^{\text{rd}}$ generation fermions. Where these relatively massive and unstable particles can be observed, is in physical processes like the cosmic ray particle showers produced in the atmosphere (see section 2.2.1) or in particle accelerators. Pions and kaons, subatomic particles that are part of the atmospheric showers, are composed of a quark and an antiquark, elementary particles of the standard model. They are hadrons, as they consist of two quarks, and within hadrons they belong to the group of the mesons, since they have an equal number of quarks and antiquarks.

2.2.5 Interaction with matter

It is precisely the effects that occur when muons reach terrestrial matter that are of greatest importance for muon tomography and specifically for this project. These particles react when they encounter matter in their path by means of two main processes: ionisation and multiple scattering.

Stopping power **or mean rate of energy loss**

Ionisation and atomic excitation are the main physical processes producing energy loss in muons, up to momenta around 500 GeV [51]. The effect of these phenomena on the energy loss is accurately quantified by the well-known Bethe-Bloch formula, which determines the energy loss per length of material traversed, depending on the incident particle and the properties of the material. In practice, muons have an average momentum of a few GeV, coinciding with the momentum at which ionisation is minimal (see fig. 2.8), i.e. muons typically lose little energy through the aforementioned processes. Here is rewritten the Bethe-Bloch formula for the specific case of muons:

$$\langle \frac{dE}{dx} \rangle = K \frac{Z}{A} \frac{1}{\beta^2} \left[\frac{1}{2} ln \left(\frac{2 m_e \beta^2 \gamma^2 W_{max}}{I^2} - \beta^2 - \frac{\delta(\beta\gamma)}{2} \right) \right] \tag{2.20}$$

Where Z and A are the atomic and mass number of the medium, respectively. This dependence is the most important and influential aspect in relation to current muography techniques. β represents the ratio between the particle velocity and the speed of light. m_e is the electron mass, λ the Lorentz factor, W_{max} the maximum possible energy transfer, I the mean excitation energy, and $\delta(\beta\gamma)$ the density effect correction.

Multiple scattering

Muons, being charged particles, scatter at many angles when they pass through matter. Much of this blurring is due to Coulomb scattering by the nucleus of matter, as explained in Rutherford's cross section. The phenomenon of multiple scattering is explained by Molière's theory. Although large scattering produces a non-Gaussian tail in the deviation distribution of all muons passing through a given material, it can be approximated by a Gaussian distribution with root-mean-square (RMS) width θ_0 [43] (see equation 2.21). Detailed information about multiple scattering studies and models developed can be found in [52] [53] [54].

$$\theta_0 = \frac{13.6 MeV}{\beta c p} \sqrt{\frac{x}{X_0}} \left[1 + 0.038 \ln \left(\frac{x}{X_0 \beta^2} \right) \right] \tag{2.21}$$

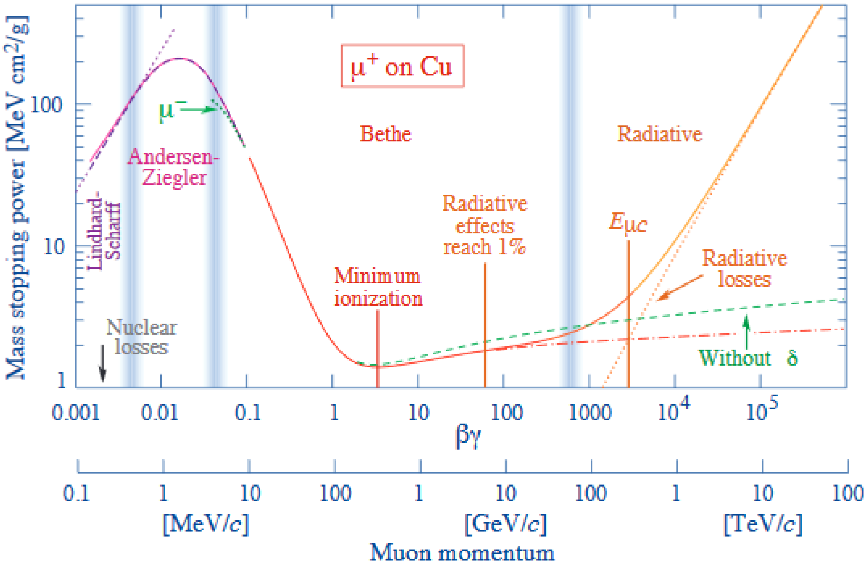

Figure 2.8: *Mass stopping power* or mean rate of energy loss (dE/dx) for positive muons in copper. [6]

Where βc and p are the speed and the momentum of the incident particle, x is the distance that the particle travels within the material in the incident direction (see Figure 2.9) and X_0 represents the radiation length of the material (description in the following section section 2.2.5). β is the ratio between the speed of the particle and the speed of light. The constant 13.6 is measured in million electron volts (MeV) and the aforementioned θ_0 corresponds to the RMS value of muon deviations projected in a plane.

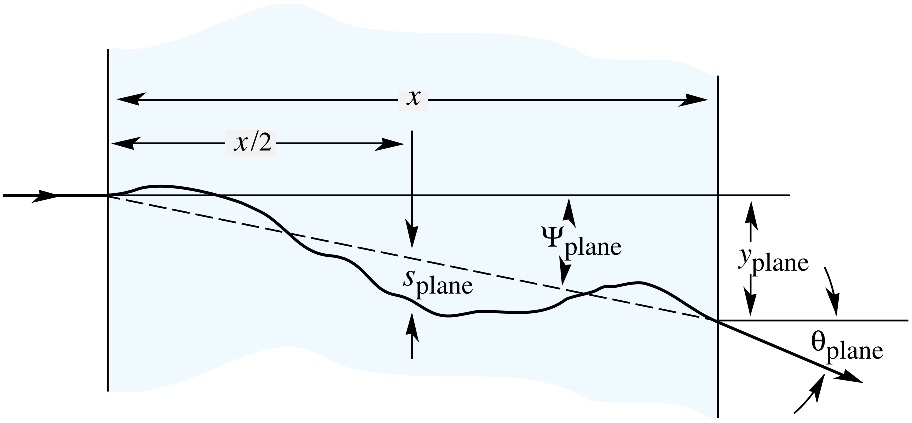

Figure 2.9: Illustration of multiple Coulomb scattering, and the parameters usually utilised to characterise it. In the sketch, the particle is transported horizontally from the left side. [7]

An example of the multiple scattering process and the parameters used to describe it are represented in fig. 2.9. Those parameters are: the already mentioned traversed material thickness x, the distance from the actual position of the particle and its straight line path (SLP) at a depth of $x/2$, represented as s_{plane}, the angle between particle incidence direction and the SLP, Ψ_{plane}, the scattering displacement y_{plane}, and the scattering angle θ_{plane}. The SLP is the straight path joining the particle incidence point on the material to the exit point. Scattering displacement and angle, y_{plane} and θ_{plane}, are correlated, with a coefficient $\rho_{y\theta} = \sqrt{3}/2 \simeq 0.87$. All of them are parameters referring to the scattering projected in a plane.

It should be mentioned that the estimations specified in the current section about multiple scattering are only valid for small θ_0, and they do not consider large-angle scatters.

Radiation length

The radiation length X_0, is a characteristic of materials, which is related to the amount of energy that high energy particles lose when they electromagnetically interact with them. It is defined as the average distance throughout which an energetic electron has its energy reduced by a factor $1/e$ due to bremsstrahlung. It is measured in cm, or in g/cm^2, depending on whether it is expressed as a distance, i.e., a thickness of material traversed by the particle (named in this thesis *thickness radiation length*), or as the amount of mass contained in the material column corresponding to that distance (named in this thesis *mass radiation length*). The *thickness radiation length* of materials is given in cm, while in g/cm^2 it is given the *mass radiation length*.

This property of materials, it is used to describe the multiple scattering, as already noted above (see section 2.2.5). Calculations of radiation length using analytical equations can be found in [55], as well as comparisons with methods applied by other scientists for the same purpose. PDG (Particle Data Group) has collected data about atomic and nuclear properties of materials, including X_0, which can be consulted in in pdf format [56], and in an interactive website [57].

In fig. 2.10, data from the mentioned sources has been plotted. Several elements are characterised by the relation of their atomic number Z, with other properties, namely, their mass and linear radiation length, their density, and their thickness expressed in number of radiation lengths and considering 1 cm. The latter property, is precisely the one that determines the magnitude of the multiple scattering undergone by muons, as specified in eq. (2.21). It could be defined too as the number of radiation lengths contained in a single unit of thickness.

The radiation length of a composite material, given those of the materials which are part of it, can be obtained trough the following formula:

$$1/X_0 = \sum w_j/X_j \tag{2.22}$$

where j refers to the different materials composing the mixture, in such a way that w_j and X_j are the weight fraction, and the radiation length of the material j.

2.3 Muography

2.3.1 Main idea and measured phenomena

From the beginnings of Muon Radiography (MR) in the early 1950s, both absorption and scattering of muons has been used to inspect structures and get a density map of their interior. MR is a technique which exploits the presence of cosmic muon showers, created in the atmosphere, to

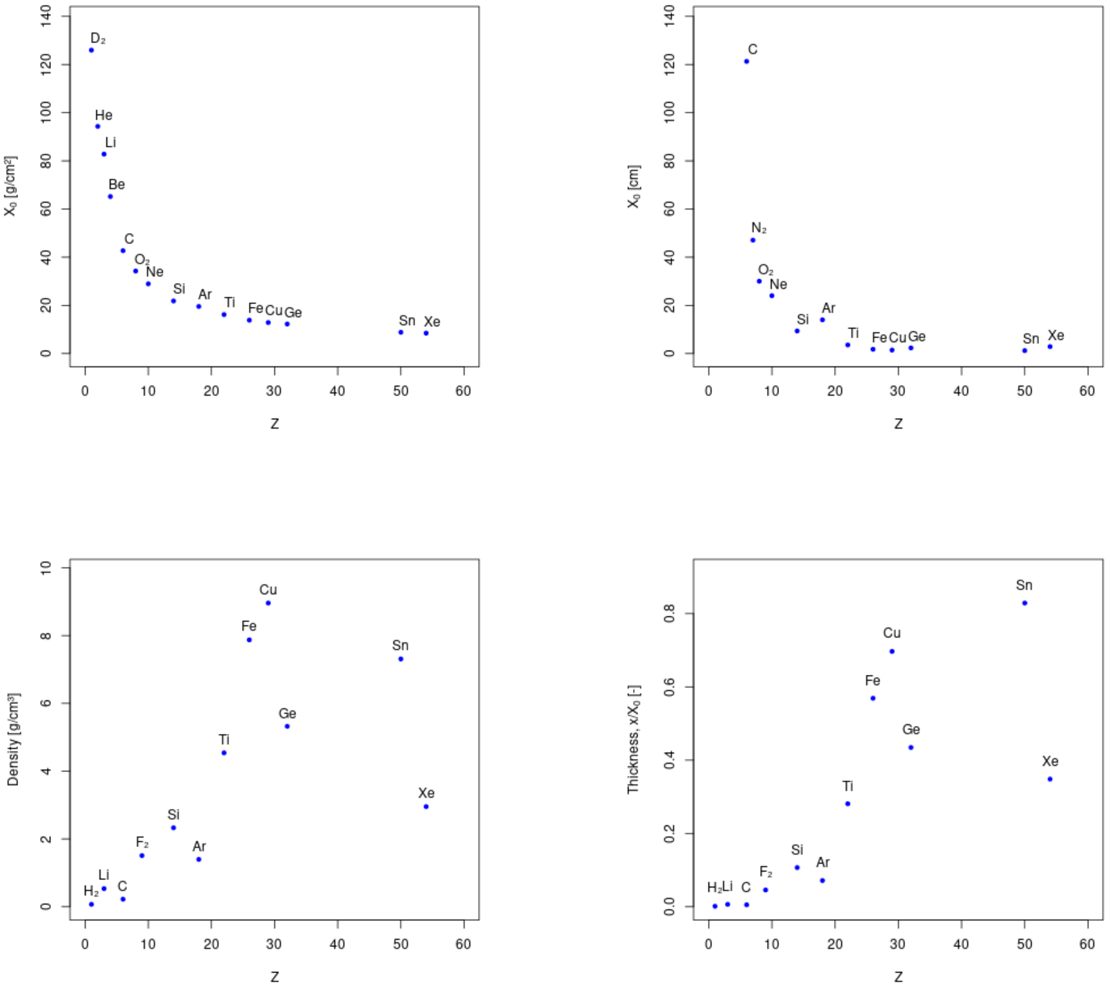

Figure 2.10: Characterisation of some elements by the relations of their atomic number Z, with radiation length and other properties such as density, and thickness. The latter is expressed in number of radiation lengths and considering 1 cm. Data from [56] [57].

measure them and extract a natural radiography, and it can be applied in the aforementioned two modalities: absorption and scattering.

Muon Absorption Radiography (MAR)

The Muon Absorption Radiography (MAR) is adequate for problems involving big targets due to its capability of scanning big areas in relation to the detector dimensions. This method only needs one detector to measure the incoming muons that have crossed the target. The density map of the scanned area is created counting the number of muons, knowing that they are absorbed when crossing big amounts of dense material due to the energy loss they undergo (see section 2.2.5).

In the example of fig. 2.11, a volume containing dense material (a volcano) is represented, and within it, a cavity is present, marked with light blue color. The muon detector located close to the object collects the muons arriving with different incidence angles. The number of counts abnormally increases for muon directions crossing the cavity.

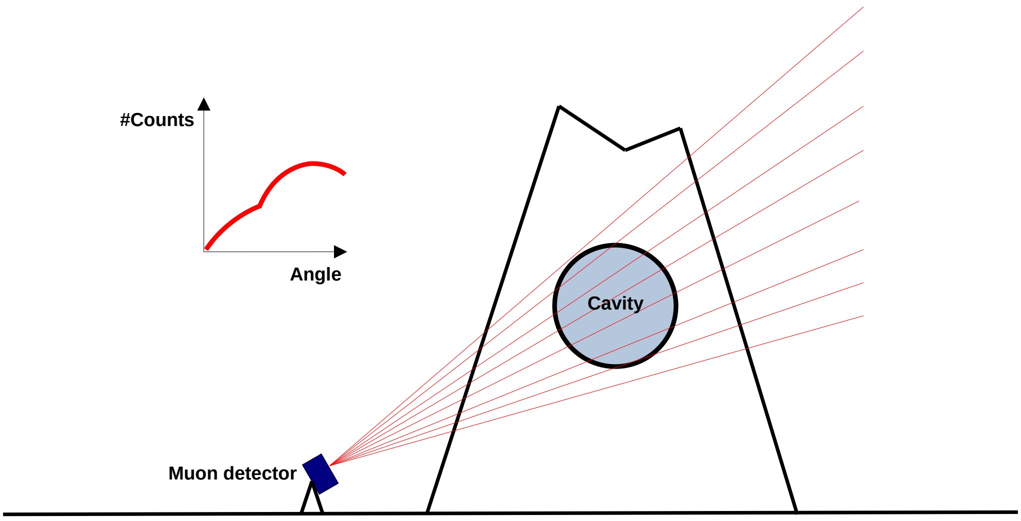

Figure 2.11: Muon Absorption Radiography (MAR) scenario example. One muon detector and a large structure (volcano) with a cavity (light blue) are represented. The distribution of muon counts is abnormally increased depending on the incidence angle.

Muon Scattering Radiography (MSR)

Muon Scattering Radiography (MSR) is appropriate to detect medium and small size targets. In this case, two detectors are needed to measure muon trajectories before and after the target, scanning smaller areas but obtaining the deviation of muons, information which allows to perform more precise reconstructions. These deviations are produced by the Multiple Scattering which suffer charged particles when traversing matter (section 2.2.5). The larger the muon trajectory deviation is, the denser the measured object.

In the example of fig. 2.12, a target, specifically an industrial pipe, is measured. The muon detector located above collects the incidence angles of muons before arriving to the target θ_{in}, and the detector below measures the muon trajectories after crossing the scenario θ_{out}. The change undergone by the muon trajectory, i.e. the existing difference when comparing the angle of output trajectory with the one recorded by the detector above, is the scattering angle:

$$\Delta\theta = \theta_{out} - \theta_{in} \tag{2.23}$$

On the right of fig. 2.12 an histogram with two scattering angle probability distributions is represented. The blue curve shows a distribution of scattering angles produced by a lighter scenario comparing to the distribution of the red curve, where muon scatters are harder due to the presence of a larger amount of matter.

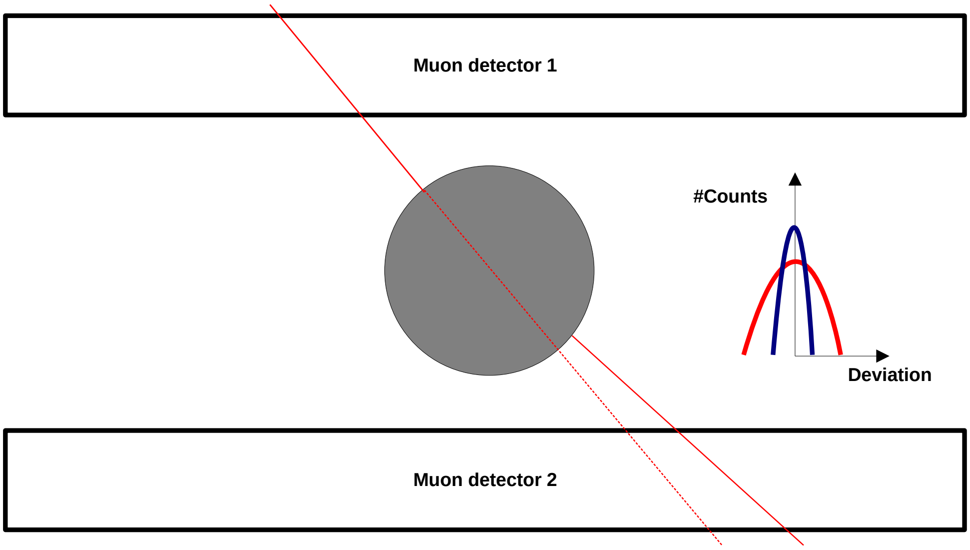

Figure 2.12: Muon Scattering Radiography (MSR) scenario example. Two muon detectors are located measuring an industrial pipe, one of them over the target, and the other below. On the right, the probability distribution of measured muon scattering angles ($\Delta\theta$) with and without target.

Muon momentum

Momentum is of great influence when performing a muography, specially when measuring scattering. As eq. (2.21) indicates, it is inversely proportional to the RMS of the scattering angles of muons. In addition, muon momentum range covers several orders of magnitude, and although its mean value for muons at the Earth surface is around 4 GeV, it strongly depends on the incidence angles of the measured muons, especially on the zenith angle (see section 2.2.2). Therefore, the momentum distributions of measured muon fluxes depend on detector configuration and orientation.

Due to these reasons, to measure or estimate the muon momentum on a per-particle basis can be a major improvement for muography. It directly improves the output of muography algorithms, as allows a more precise reconstruction of absorption and scattering phenomena. The momentum of a particle can be inferred based on its time of flight, or also using calorimeters and detectors, measuring the deposited energy or other indicators, such as the scattering in the detector material, technique that has been already tested in the area of muography [58]. The use of dense material layers placed between detectors has been proposed too, with the aim of filtering and classifying muons of different ranges of momentum [59] [60], or to directly estimate it [61]. It should be borne in mind that when adding detection layers the angular acceptance and efficiency of the whole system is undermined. However, the improvement of muon imaging has been demonstrated with a detector including a dedicated momentum spectrometer [62].

The latter technique has been studied in this thesis and applied to material discrimination (appendix B).

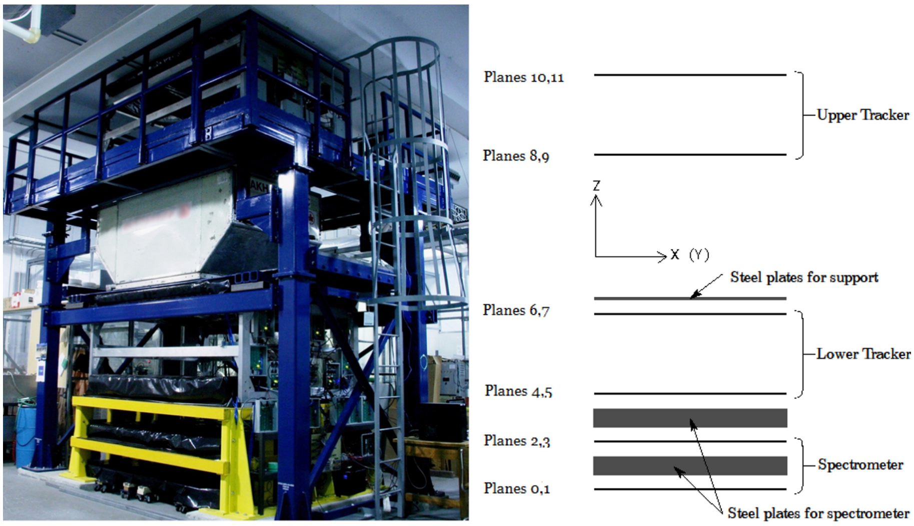

Figure 2.13: Photograph and explanatory sketch of the detector with dedicated momentum spectrometer used in [62]. [8]

2.3.2 Types of detectors

In this section, the existing types of muography detectors depending on their detection technology are enumerated, together with their main characteristics. Emphasis is placed on gaseous detectors, and more specifically on Multi-Wire Proportional Chambers (MWPC), which is the technology utilised to build the detectors studied in this thesis.

The requirements of a detector built for MAR applications are usually less demanding comparing to MSR detectos in terms of resolution. In the case of MAR, the resolution affects the accuracy with which the detected muons are reconstructed, but not the main magnitude that is used to estimate the density distribution of the scanned volume, i.e., the muon counts which indicate the absorption. On the other hand, in MSR, the resolution influences both, the accuracy of the location of the measured muons trajectories, and also the scattering angle measurement, which is used to infer the scattering density of the materials within the detection volume. The requirements also depend in the targets of each specific application.

Regarding the muon momentum measurement on a per-particle basis, despite attempts, there is still no technology that has been widely applied in the field of muography, both because of the cost of the hardware needed to do so and due to the technical complexity that the task involves.

Scintillators

Detectors composed of plastic scintillators are typically used in MAR measurements, since their resolution is not optimal comparing to other technologies. On the other hand, they are robust and relatively cheap systems (roughly 50k €/m^2) [51]. The emergence of Silicon Photo Multipliers (SiPM) has reduced the cost and power consumption of scintillator detectors. Light guides and Wavelength Shifter Fibres (WLS) are the mechanisms used to collect the photons emitted by the particles along their path through the scintillators. The output of the mentioned mechanisms is connected to photo multipliers and then to the readout electronics. WLSs and SiPMs have been used in MU-RAY [63], among other detectors (see fig. 2.14).

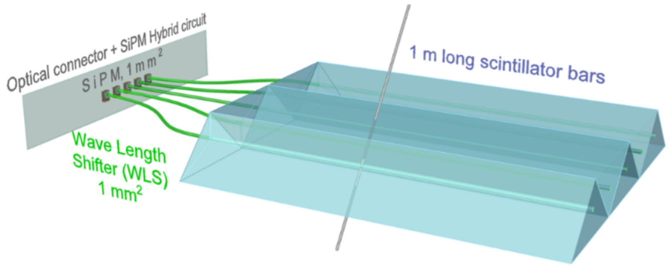

Figure 2.14: Simplified sketch of a scintillator using Wavelength Shifter Fibres (WLS) and Silicon Photo Multipliers (SiPM). [9]

The operation of this type of detectors is highly dependent on temperature, and the voltage has to be adapted to its variation. Other approach to solve this issue, the use of temperature control systems that maintain a constant temperature inside the detector, has been applied in the MURAVES experiment [64].

It is worth mentioning that two special types of detectors have been developed with scintillators: novel borehole detectors which are useful for underground applications [65] [66] [67], and MSR detectors based on thin scintillator fibres [68].

Nuclear emulsion

These detectors are composed of extremely high spatial resolution photographic layers, even below the micron, depending on their grain density. Charged particles leave a three-dimensional trace in their interior which can be seen and reconstructed by means of microscopes and specific equipment. These detectors are lightweight, and they can reach angular resolutions of the order of a few mrad [69]. They do not need electric power, but the reconstruction of their measurements is not a real-time process, and involves the use of complex and quite uncommon equipment. In addition, their operation it is adversely affected when working with low temperatures, and in humid atmospheres [51].

Such detectors have been utilised in diverse and harsh scenarios [70] [71] [72]. They have been one of the three technologies used by ScanPyramids collaboration in the discovery and characterisation of a big void and a structure that resembles a corridor in Khufu's Pyramid [73] [74].

Semiconductor

Silicon, or semiconductor detectors are robust, reliable, and high resolution systems, but their price is high compared to other detection technologies typically utilised in the field of muography. The detection units can be pixel or strips, having the former greater ability to differentiate events, but at the expense of important requirements regarding the electronic acquisition system. This type of detectors can reach resolutions of 10 μm [75].

Cherenkov radiation

Cherenkov radiation systems have been tested as muography detectors, for example in MAR applications in vulcanology [76], and also in MSR applications as momentum estimators [77]. However, due to their high cost they are not a widely used technology in the field of muon radiography. The Cherenkov light is produced when a charged particle traverses dielectric material at a velocity greater than the speed of light in the same medium (phase velocity). Thanks to this electromagnetic radiation, particle trajectory and speed can be reconstructed, since the angle of the cone-shaped light which is emitted is related to particle velocity.

Gaseous

Among gaseous detectors different sub-types exist. For example, drift chambers, micromegas, Resistive Plate Chambers (RPC), and Multi-Wire Proportional Chambers (MWPC), the detection technology studied in this thesis. They all share common characteristics such as a high angular resolution, and reduced financial cost, both particularly desirable requirements for scattering muography detectors. However, this sort of detectors are used both in MAR and MSR applications, and they are usually built with flat shape, although borehole gaseous detectors also exist [78]. Charged particles traversing the volume filled with gas inside the detector collide with the atoms of the gas and release electrons from them. Thus, the atoms become ions, and due to the action of the electric field within the detector they are drifted towards the cathode, while electrons are attracted by the anode. Depending on the gaseous detector sub-type, the detection units, that is, anodes and cathodes, can be tubes, strips, plates, or proportional wires.

Multi-Wire Proportional Chambers (MWPCs), were invented in 1968 [79]. In this first implementation the MWPCs already showed the possibility or reaching excellent time resolutions of up to 100 ns. The wires worked independently down to separations of 1 mm. The appearance of MWPCs entailed a revolution in the field of particle detectors, due to the aforementioned improvements in position resolution and in the ability of distinguishing particles with high arrival frequencies. These detectors are composed of an anode plane usually made of wires, or alternatively of other components, such as strips. This plane is in between of two cathode planes. Arranging two anode planes perpendicularly and close to each other, just below one another, the points where charged particles cross the chamber can be estimated. The passage of charged particles through the detector volume filled with gas produces ionisation, and as explained above, the electrons take direction to the anodes, in this case, the wires. When approaching them, the electrons are multiplied and produce avalanches (see fig. 2.15), which are usually collected on the nearest side of the wire, and do not surround it. In this way, signals are produced in the anodes, which are transmitted to their receivers in order to capture them. The mentioned avalanche effect is described by the Townsend coefficient, and depends on applied electric field, gas density, ionisation cross sections of collected electrons, and other transfer mechanisms [80]. The Townsend avalanche is the phenomenon behind the amplification factor of the anode wires, which are also called proportional wires due to the proportionality of the signal they generate with relation to the number of electrons collected. This proportionality is maintained as long as the electric field disturbance produced by the avalanche is negligible compared to the electric field of the wire.

MWPC variants like the Cathode Strip Chambers (CSC), which use segmented cathodes and provide excellent spatial resolution and high counting rate capabilities have been installed, commissioned, and tested in ATLAS detector of LHC (Large Hadron Collider) [81]. These CSCs have wire and strip pitches of 2.5 and 5 mm, respectively. The position resolution in the precision coordinate is roughly of 60 μm, and it is obtained through interpolation of the induced charge on the segmented cathode. In addition, in the case of events with more than one track, pulse height helps

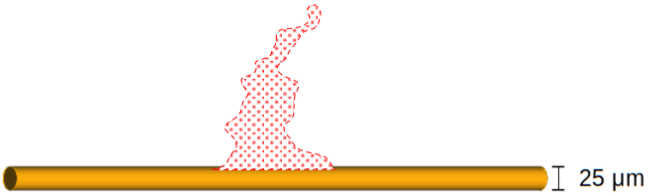

Figure 2.15: Rough representation of an electron avalanche in the vicinity of an anode wire.

to identify and match tracks of precision and secondary coordinates belonging to the same particle.

Recently, innovative designs of MWPCs adapted to requirements of muography have been developed too. As an example, the construction of chambers with uniform and high detection efficiency (above 99%), and a low gas consumption of less than 2 liters/hour [82]. The utilised gas is an argon and carbon dioxide mixture, which is nontoxic and nonflammable. It was proven that the position resolution of the detectors was compatible with the expectation of a 12 mm spacing between wires, i.e, 3.5 mm (assuming uniform hit distribution). Such detectors have been applied in absorption mode in natural caves and artificial tunnels [83], in Sakurajima volcano [84] [85] [86], and also in a civil engineering application, where an underground iron pillar was imaged using a borehole detector [87]. A rotating 5 metre length MWPC-based muon spectrometer has been built too, which is used to perform precise momentum measurements [88].

The main drawbacks of MWPCs are the fragility of the wires, and complex construction and maintenance. The effects of temperature change require a compensation, which can be solved with voltage regulation [82].

Regarding Resistive Plate Chambers (RPCs), the first detector of this type was developed in 1981 [89]. The detection mechanism is composed of high resistivity parallel plates with constant gaps between them. The plates are coated with a low resistivity material, typically graphite. Comparing to other gaseous detectors, a higher electric potential is needed, approximately 10000V are applied to the coating. RPCs are reduced cost detectors, and their manufacturing is simple compared to other muography detectors. On the other hand, they require extremely high voltages, can be damaged by sparks, and they use flammable, and even restricted gases. High Global Warming Potential (GWP) gases, such as the ones used in the RPCs (namely C2H2F4, and SF6) have been restricted by European regulations. For this reason, it is envisaged analysing the performance of RPCs using eco-friendly gases [90].

In 2000, the RPCs were already utilised as triggering detectors in ATLAS experiment, reaching a timing resolution of 3 nanoseconds [91]. Later, a high resolution detector prototype (300 μm spatial resolution) was developed for scattering muography [92]. In 2019, a exploration of small-area RPCs intended for use in muography applications with complicated logistic conditions was suggested [93]. Currently, research activities and manufacturing of portable muon detectors based on Resistive Plate Chambers are being carried out [94] [90]. RPCs have been applied in Puy de Dôme volcano, providing useful information about the performance and requirements of detectors for volcano absorption muography [95].

The drift technique consist in measuring the time of the travel of the electrons through the gas within the chamber until they reach the anode wire. With this magnitude, the distance between muon trajectory and the detection wire can be inferred. This technique can be applied in drift chambers made of tubes, or also of proportional wires. However, it should be borne in mind the influence of various factors on on drift velocity, such as temperature variation, and the ratio of electric field to gas pressure [51]. By taking advantage of the high resolution that can be achieved with this technique, detectors based on it have been used to perform scattering muography measurements where nuclear threat [96] detection, and material characterisation [60] have been studied.

Micro-Pattern Gaseous Detectors (MPGDs) are a new generation of detection mechanisms composed of microelectronic structures. In those detectors, the distances between anode and cathode electrodes are below millimeter scale. Their performance regarding rate capability, time and position resolution, granularity, stability and radiation hardness improves that of the MWPCs. Currently, a collaborative effort is being made in order to make MPGDs a viable, easy-to-use, and cost-efficient technology for construction of large surface and portable detectors [97]. A sub-type within MPGDs, the MICRO-MEsh GAseous Structure (MICROMEGAS) detectors have been already tested in controlled environment and used to perform MAR measurements in a dam in the South-East of France [98] [99], as well as in Khufu's Pyramid, in the framework of the ScanPyramids project [73].

As a concluding remark about gaseous detectors, the need of a continuous gas flux has to be considered, which in case of large surface detectors can be high. This fact could difficult or limit their operation and performance in certain applications.

2.3.3 Simulation

In this section, the particle physics simulation tools used in the research are described. The simulation consists of three main aspects: muon generation, their propagation trough matter (transport), and the detector response.

The utilised simulation framework generates muons mainly by means of the Cosmic RaY generator (CRY) [100]. CRY is a cosmic-ray particle shower generator library, which provides data at three different elevations above sea level: 0, 2100, and 11300. The primary cosmic ray production is based on simulation tables verified by means of published cosmic-ray measurements. It can generate muons, neutrons, protons, electrons, photons, and pions. The generation can be configured, activating or eliminating the aforementioned types of particles. They are generated within the selected generation area (a flat and squared surface, with configurable side length), taking into account the flux corresponding to the specified conditions. The latitude and solar cycle effects are also considered, and they can be managed by the user. The Efficient COsmic MUon Generator (EcoMug), which is based on experimental data parameterisation, is also within the framework and can be used to generate cosmic muons [101]. It is particularly designed for muography applications, and it allows to produce muons from different surfaces, such as planes, cylinders and half-spheres. This feature allows to simulate certain scenarios in more efficient way compared to squared surface generators, such as CRY. The generation of background events has been recently included [102], among other improvements. Both, CRY and EcoMug, reproduce the atmospheric muon flux arriving at the Earth's surface, which is the information used in this thesis.

GEANT4 [103] is used to simulate particle propagation through matter. GEANT4 is a particle transport simulation software, designed and maintained at CERN, which simulates particle-matter interactions in high energy and nuclear physics. A detailed summary of the aspects of Geant4 related to muon tracking can be consulted in [104], while the physics reference manuals, together with the rest of Geant4 documentation can be found in [105]. The key Geant4 processes for the studies performed in this thesis are those related to muon transport, and in particular their energy loss and scattering phenomena.

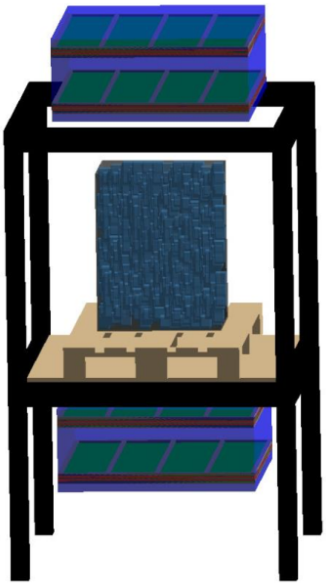

Figure 2.16: Visualisation of the experimental muography detector model included in Muon Systems simulation framework.

The simulation framework used in this research contains a model of the muography detector utilised including its response (see fig. 2.16). This framework has already been successfully applied to various use cases, such as steel pipe wear [106] and the application to hidrology included in this thesis [107]. Similar simulation frameworks are commonly used in muography applications [108]. It is worth mentioning that both perfect and realistic resolution detector response can be generated with the simulator. In the case of realistic resolution, the muon trajectories are reconstructed by the wires of the detection layers, that are included in the simulation. The closer wires to the actual position of the muon are activated, and their amount is determined depending on muon incident angle, based on a model extracted from laboratory measurement data (see section 3.3.1). Perfect resolution simulation provides the actual muon position in the detection layers, as generated by Geant4.

2.3.4 Muon reconstruction algorithms

In the current section, different types of muography algorithms used to reconstruct muon signals are explained. Specifically, imaging, and parameter inference algorithms are reviewed. The section is mainly focused on scattering muography.

Muon imaging algorithms

The *Point Of Closest Approach* (POCA) algorithm [109] [110] is a simple and effective muon imaging algorithm widely used in scattering muography field. It is based on an extremely simplified view of the multiple scattering, in which a single scattering centre is only considered. This centre (P_{poca}) is inferred calculating the closest point to both, upstream and downstream muon trajectories (see fig. 2.17).

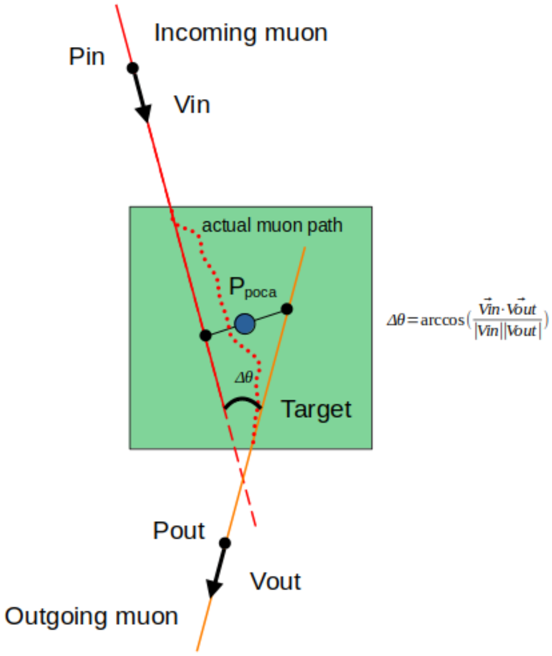

Figure 2.17: Sketch of the POCA algorithm calculation.

The algorithm is highly dependent on the trajectory resolution of the detector utilised, and it is characterised by a lack of accuracy in the axis perpendicular to detection layers, which is emphasised for muons with low deviations. This kind of muons, which are presumably of high-energy, can be an important part of the measurement containing significant information. Even with a perfect resolution detector, scattering centres inferred with POCA for energetic muons traversing light materials can be very imprecise or even undetermined. In those cases, the expected initial and final muon trajectories are almost parallel. They should be considered also cases where the reconstructed tracks tend to drift away from each other.

A version of this algorithm has been applied in some analyses of this thesis to reconstruct the scattering density distribution of different targets, such as cargoes composed of several materials (see appendix C), and concrete cylinders (see fig. 2.18). It has been also utilised as input for a furnace ladle fill-level inference model developed in section 6.3, which has been recently applied by TomOpt [111] collaborators to differentiable-programming detector parameter optimisation [112]. The implemented model is essentially a general and efficient algorithm which estimates the thickness of a layer of material.

The *Angle Statistics Reconstruction* (ASR) algorithm [113] was proposed as an alternative to the above described POCA. It was designed with the aim of reducing inaccuracies inherent to POCA

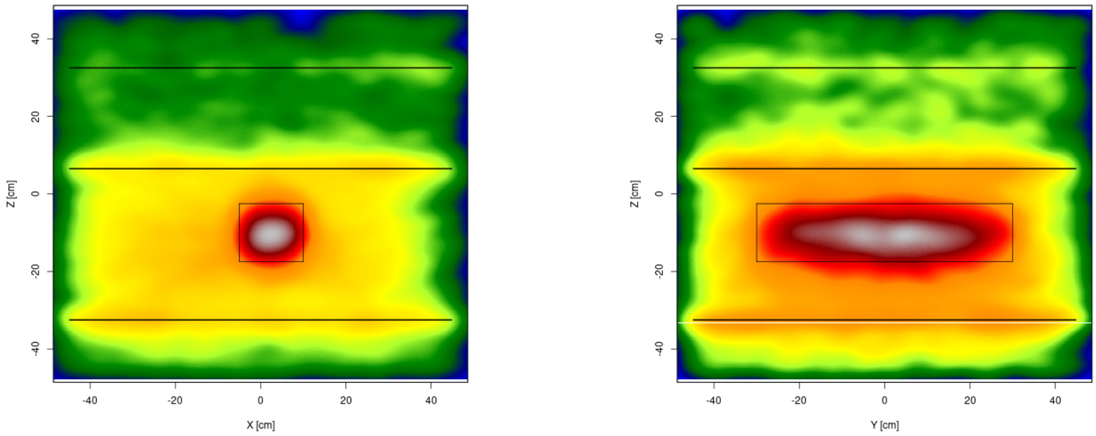

Figure 2.18: POCA point density tomography of two concrete cylinders, with same dimensions, and located next to each other. The volume where both of them are located is marked with black rectangles.

algorithm, such as those already described in the previous paragraphs. ASR reconstructs the scattering in a grid of voxels depending on the distance between incoming and outgoing trajectories. A maximum threshold distance is defined, which determines the scattering existence in the voxels. When the trajectories are closer than...

The *Maximum Likelihood Expectation Maximisation* algorithm [114] [115] approaches the detection volume scattering density reconstruction as a multi-parameter estimation problem. The detection volume is divided in voxels, whose radiation length is estimated based on a statistical scattering model. Maximising the likelihood function by means of expectation maximisation techniques, the scattering density distribution of the volume of interest is inferred. The algorithm has been multiple times re-explored, although it requires muon momentum information, a magnitude which is not usually measured with precision in a per particle basis by common scattering muography detectors. [116] is a recent implementation example. Detailed information about the mathematical basis of the algorithm can be found in [117] [118].

In this thesis, an alternative imaging algorithm has been developed and applied, which consists in reconstructing the scattering density of concrete cylinder vertical sections. It is adapted to the known volume and location of the target, and based in muon trajectory projection and deviation statistical analysis. Its detailed explanation and application to laboratory experiments can be found in the chapter 4.

Parameter inference algorithms

Algorithms based on the modelling of parameters about the detection targets have been also applied to several use cases. Parameters of interest, such as the thickness of a target, or its amount of matter have been modelled based on muography inputs. The utilised inputs have been scattering angle, and POCA point distributions.

Muography measurements involve several factors that can produce significant variations in the measured variables, such as background particles and other source of noise, chamber alignment, detector material, or the resolution of the system. They prevent of directly solving in a precise way the inverse problem based on scattering models, due to bias produced by the aforementioned factors. Therefore, all of them should be taken into account in order to perform accurate reconstruction of the volume of interest.

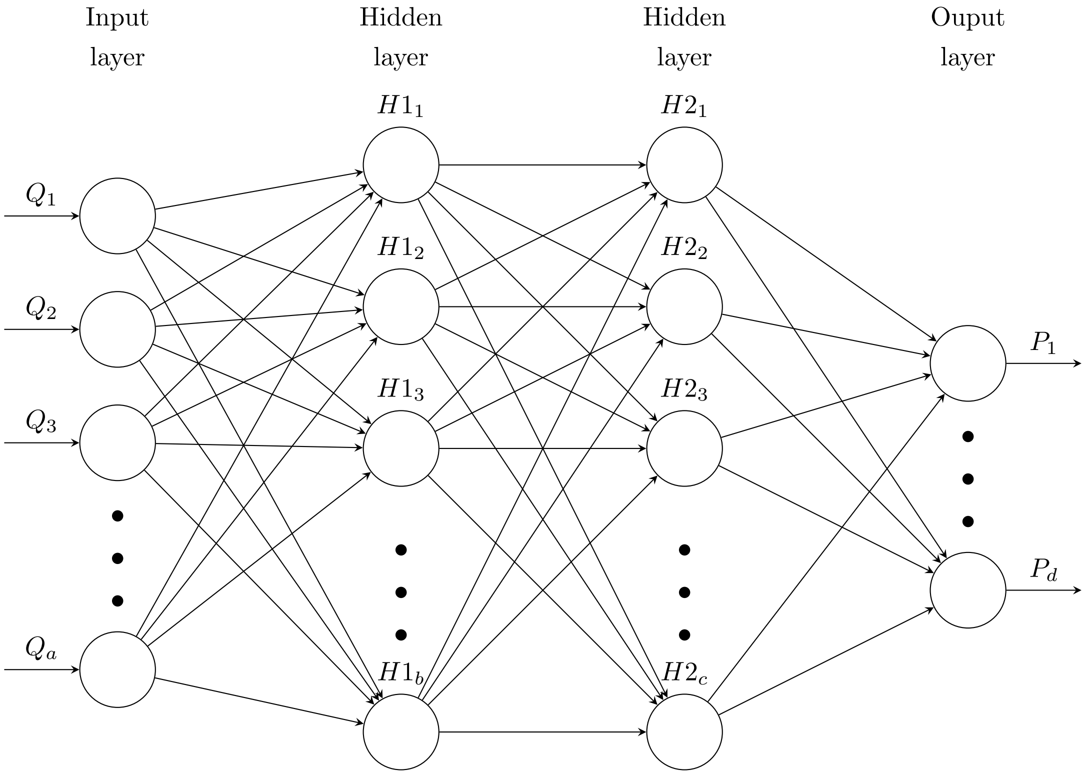

Figure 2.19: Illustration of a generic NN using as inputs a quantiles (Q_a) of probablility distributions of variables measured trough muography (e.g., scattering angles and displacements, POCA outputs) to model their relation with d parameters of interest (P_d).

This issues can be handled by models fitted to sets of data with representative cases in which the parameters of interest have been varied. In this manner, the relations between measured muography variables and the parameters describing the detection volume are learned, together with the uncertainty factors mentioned in the previous paragraph, which depend on the specific muography detection setup utilised. The parameter variation of the fit data should represent well and completely cover the cases that want to be solved. This type of models have been used in this thesis in chapter 5 to estimate the *Snow Water Equivalent* (SWE) evolution of the snowpack, and also in appendix B to characterise material mixtures. In the case of SWE estimation, single input and output models of the relation between the RMS of muon scattering angles and the SWE have been utilised. For material characterisation, Neural Network (NN) models have been trained to learn multiple parameters about a material mixture. The quantiles of the measured muon scattering angles have been used as inputs of the NN models. Similar models has been already applied to industrial electric arc furnaces, in order to estimate the position of their carbon electrodes [61]. A generic sketch representing this type of models is shown in fig. 2.19. As already mentioned, a furnace ladle fill-level inference model has been also developed. This algorithm is an additional example of parameter modelling approach, in this case using POCA point distributions.

2.3.5 Applications

In the following, different applications of muography are reviewed. They are developed in several areas ranging from industrial production and civil engineering to natural sciences like geology.

Civil Engineering

The first application of MR was carried out in 1955 and it involved the MAR inspection of the overburden of a tunnel with a movable detector [119]. This same application has been repeated recently in a UK railway [120]. In the latter campaign, a hidden shaft in the tunnel overburden has been discovered.

In relation to the application of MSR in world heritage buildings, studies and laboratory experiments have been done to confirm the feasibility of measuring and assessing the state of reinforcement elements in the dome of Florence Cathedral Santa Maria del Fiore [121, 122].

Other explored civil engineering applications are stability monitoring of historical buildings [123], building interior mapping [124], and sewer pipe positioning [78]. Regarding reinforced concrete block assessment, a first proof of concept with experimental measurements has been already done [125]. Simulation studies about rust detection in steel bars encased in concrete have been performed too [126]. In this thesis, in the chapter 4, the detection feasibility of subtle defects in concrete cylinders is analysed by means of laboratory measurements.

Archaeology

In the field of archaeology, MAR was applied for the first time in the 1960s, at the Chephren's Pyramid in Giza (Egypt). The objective was to investigate the existence of hidden chambers, and it was concluded that chambers of these dimensions do not exist in Chephren's Pyramid [127]. The campaign of measurements performed in the Pyramid of the Sun built by the Aztecs at Teotihuacan (Mexico) had the same objective. A lower density area in the southern side was reported, concluding that its probable cause was a structural weakness [128, 129]. In a Mayan site in Belize, called La Milpa, MAR has also been applied to search hidden chambers [129, 130]. Recently, a big void, among other cavities, has been discovered in the Great Pyramid of Giza. The discovery has been confirmed by three different muography teams of the ScanPyramids project which have used different detection technologies [73]. The last research of the aforementioned project has resulted in the characterisation of a corridor-shaped structure, which was other of the voids found in the previous campaign [74]. The discovery of a cavity in the Mount Echia, in Naples (Italy), is another example of the potential of MAR to obtain information about these sorts of archaeological constructions [131, 132, 133].

Hydrology and other geoscience areas

Hydrological problems have been also addressed with means of muography. Regarding the *Snow Water Equivalent* (SWE) inference, the potential of muon counters to achieve it has been proved comparing the decreasing muon count rate with in situ SWE measurements performed in a Swiss glacier [134]. It was concluded that the muography detection method used is a promising technique that has advantages comparing to neutron detectors. It is worth mentioning that the SWE is defined as the height of the resulting column of water if the snowpack melted, and it is usually measured in mm. In the chapter 5 of this thesis, a summary of the recent research about the application of scattering muography to SWE inference [107] is included. It should be mentioned that MAR has been also utilised to study the ice-rock interface in glaciers [70, 71].

MAR has been applied by multiple research groups in the field of vulcanology. The applications have been carried out in different volcanoes, such as Stromboli [72], Vesuvius [135, 131, 64], Etna [136], and Puy de Dôme [137, 95] in Europe, La Soufrière de Guadeloupe [138, 139] in the Caribbean sea in America, as well as Asama [140], Satsuma–Iwojima [141] and Sakurajima [85] in Japan.

Other representative applications to the area of geology involve natural cave [142, 83] and other underground explorations involving material and cavity identification and mapping [143, 144, 78, 145].

Manufacturing industry

Many applications in the field of manufacturing engineering are related to industrial furnaces. The reconstruction of the interior of blast furnaces [58, 146] has been already studied, and an European project has been launched in order to validate that muography could be a useful tool for this purpose [147, 148, 149]. Carbon electrode localisation in electric arc furnaces has been analysed too [61], as well as filling-level of furnace ladles [112].

Scrap metal inspection [150, 151, 58, 60], and pipe wear detection [152], even under insulation [61] are other industrial application examples of muography.

Cargo inspection

Containers and vehicles carrying cargo related to different activities are scanned by means of muography. Security inspection applications have been developed in order to detect nuclear material, sometimes combined with additional technologies, such as X-ray, neutron, and γ ray detectors [153, 78, 154]. The scrap metal scanning, which has been already mentioned among the manufacturing industry applications, also has among its objectives the detection of nuclear material.

In 2012 a muon portal was installed in Freeport, in Bahamas. With this portal thousands of cargo containers were scanned. However, the project ended due to damages produced by a hurricane [155]. Currently, new research is being developed regarding cargo inspection muography portal construction. As examples the European project Silent Border [156], and the Spanish Muon Cargo [157, 158], of which preliminary analyses are presented in this thesis, in appendix C. A recent review of muography technology applied to cargo scanning can be found in [159].

Nuclear energy

Spent fuel and nuclear waste monitoring [160, 161, 162, 58, 68] are examples of muography applications to the field of nuclear energy. The technology has been also used in the nuclear power plant of Fukushima in order to scan the reactors after the nuclear crisis [163, 164, 165, 166]. Recently, two abandoned Soviet nuclear submarines containing encased reactors have been inspected [167, 168].

Chapter 3

Commissioning of a MWPC-based muon detection system

3.1 The detectors of Muon Systems

In this section, the muon detectors built and exploited by Muon Systems are described. Muon Systems is the company where this industrial PhD is developed. The detectors built, studied, and utilised during this PhD project, consist of several MWPCs, whose working principles have been explained in the previous chapter (section 2.3.2).

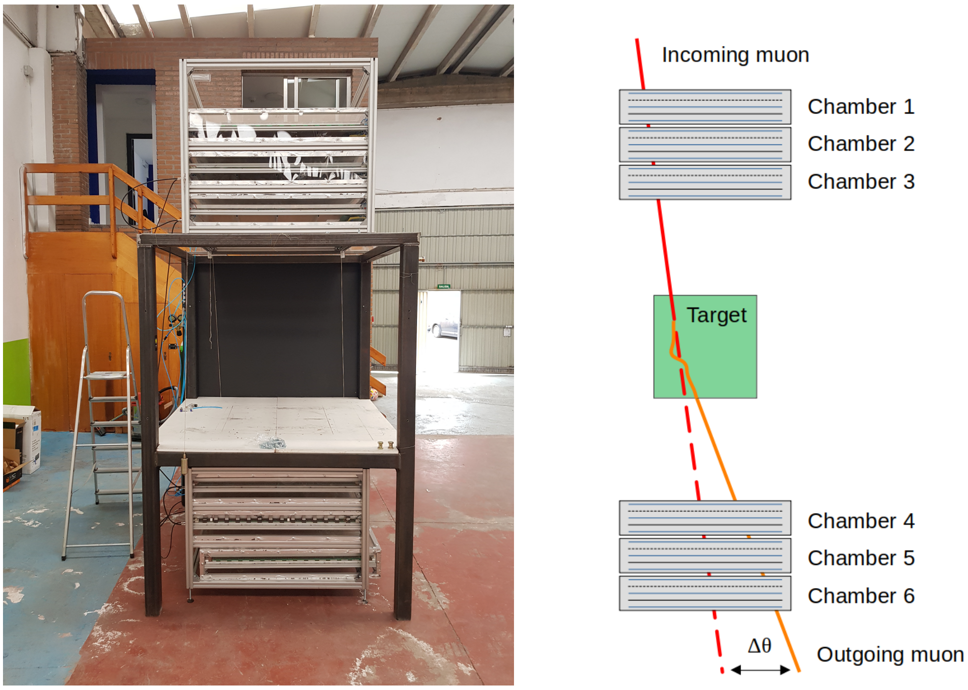

Figure 3.1: On the left, the detector built by Muon Systems, installed in the industrial site of the company. On the right, a sketch representing a muon measurement.

Muon Systems detectors are currently employed to perform laboratory scattering muography measurements of representative samples from several applications in different fields, namely manufacturing industry [61], civil engineering [169], and hydrology [170]. Similarly designed MWPCs with smaller detection surface have been already tested in underground railway tunnels [158] (see fig. 3.2). In the following lines, aspects related to the design, electronics readout, synchronisation (trigger), and data acquisition system (DAQ) of the mentioned detectors are discussed.

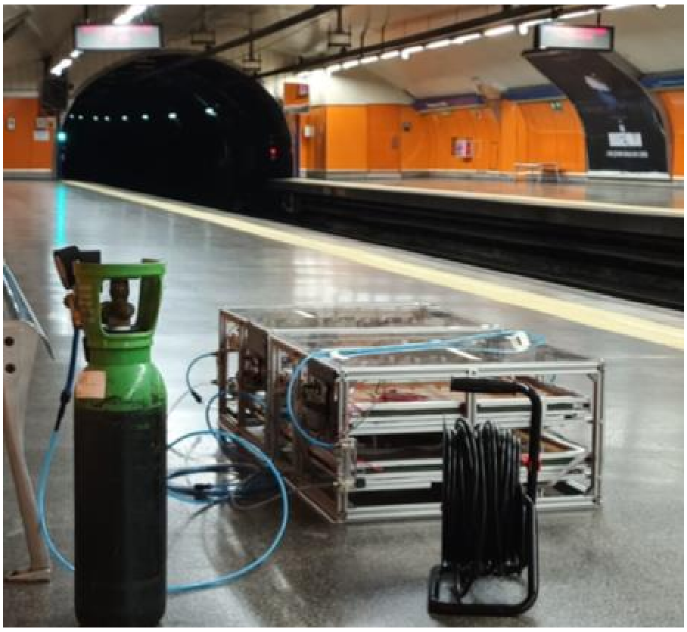

Figure 3.2: Muon Systems MWPCs prepared for the first tests performed in underground railway tunnels.

3.1.1 Muon chamber design

Muon detectors manufactured by Muon Systems consist of Multi-Wire Proportional Chambers (MWPCs), which in turn, are formed by two position detection layers with 4 mm separated wires (see fig. 3.4). Therefore, they provide a position resolution of 1.2 mm considering a uniform particle hit assumption (see section 3.3.5). Two anode wire planes are located between parallel cathode plates (one is between the two wire layers, and the other two are placed in the exterior, above and below the upper and lower wire planes), which cover the whole chamber, whose active detection area is of 89.6 x 89.6 cm^2. The basic configuration used requires only 4 MWPCs, although more chambers can be added to improve the muon reconstruction. The detection performance of the system using 6 MWPCs is also studied in this thesis (see fig. 3.5).

The detection wires are composed of 99.95% purity tungsten, plated with 99.99% pure Gold. Their diameter is 0.025 mm. It is worth mentioning that 224 wires with a length of approximately 90 cm have been welded in each of the layers of the MWPCs. In the borders of the chamber, two additional wires have been added not for detection purposes but to compensate the electric field. These wires are made of copper, with a diameter of 0.1 mm.

A tool has been used to guide and give the right tension to all the wires. In addition, it has been mechanically ensured that the cathodes are kept at the right distance from the wire planes, in particular by preventing them from getting too close to each other in the central area of the chambers. Obviously, this is important for a correct operation of the detectors, since the two conductive elements, anode electrodes and cathode, the wires and the metallic plates, must be isolated and at

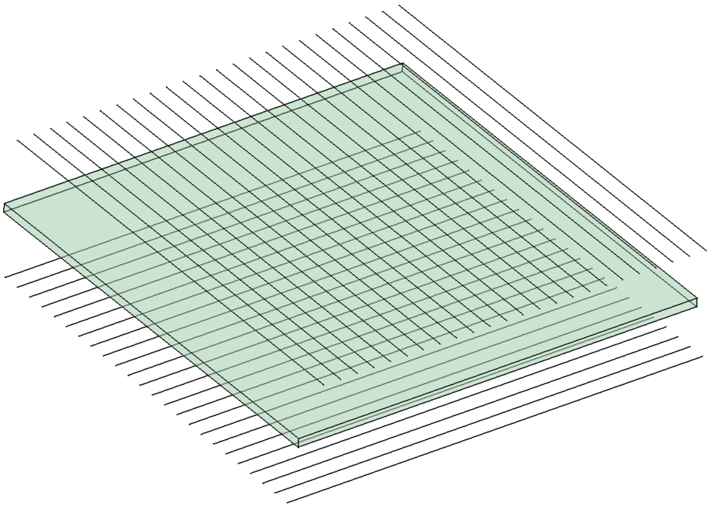

Figure 3.3: Sketch of a reduced (9.6 x 9.6 cm^2) 2D grid of detection wires with a central cathode, following the design of Muon Systems MWPCs.

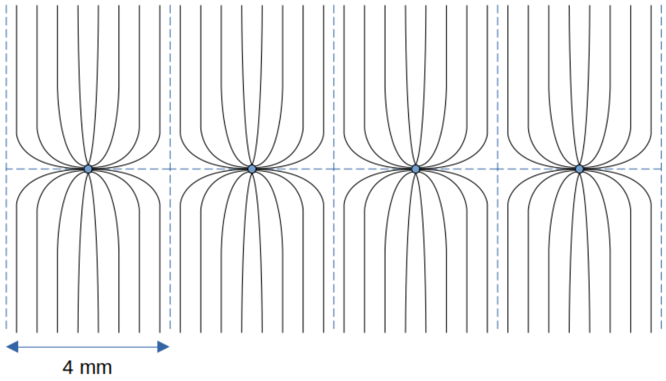

Figure 3.4: Sketch of the electric field lines close to anode wire plane location.

a different electrical potential. Photographs of the manufactured MWPCs are shown in fig. 3.5.

In principle, the detectors have been designed to work with an anode voltage around 2150 V, which can be dependent on environment conditions and other detector system variables, such as the gas flux. In this thesis, efficiency of muon detection for different anode voltages is analysed in order to check which is the optimal operation point in terms of anode voltage, for controlled and stable conditions of gas flux, temperature, and humidity in the laboratory section 3.3.2. The detection system uses an industrial gas mixture with Ar and CO_2 (15%), whose flux can be maintained constant at an optimal operation point, or regulated automatically depending on signal noise ratio.

3.1.2 Electronics: Readout, and synchronization system

The electronics readout and the trigger system are made up of custom electronic boards. The electronics readout system collects the signals from the wires, amplifies them, and converts them into digital format. Each board handles the signals of 16 anode wires and has a configurable threshold for pulse identification. To form a full detection layer (224 wires), 14 boards are required.

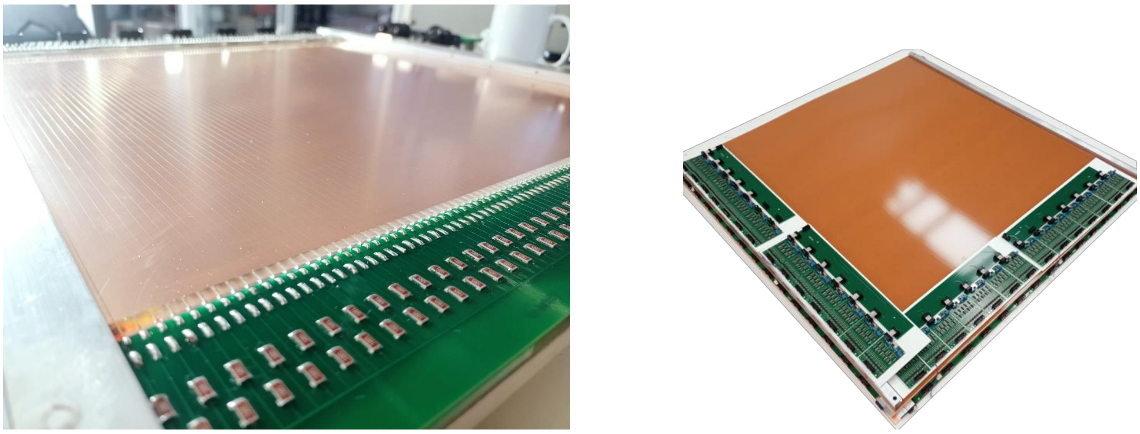

Figure 3.5: Left: Muon Systems MWPC with the top cover opened. The anode wires, their electronic connections, and the lower cathode can be observed. Right: Muon Systems MWPC with its readout electronic boards.

The trigger, or synchronisation system, is based on a set of registers and a microprocessor that gives the order of readout whenever it finds an activation in a predefined number of layers. The acceptance time window of the trigger system is of the order of microseconds, while the time needed by the master to manage and process the data to send it to the acquisition computer is of some milliseconds.

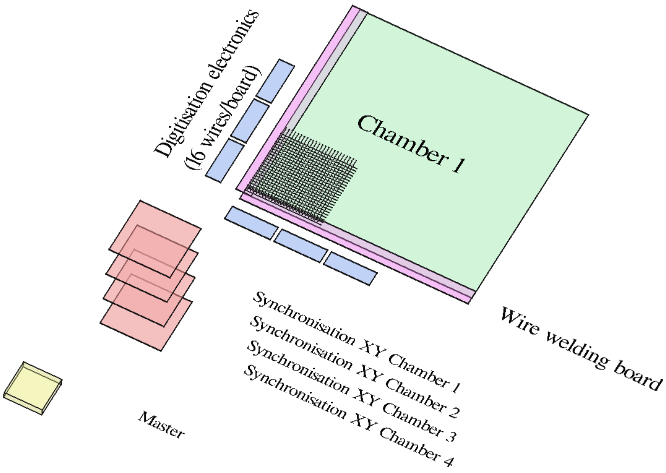

Figure 3.6: Detection system illustration. Anode wires, their welding boards, and the central cathode of upper chamber 1 are represented. The main parts of electronic readout and synchronization system are also shown, namely, pulse digitisation boards, chamber level synchronisation boards, and the master microprocessor.

The characteristics of the muon flux and also the particles that can leave a signal in the multiwire chambers are of vital importance for the correct functioning of the synchronisation system, and thus of the whole detection system. In this sense, the flux of charged particles is a key factor in the design of electronic acquisition systems, as it should be able to distinguish between them.

When an anode wire of the detection system generates a pulse, it activates the trigger electronics and a time window is opened to check if pulses are originated in the other triggering chambers. The goal of such a system is to distinguish signals produced by muons that cross all the synchronisation chambers, from other type of spurious signals that can activate the detection wires. Note that wires can collect signals generated either by muons, by other charged particles, or by noise in the chamber.

In this context, the time interval between subsequent muons is a parameter that helps to define the requirements for the electronics and also to understand its limitations and the probabilities to acquire noisy events. The higher is the muon flux detected, the more demanding the time resolution of the triggering system. In the case that in the same time window two muons activate detection wires, signals produced by both muons will be included in the acquired event, making difficult their discrimination and reconstruction. Furthermore, it also has to be considered the cases when other charged particles such as charged hadrons, electrons, and positrons (background noise, or "fake muons") activate the detection wires. The abundance of these particles at sea level and above an energy of $1\tilde{G}eV$ is roughly two orders of magnitude smaller compared to the muon flux, but it should be also taken into account for detectors without momentum cut like the one utilised in this research. Hence, when analysing and interpreting data acquired with the detectors, this phenomena will be considered.

3.1.3 Data Acquisition system

The Data Acquisition System (DAQ), which is represented in fig. 3.6 for the particular case of 4 MWPCs, is composed of the set of readout electronic boards and the master electronics already described in the previous section. They process the analogue pulses collected by the anode wires and convert them into digital pulses. The digital signals are synchronised firstly at chamber level, and then at detector level, based on a system of delays. The system allows to choose the chambers used for triggering. Therefore, the measurements can be performed with different detector level synchronisation configurations. The master microprocessor is responsible for checking the trigger information, and collecting the data from all the chambers when activation pulses are acquired in the triggering chambers.

All the events collected by the master are stored and sent to a computer via a USB connection following a data protocol. The DAQ workflow is shown in fig. 3.7. The last step, indicated with a green box, represents work done during this PhD related to wire activation decoding, subsequent analysis, and algorithm implementation. These developments involve the study of filtering strategies and Smart Tracking, which eventually lead to optimal muography reconstruction and inference, the final objectives of this thesis.

3.2 Event reconstruction

3.2.1 Trajectory building

The reconstruction of the acquired signals is performed as follows. Activated wires are translated into local coordinates (X_C, Y_C, Z_C) using the geometry description of the chambers. If more than one wire is activated in the same layer, the mean is used as the muon position. Using again the geometry description, local coordinates are transformed into a global coordinate system, and

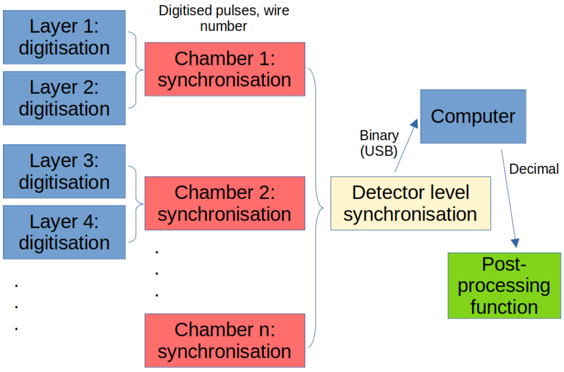

Figure 3.7: DAQ workflow graph representing wire pulse identification and digitisation, chamber and detector level synchronisation, and data transmission to the acquisition computer through USB connection. Electronic binary data is converted to decimal format following a data protocol. The green boxes represent developments carried out within this PhD: a *post-processing function* to decode the wire activation information, and the subsequent analyses and algorithms.

the entry and exit trajectories of the muon are estimated, i.e., their position (X_D, Y_D, Z_D) and direction (vX_D, vY_D, vZ_D). These trajectories are reconstructed in the upper and lower detectors by performing a linear fit to the detected muon positions. The angular deviation projected in both horizontal axes ($\Delta\theta_X$, $\Delta\theta_Y$) are calculated from the direction vectors.

3.2.2 Post-processing: event filtering and quality criteria

A *post-processing function* which reads all the events collected by the DAQ, has been implemented. It extracts the wires activated in the different layers in each event for their subsequent analysis. This tool checks the quality of each measurement, monitoring the presence of background noise and other possible disturbances. This analysis aims to provide information to improve the calibration of the chambers and to identify anomalous or inadequate operation. Another target addressed by this code is the adoption of an optimal filtering strategy. Several quality criteria for accepting events as valid muons can be established based on the number of activated wires in the detection layers, discontinuities in the activated wires, and goodness of fit of the measured muon points to a straight line, among others.

The implemented *post-processing function* reads the files with laboratory measurement data and directly saves all the activated wires in all the detection layers for all the events, even if they are not of good quality and cannot be reconstructed in an acceptable way. The aim is to be able to analyse all captured events, reconstruct their signals and thus know and quantify all types of events that are detected. With this information, it is intended to assess whether events discarded due to excessive signals and other problematic wire activation can be reinterpreted and recovered by advanced event reconstruction software. This type of algorithms, which can be applied when measuring with redundant chambers and require interpretation and removal of data at level of wire activation, are studied in section 3.3.4.

Depending on the number of chambers used in the measurement, different methods of removing the background noise have been implemented. For example, when using 4-MWPC detection system, it is checked if the event has contiguous wire hits in all the detection layers with less than a certain number of wires activated in each layer (e.g. 4 wires). The latter parameter could vary depending

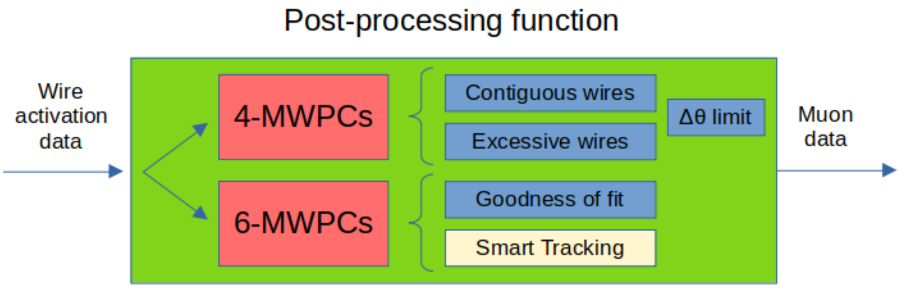

Figure 3.8: *Post-processing function* workflow graph showing the different quality criteria and algorithms applied to get accurate muon reconstruction data with 4 and 6-MWPC detection systems.

on the acceptance angle. Scattering angle cuts, which produce also loss of soft low-momentum muons, but can improve measurement signal-noise ratio are also utilised. On the other hand, when using a detection system with redundant data available, such as a 6-MWPC detection system, which has one extra point to determine the muon trajectories, more precise filtering techniques can be applied. For example, the muon events can be selected depending on their goodness of fit to a straight line.

3.3 System characterisation and commissioning

3.3.1 Wire occupancy

This section describes how several variables have been evaluated in order to ascertain the quality of wire activation data acquired with the detectors in laboratory measurements. Wire activation is continuously monitored in order to check its distribution in the detection layers, and to identify the presence of noise. The wire occupancy correlation with the incident direction of the muons in relation to the wire plane has been studied too.

Wire occupancy distribution in detector layers

Wire activation distributions in each of the detector layers for muons synchronised by the electronic acquisition system are shown in fig. 3.9. In this measurement, no material apart from the air of the atmosphere, the supporting structure, and the detectors themselves has been in between the detectors. In order to ensure a very high quality of the muons considered, a filter on the goodness of fit of the muon reconstruction was performed. It should be mentioned that the chambers, were placed parallel to the ground, and perpendicular to the zenith. The chambers have been located in the vertical axis as specified in the table 3.1. Note that Ch1 and Ch6 have not been active during the measurement. Therefore, layers 1 and 2 correspond to Ch2, 3 and 4 to Ch3, 5 and 6 to Ch4, and 7 and 8 to Ch5.

	Z location of the chambers [cm]					
	Ch1	Ch2	Ch3	Ch4	Ch5	Ch6
4 chambers		101	79	-79	-101	

Table 3.1: Location of the detection chambers during the measurement.

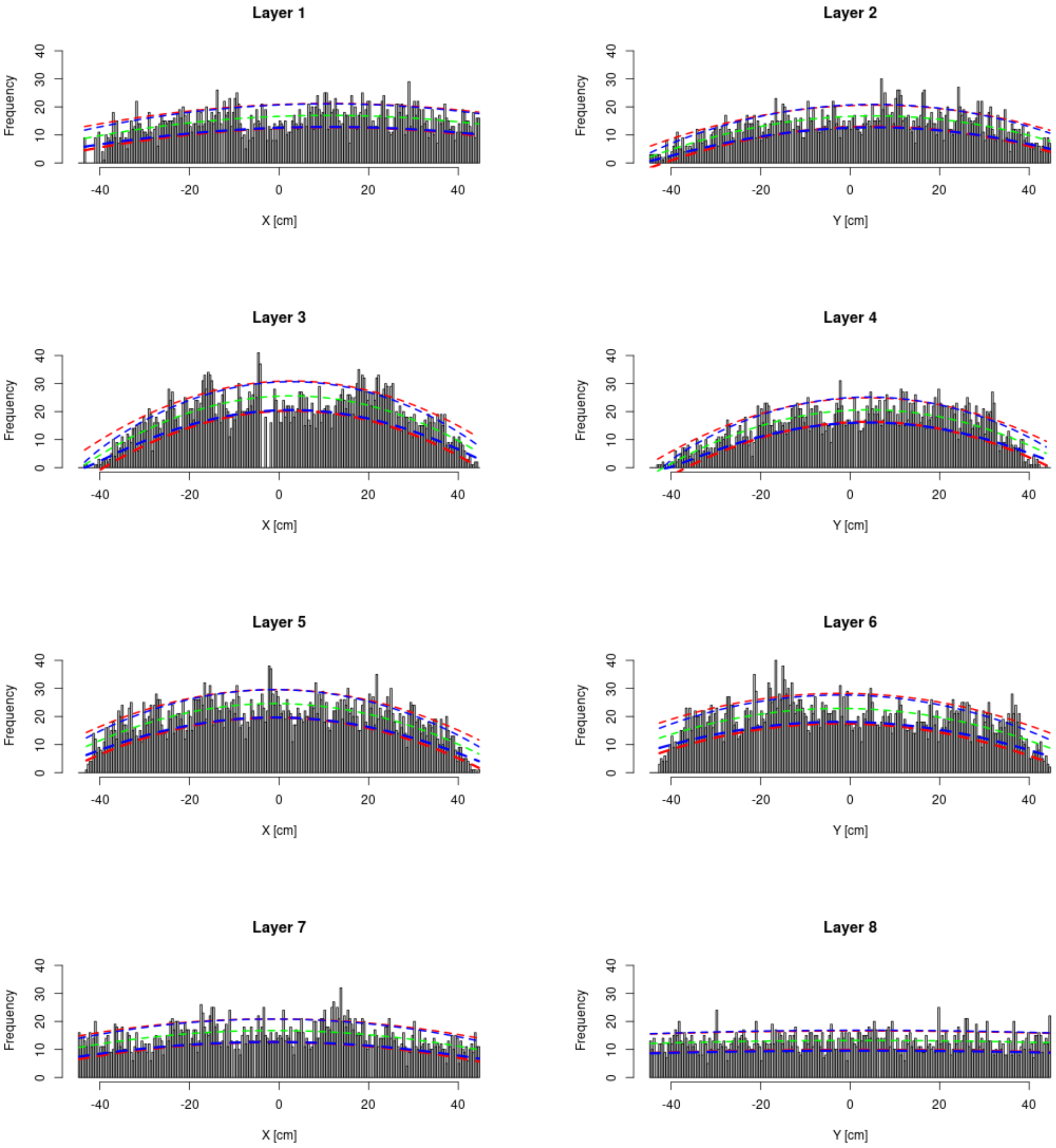

Figure 3.9: Wire activation distributions in each of the detector layers for muons synchronised by the electronic acquisition system, which have been filtered based on the goodness of fit to a straight line. Second order polynomials fitted to wire activation distributions are represented in green, the standard deviation of their residuals in red, and the expected frequency standard error in blue.

Due to the geometric acceptance of synchronised muon flux, central chambers are expected to have more activation density in the area close to their centre comparing to chambers in the ends of the detector. This geometric acceptance influence is clearly observed in the data of the analysed measurement (see fig. 3.9). The behaviour of detection layers has been within the expected parameters during this measurement. Wire activation distributions fluctuate within expectations in almost all cases. However, peaks and clusters of wires with high number of hits are observed indicating more active areas in the chambers. The presence of noisy wires due to poor welding or deterioration, and also the tuning of the gain of readout electronic boards can contribute to an unbalanced activation.

Specifically in this measurement, slight asymmetries can be observed. Layers 1 to 4 are more active in the positive part, while layers 5 and 6 have more activity in the negative. The distributions of layers 7 and 8 are almost symmetric and uniform, especially that of the layer 8. This noticeable but light asymmetries and differences between the wire activation distributions of the chambers can be produced by a not homogeneous gas flow, and as already mentioned, by slight adjustment differences of acquisition electronics, among other factors.

Wire occupancy correlation with direction

The correlation between the number of wires that are simultaneously activated in a single muon event, and its incident angle respect to the wire plane has been characterised. For that purpose, data of one laboratory measurement has been analysed, which totals more than 200000 muon events. These muons have been classified in nine groups depending on their incidence angle projected to a plane perpendicular to the longitudinal direction of the wires ($\theta_{in} = \theta_{X,\ in} = \theta_{Y,\ in}$). Incidence angles up to 45°have been sampled, being the range of each muon group of 5°. The data collected with the the upper layer of the detector (number 1) is shown in fig. 3.10.

The data fulfilled the expectations, showing a clear correlation of the number of wires activated simultaneously for a muon event with its incidence angle in relation to wire plane. For muons with incidence angles smaller than 5°, the 87% of the muons activated one wire, and only around 1% activated four. On the other hand, among the measured muons with largest incidence angles, between 40 and 45 °, simultaneous double-wire activation was the most frequent case with 39% of the muons, above single-wire case, with 36% frequency. Four-wire muons increased up to 4%. These data demonstrated the expected correlation, which is simply due to the geometry of wires and muon incident angles, although its particular characteristics depend also on other structural factors related to the detector, such as wire separation, nature of its the electric field, etc. With this data, a model have been built for the simulation framework utilised in this PhD, allowing a highly realistic production of data that matches the features of the detectors. Information about the simulation framework is detailed in section 2.3.3.

3.3.2 Layer and chamber efficiency study: special trigger setups

In the following subsection, the efficiency of detection layers and chambers which are part of the detection system is quantified. For this purpose, detected and cautiously filtered events are utilised, in order to ensure with as much certainty as possible that they are due to the passage of a muon. The detection efficiency of these events is studied in a single chamber at a time.

In order to determine the layer efficiencies, a set of experiments involving multiple measurements of 10 minutes has been designed. All the measurements were performed the same day. The temperature varied from 25.3 °C to 26.9 °C, and the humidity from 71.7% to 73.3% during the experiments. In those experiments, the parameters mentioned above have been monitored in the target chamber (Ch4), with different *anode voltage*. The power supply of the other chambers (Ch2, Ch3, and Ch5) has been maintained constant, at 2150V, a value that allows a correct operation of the detection system. With the same purpose, the gas flow has been maintained constant, at a level of 0.2 lpm in the input of each MWPC. It has to be mentioned that the gas consumption has not been optimised for these measurements, but this level has allowed a reasonable operation of the detectors.

The measurements have been done with four detection chambers, with three of them operating in

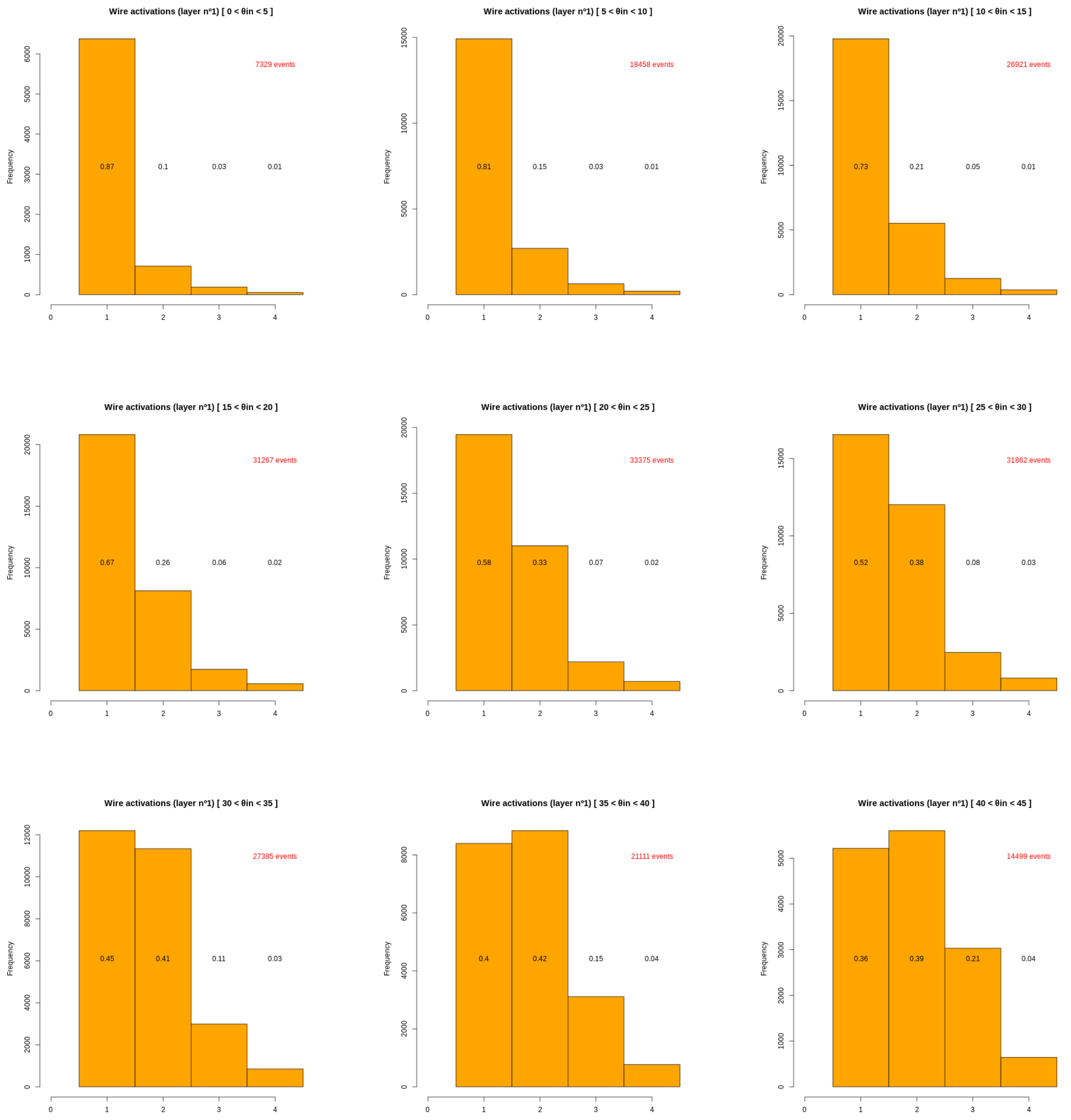

Figure 3.10: Number of simultaneous wires activated in the upper layer of the detector 1 by more than 200000 muon events measured with the laboratory detection setup. The muon events are classified in nine groups depending on their incidence angle in relation to wire plane ($\theta_{in} = \theta_{X,\ in} = \theta_{Y,\ in}$). The planes of the wires were placed horizontally, parallel to the ground, and perpendicular to the zenith.

synchronisation mode (Ch2, Ch3, and Ch5), that is to say, providing to the electronics the trigger signals to collect the data. The other (Ch4), has been working in free mode, reading the activated wires but not participating in the synchronisation process, with the aim to use its independent measurements to check the efficiencies and noise levels. With this setup, what has been obtained is a strict selection of muons with the three synchronising chambers, in such a way that an efficiency test can be performed with the remaining layers.

The criterion to select events as muons with a very high certainty, not only has required wire activation in all the synchronising chambers, but also that those activated wire locations fit to a

	Z location of the chambers [cm]					
	Ch1	Ch2	Ch3	Ch4	Ch5	Ch6
4 chambers		101	79	-79	-101	

Table 3.2: Location of the detection chambers during anode voltage dependent wire and layer efficiency measurements.

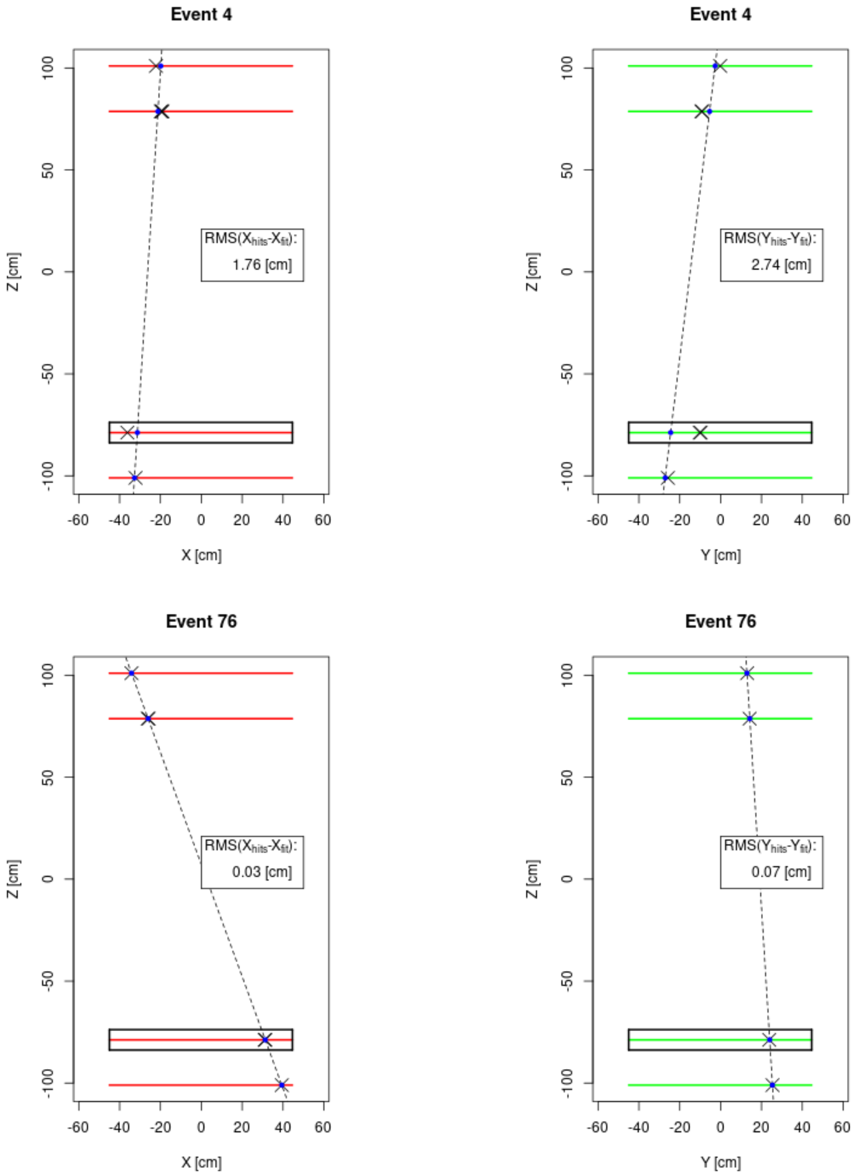

Figure 3.11: Event with wire signals considered not coming from a single muon (event 4), and a "clean" muon event (event 76). The activated wires are indicated with a cross. The muon crossing points (mean of the activated wires) of each layer are signalled with dots. In the plots, the aspect ratios XZ and YZ are maintained as in reality.

line with a root-mean-square error (RMSE) below 0.2 cm. All those conditions have been applied independently to the two layers composing the chambers, therefore resulting in independent analysis of the performance of both coordinates. In the fig. 3.11 two events are plotted, one fulfilling the mentioned conditions in both coordinate layers (X, and Y), and another one failing to fulfil the criterion in both of them. This second event, the 4$^{\text{th}}$ in order of occurrence, is likely to be due to the detection of two muons in the same synchronisation time window, since the recorded trajectories in the detectors do not have noisy or excessive wire activation, but neither do they point to the other detector. The possibility of detecting spurious signals coming from other particles or electronic noise should be also considered. In any case, with the synchronisation and filtering criteria established, the vast majority of this sort of events are identified and discarded.

Efficiency of the chamber Ch4 as a function of anode high voltage

Hereafter, the performance of the target chamber (Ch4) and its two detection layers (X, and Y) is assessed depending on the anode voltage. Once selected the events that with a high probability have only activated wires coming from one muon in the trigger chambers, the behaviour of the chamber Ch4 has been analysed. Different types of efficiencies have been monitored, all of them calculated with respect to the number of events synchronised by the trigger chambers Ch2, Ch3, and Ch5 and that fulfil the criterion to be accepted as muons. The *efficiency A* is defined as the percentage of those events that have activated any wire in the independent chamber Ch4. The *efficiency B* represents the percentage of the events that have at least one activated wire in the chamber Ch4 within an expected area, which is calculated based on the linear fit trajectory determined by the other chambers. An uncertainty corresponding to 5σ of the position resolution is used to determine the limits of the area mentioned above. It should be noted that the position resolution of the system is given by **??**, and is of 1.15 mm for the wire separation of these chambers ($Ws = 4mm$). The *efficiency C*, is defined as the percentage of events whose reconstructed muon crossing point (wire activation mean) in the chamber Ch4 is within the expected area defined above. Note that *efficiency C* conditions are more demanding compared to those of *efficiency B*. In *efficiency C* calculation is also assessed if the signals collected have noisy wires activated that bias the reconstructed muon points, while *efficiency B* only checks if the expected muon hit has been detected, regardless other simultaneous signals in the chamber.

As shown in the fig. 3.12 the *efficiency B* grows until an *anode voltage* of 2200V. It should be mentioned that with a higher voltage the power source starts to significantly increase the current consumption, indicating that an excessive electric field is created, leading to anomalous operation of the chamber. On the other hand, if the evolution of *efficiency C* is observed, which could be understood as an indicator of noise detection, it undergoes a slight decrease with an *anode voltage* of 2200V. Although it is within the uncertainty of the parameter, it could suggest that, with 2200V, the detection of noisy events starts to grow. Due to this fact, and to guarantee that the power supply does not have anomalous current consumption, the value of 2150V is going to be considered the *standard operation anode voltage* for the detection system.

Layer and chamber efficiency for all chambers

In order to quantify the detection efficiencies of all the chambers utilised in the analyses of this thesis, the *efficiency A*, *efficiency B*, and *efficiency C* of each of them has been estimated by means of 15-minute data taking time measurements, which have been performed at the previously defined *standard operation anode voltage* (2150 V). To this end, the chamber under study is removed from the trigger criteria in such a way that muon tracks are reconstructed with other chambers com-

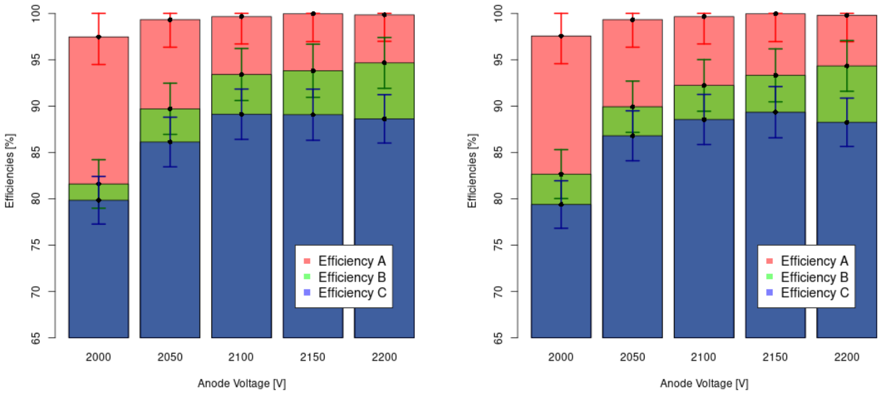

(a) X axis layer. (b) Y axis layer.

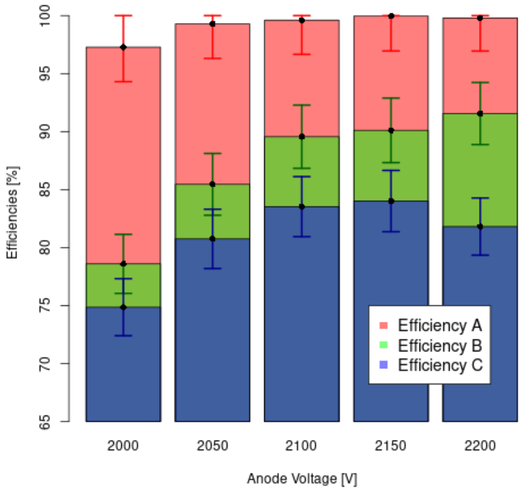

(c) Chamber level.

Figure 3.12: *Efficiency A*, *efficiency B*, and *efficiency C* monitored in the target chamber layers (X, Y), as a function of their *anode voltage*.

posing the system.

Therefore, using the aforementioned trigger setups, the efficiency can be estimated by counting the fraction of times in which the trigger chambers detect a muon track and the chamber under study as well. The target chamber has been placed in all the experiments between the trigger chambers to ensure that all the synchronised muon flux passes through it. Figure 3.13 shows the results of the efficiencies calculated using this procedure.

It is worth mentioning that efficiency estimation of Ch1, and Ch6 have been done with the six chambers connected to the acquisition system, while efficiency estimations for Ch2, Ch3, Ch4, and Ch5 have been performed with only 4 chambers connected. In addition, the trigger configuration for 6-chamber measurements considered signals of 4 chambers, while in the case of the 4-chamber measurements only 3 chambers have been used for the trigger.

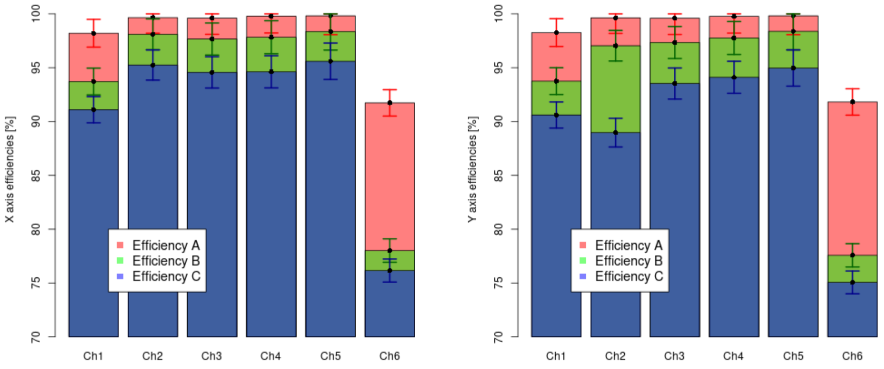

(a) X axis layers.

(b) Y axis layers.

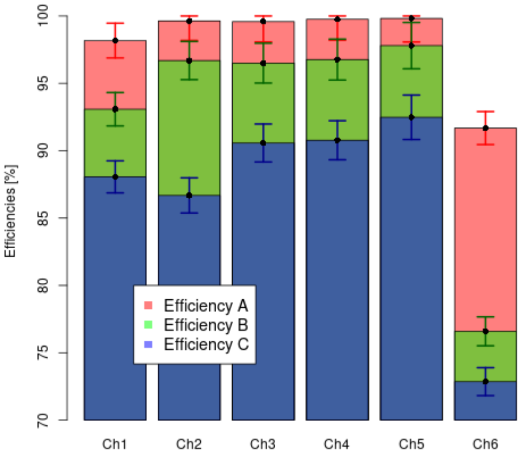

(c) Chamber level.

Figure 3.13: *Efficiencies A*, *B* and *C* of the six MWPCs utilised in this thesis research, at chamber and layer level.

As results show, the chamber six presented a less efficient performance compared to the other chambers. It have been due to malfunction related to the chamber construction, and it is under study in order to understand the origin. The Ch1 also has low efficiencies comparing to the chambers whose efficiency was estimated with 4-chamber measurements that used 3 to trigger the events. Ch2 presents poor performance in terms of noise, as indicated by its *efficiency C*. Its *efficiency A*, *efficiency B* values are at expected levels compared to Ch3, Ch4, and Ch5, while *efficiency C* is significantly lower. Comparing Ch2, Ch3, Ch4, and Ch5 it can be also observed, mainly in Y axis, a slight increase in efficiencies of chambers located in lower positions in Z axis. This minor pattern could be related to the configuration of the connections of the chambers and their layers with relation to the electronic acquisition system.

Discussion and conclusions

The comparison of the measurements performed to estimate chamber Ch4 efficiencies as a function of anode high voltage, and those made to quantify the efficiencies of all the chambers yielded conclusions that are worth mentioning. The efficiencies estimated for Ch4 with the *standard operation anode voltage* of 2150 V are not equivalent. In the case of the voltage dependent efficiency estimations performed with 2150V, the quantified efficiencies A, B, and C are around 85, 90, and 100%. In contrast, in the latter estimations the efficiencies of Ch4 are approximately of 90, 97, and 100%. The differences of *efficiency B*, and *efficiency C* are meaningful with relation to the statistical errors.

The main explanation of the discussed data may lie in the different conditions in which the measurements of both analyses have been made. The detectors were moved by causes unrelated to this project, and therefore the measurements analysed in this thesis have not been taken all in the same building. The voltage dependent estimations have been done in the interior of an industrial building, with only a roof above, while the second set of measurements used to estimate the efficiencies of all the chambers have been made on the ground floor of a multi-storey building. The muon flux attenuation for the former measurements is negligible, in contrast to the latter set of experiments. In addition, the total height occupied by the detectors is also different in the two cases. In the industrial site, the detector height is of roughly of 2 metres (see table 3.2), while in the configurations utilised in the multi-storey building the height is around 1 metre.

With higher detector spacing in the vertical axis, the rate of charged particles (mainly not synchronous muons) that cross the detectors and have to be distinguished by the trigger system increased. At the same time, the flux of muons that are actually synchronous is reduced. Therefore, there is a higher probability of synchronising events with signals not coming only from a single muon. This phenomena explains the lower values of *efficiency B* and *efficiency C* for the measurements taken in the industrial site, where muon arrivals to the chambers are expected at higher rates, while synchronous muon proportion is lower due to detector arrangement. The reason of the worse performance could be the more demanding characteristics of the muon flux arriving to the detectors.

Other important factors affecting the efficiency estimations have been the number of chambers utilised in the measurement, the trigger configuration, and probably the chamber location and trigger connections too. The chambers have been more efficient in 4-MWPC configurations compared to 6-MWPC measurements. Due to the nature of the trigger, which is based in a system of delays and signal management, the location and connections of the chambers could have influenced the results too.

To conclude, the expected full system efficiencies are calculated using the individual chamber efficiency estimations. The average chamber *efficiency B* (among the three efficiencies monitored it is considered the most accurate to determine the actual probability of detecting a muon, regardless it can be reconstructed or not) estimated for Ch2, Ch3, Ch4, and Ch5 in the multi-storey building has been of 96.9%. On the other hand, the quantified *efficiency B* of chamber Ch4 in the industrial site has been of 90.1%. Then, if it is assumed that the efficiency of the entire system is the multiplication of its parts, the expected efficiency for a 4-MWPC detector in the multi-storey building would be of roughly 88%. In the case of using six chambers, and using the unique representative estimation of *efficiency B* made by means of a 6-MWPC measurement (Ch1, 93.1%), the full system efficiency could be around the 65%. Regarding the industrial site, and considering the analysed detector configuration, it could be close to the 66%. Note that these are only rough calculations made with the aforementioned assumptions. In addition, the limitation and conditions of the measurements performed to get the estimations, and their associated statistical errors should be considered. However, this references could be helpful to interpret full system efficiency measurement results that are presented in the next section.

3.3.3 Full system efficiency compared to simulation

The analyses of this section have been performed to study the operation and muon efficiency of the full system when compared to simulations. To this end, all the detected and acquired events have been considered, assessing them in several situations. In all of them, the power supply of the chambers has been set at the *standard operation anode voltage*, 2150V. Acquired events have been monitored with 4 and 6-chamber detection, including variable Z locations of the chambers table 3.3. The synchronisation settings have been varied too, but where it is not specifically mentioned, the trigger is determined by all the chambers of the detection configuration (4, or 6). In those situations, indicators such as simultaneously triggered wires, chamber efficiencies, and rate of detected events have been assessed. The vertical positions where the chambers have been located in the different configurations of the experiments are shown in table 3.3.

	Z location of the chambers [cm]					
	Ch1	Ch2	Ch3	Ch4	Ch5	Ch6
4 chambers - config. 1		45.5	19.5	-19.5	-45.5	
4 chambers - config. 2		101	79	-79	-101	
6 chambers	58.5	45.5	19.5	-19.5	-45.5	-58.5

Table 3.3: Location of the detection chambers in the three different configurations utilised. The reference system origin is in the middle of the detectors.

In order to study the muon detection efficiency, the geometric detector configurations used in laboratory measurements (specified in 3.3) have been simulated using the software of Muon Systems, a particle physics simulator based in Geant4 and Cosmic RaY generator (CRY). With these simulations, a reference of the expected rate of detected has been obtained. This data must be evaluated with caution, since the muon flux generated by the simulator using the CRY particle generator may differ from the real muon flux at the place where the measurements were made.

The first experiment was performed on the ground floor of a multi-storey building. Therefore, an important drop of the detected muon flux is expected due to the absorption of muons produced trough the building. On the other hand, the data acquired with the real-world detector could include events corresponding to noisy signals caused by charged hadrons, electrons, and positrons (*fake muons*), different muons crossing the detectors in the same time acceptance window, or the combination of a muon with spurious signals due to noise in any stage of the electronic system. The flux estimates for these experiments are shown in table 3.4.

The results of 4 and 6-chamber detection show a very noticeable difference in the collected muon

	Detected events [thousands/min]	
	Simulation	Laboratory
4 chambers - config. 1	1.78	1.53
6 chambers	1.30	0.80

Table 3.4: Synchronous muon flux obtained in simulation and in laboratory measurements with the same geometrical configurations. The simulation flux has been generated with CRY. Details about the flux generated in simulation are shown in fig. 3.14.

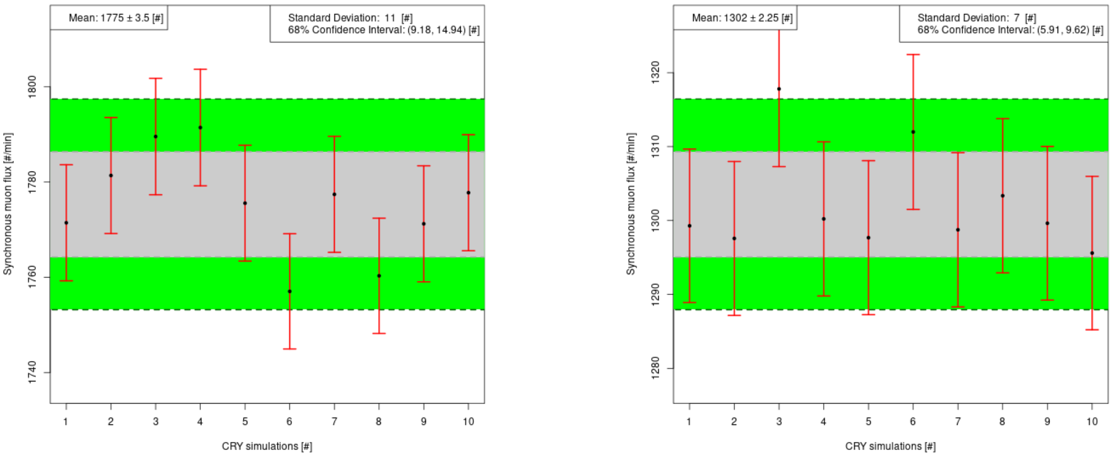

(a) 4 chambers - config. 1.

(b) 6 chambers.

Figure 3.14: Synchronous muon flux obtained in 10 simulations for each of 4 and 6-MWPC configurations.. The simulation flux has been generated with CRY, configured at 0 metres a.s.l, and a latitude of 43.27º. The duration of each simulation data taking time have been of approximately 12 minutes.

flux. The 6-chamber detection suffers an expected efficiency decrease, since the full system efficiency corresponds to the multiplication of the efficiencies of each synchronising chamber.

For this detector configuration and conditions the expected efficiencies of 4-MWPC and 6-MWPC systems are around the 88% and 65%, respectively. These estimations have been calculated according to the chamber efficiency results obtained in the previous section 3.3.2. As the muon absorption produced by the building has not been quantified, is not possible to determine precisely the efficiency of the laboratory detector with respect to simulation data. On the contrary, the efficiency drop between 4-chamber and 6-chamber detection can be compared. In previous estimations the drop was from 88% to 65% (74%), while in the latter measurements the flux drop has been of a 52%. This indicates a worse detection efficiency, probably due to the malfunction of chamber Ch6, which could not be corrected.

Other fact observed related to triggered events is that, when synchronising and measuring with the 6 chamber configuration, more events with void data are acquired compared to “4 chambers - config. 1”. These type of events activate the trigger, but do not have any signal determining the activated wires in some of the detection layers. They could be events that activate the synchronisation due to a malfunction, and therefore they have no wire signal to read in some of the layers. Or the opposite, they might be well triggered, but they undergone a readout failure. These events are quantified for two measurements of 15 minutes of data taking in the table 3.5. Their increase in the case of the 6-chamber system may be due to the greater complexity of its event triggering configuration. In 4 chamber measurements 8 groups of wire signals are synchronised (two coordinates per chamber), while with 6 chambers 12 signal groups have to be considered. It is also worth mentioning that in the 6-chamber configuration the detectors cover a larger range in Z axis, and therefore a higher rate of not synchronous muons and other charged particles pass through the detection layers, making the triggering task more demanding. The probability of detecting spurious electronic noise is increased too, with the number of chambers utilised.

	Void data events [%]
4 chambers - config. 1	1.87
6 chambers	7.05

Table 3.5: Proportion of events with void data in any of the detection layers.

A third series of measurements has been carried out, in which synchronisation settings utilising different numbers of chambers have been tested, but always maintaining the geometrical configuration of the synchronising chambers, i.e. keeping the location of the upper and lower synchronising chambers so as not to vary the expected muon flux due to the geometry of the system. The results show the variation of detected event rate depending on the number of chambers used for synchronisation (see table 3.6). This results match the expectations, since the efficiency of the full system is the product of the efficiencies of all their parts.

Number of synchronising chambers	Detected events [thousands/min]
6	0.74
4	1.40
2	1.60

Table 3.6: Events detected in relation to the number of chambers used in synchronisation.

The increase of events is considerable when synchronising with fewer chambers. However, one must consider the possibility that more noise may has been captured due to the less restrictive synchronisation utilised. This issue can be handled applying event filtering techniques, such as the ones proposed in section 3.2.2, and also with more advanced Smart Tracking algorithms (section 3.3.4), rather than trying to filter the noise completely with the trigger system, that can cause loss of valid muon events. On the other hand, noisy events captured by the trigger can always be later discarded with the above mentioned post-processing strategies.

In a last analysis of the full system performance, all the triggered events have been analysed in 7 additional measurements of several hours. Flux and wire activation data has been interpreted in order to explain the influence of different phenomena that can produce signals in the wires. The results extracted from the experiments are shown in table 3.7.

	Events [k/min]	Void data [%]	N.C. [%]	N.C. one layer [%]
Measurement 1	0.96	9.78	55.01	24.92
Measurement 2	0.90	9.17	46.55	20.14
Measurement 3	0.90	9.80	55.74	25.23
Measurement 4	0.94	9.46	49.07	21.72
Measurement 5	0.90	9.49	55.73	25.26
Measurement 6	0.88	9.19	46.73	20.30
Measurement 7	0.89	9.21	47.05	20.45

Table 3.7: Rate of events acquired in measurements performed with the second configuration of 4-chamber detection ("4 chambers - config. 2"). Events with void data in any of the detection layers are specified together with the proportion of events with non-contiguous wires activated (N.C.), and with non-contiguous wires activated only in one of the layers of the detector (N.C. one layer).

The detector configuration used in these measurements ("4 chambers - config. 2") has been also simulated to obtain a reference of the muon flux that could be expected. The data obtained from the simulation software is a flux of 0.62 thousand muons per minute. It is remarkable the excess of event flux collected with the laboratory detector, which could be due to the synchronisation of different but practically simultaneous muons, and also to other charged particles or noisy wire activation. Note that these measurements have not been performed in the same place as the previous experiments studied in this section. In this case, the detectors have been in the interior of the already mentioned industrial building, with only a roof above them. The muon flux absorption for these latter measurements is negligible, in contrast to the other case.

Therefore, compared to the previous measurements performed in the multi-storey building, a higher rate of muon arrival is expected, while the flux of muons that are actually synchronous is reduced due to the larger separation of the chambers in Z axis. Both facts make the task of the trigger system more complicated, as the the ratio of synchronous muons to muons which are not synchronous and other phenomena that can activate the detection wires is reduced. The proportion of void data events, which is almost stable in all the measurements, supports the conclusions explained above.

Another important aspect that emerges from the data collected in this analysis is the existence of a quantity of events that can be retrieved by means of intelligent trajectory reconstruction algorithms which manage the signals at wire activation level (Smart Tracking algorithms). The simulation shows a flux of 0.62 thousand muons per minute. However, in real measurements, the resulting flux of events that can be properly reconstructed is approximately of 0.36 thousand muons per minute (subtracting, from the average event flux obtained, around the 10% which are void data events, and the 50% which are events with non-contiguous wires). In other words, it is likely that around 0.26 thousand muons per minute are being lost. In addition, it should be taken into account the possible presence of non-muon events among those acquired by the laboratory detector. In the section 3.3.4, the above mentioned Smart Tracking algorithms are described and used to recover as many unreconstructed muons as possible, based on these analyses. Data on the number of events with non-contiguous wires in a single detection layer, which is more than 20% of the detected event flux, indicate that at least that many events are susceptible to be reconstructed by Smart Tracking algorithms, simply removing the unwanted signals from a single layer.

3.3.4 Reconstruction efficiency improvement and noise reduction

Smart tracking techniques have been applied in order to identify muon signals in events with noisy wire activation or void data in any of the detection layers. These algorithms can improve the full system reconstruction efficiency, reinterpreting complex but resolvable signals acquired by the detection layers. In this section, those techniques are applied to the same dataset used previously and collected with 6 chambers (see table 3.3). The redundant detection data provided by this system is used to interpret event signals and reconstruct those belonging to a muon.

Events with void data

A total of 847 events acquired with void data have been analysed. In fig. 3.15 a representative event, which fulfils the standard quality requirements for the 4-chamber systems is plotted as an example.

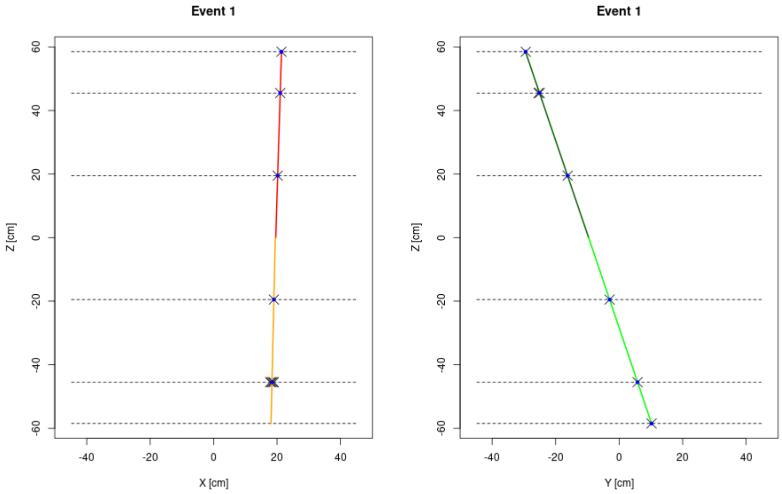

Figure 3.15: Event with void data in the lowest layer of X axis (layer without signal). The activated wires are indicated with a cross. The muon crossing points (mean of the activated wires) of each layer are signalled with blue dots. In the plots, the aspect ratios XZ and YZ are maintained as in reality.

Among the void wire data events, the 34% can be directly reconstructed in both axes by means of the signals captured with the 6-chamber detection system. Despite the fact that these events have one or more layers without wire activation, they have at least acquired signals in 2 of the 3 chambers in each trajectory detector (both for X and Y axis), and fulfil the standard quality requirements for the 4-MWPC system. Those requirements involve contiguous wire activation in all the detection layers without exceeding the amount of 4 wires per layer.

In order to show that these recovered events are valid, their projected angular deviation are shown in fig. A.1. The distribution looks healthy, in agreement with the expectation of actual muon events.

Not contiguous wires

The 41% of the total of the events (4915 out of 12021), which have been initially discarded due to not adjacent wire activation have been also analysed. Among them, 2958 (25% of the total) have signals without not contiguous wires in at least two of the three detection layers used to calculate each projected trajectory (upper X, upper Y, lower X, and lower Y).

To retrieve this type of events, contiguous wire clusters have been identified. Employing their locations, the possible combinations to reconstruct muon trajectories have been assessed in an automated way. For each of the clusters the event trajectory and its goodness of fit to a straight line have been calculated. Among all the possibilities, the cluster with the best goodness of fit has been selected, while other wire activation clusters have been removed.

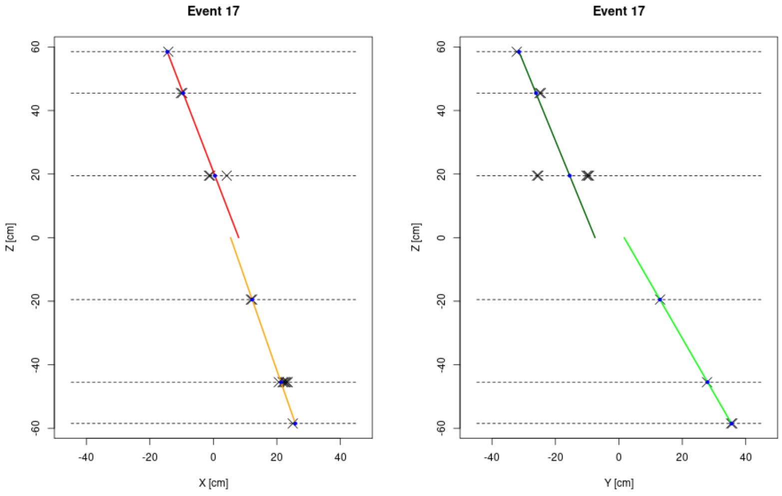

(a) Initial. (b) Initial.

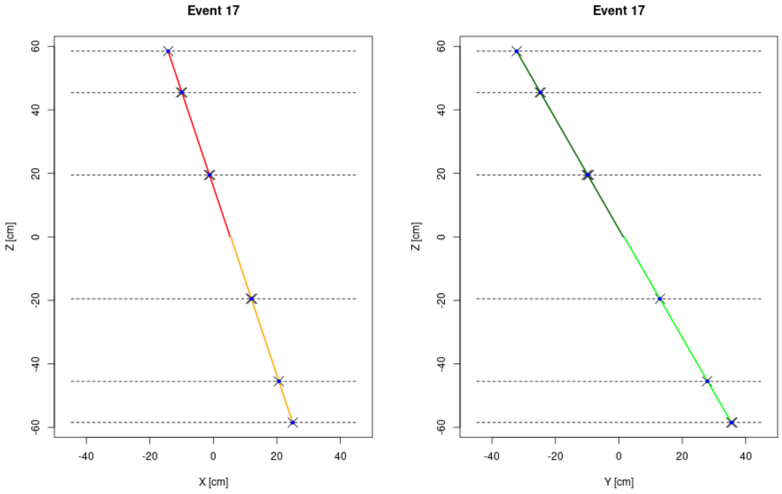

(c) Not contiguous wire removal. (d) Not contiguous wire removal.

Figure 3.16: Event with noisy non adjacent wire activation in two layers of X axis and in one layer of Y axis. Its reconstruction is improved by removing wire activation that fit worse to straight lines in each detector and axis.

After this treatment, 2136 out of the 2958 events do not have excessive wire activation, meaning that in none of the layers, more than 4 wires have been activated simultaneously. Those events already fulfil standard quality requirements to be reconstructed. An example is displayed in fig. 3.16, while their measured deviation distributions are shown in fig. A.2. These distributions, which have similar spreads comparing to those of recovered void data events, are also an indicator of quality and absence of noise.

On the other hand, the rest (822 events) could be re-processed to analyse whether their excessive wire activation is removable.

Excessive wire activation

Initially, 12% of the total of the events (1454 out of 12021) did not fulfil reconstruction requirements only due to what has been considered excessive wire activation, meaning that these events do not have neither layers with void data nor not contiguous wires. The Smart Tracking reconstruction procedure that has been followed consist on simply removing the most excessive wire activation of each of the built trajectories, i.e., that with higher amount of activated wires.

In fig. 3.17 an event with a single excessive wire activation cluster in the lower trajectory of Y axis is shown. The cluster is displaced towards the negative side in relation to the initially fitted trajectory. Removing it, the trajectory is slightly modified. It is worth mentioning that more noisy activation clusters have been observed and removed with this technique. The overall deviation distribution of the retrieved events is shown in fig. A.3. As in the previous types of retrieved muon events, the spreads of the deviations are in the expected levels. Although the most significant excessive wire activation of each trajectory have been removed, the 5% of the events still have some over-activation.

Poor goodness of fit to straight line

The aforementioned excessive activation wire events that have not been completely removed, and also the rest of the events that already fulfil 4-MWPC system reconstruction requirements can be assessed again in order to eliminate or reinterpret them. To do this, the goodness of fit to straight lines of the trajectories of the events has been checked.

In the following analysis, 44% of the events (5295) that without any Smart Tracking processing already fulfilled the 4-MWPC reconstruction requirements, are considered. Events with trajectories reconstructed using three points that do not fit well to a straight line (as the trajectory of the upper detector of the Y axis of the represented in fig. 3.18) have been identified. Specifically, a not very demanding fit RMSE threshold of 0.5 cm has been defined. All the events above it have been selected, and in this case, removed to prevent the reconstruction of noisy events. X axis and Y axis have been analysed independently, eliminating 839 and 897 respectively. The number of removed events if both axes are considered is 996. The measured deviations for the whole group of events are represented in fig. A.4, before and after the noise removal.

The distributions of both axes before and after the noise removal have smaller standard deviations, although the shape of the distributions is practically the same. Probably most part of the noisy events removed have higher projected deviations than 50 mrad, but even in this limited range, the effect of the noise removal is noticeable.

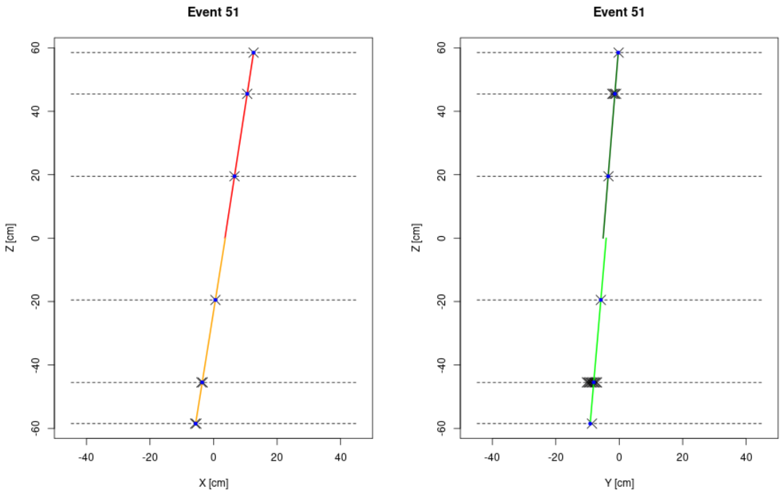

(a) Initial.

(b) Initial.

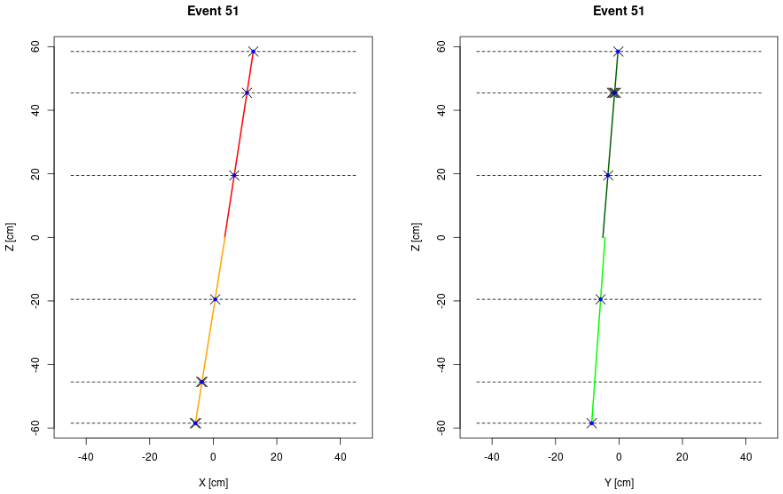

(c) Excessive wire removal.

(d) Excessive wire removal.

Figure 3.17: Event with noisy and excessive wire activation in the intermediate layer of the lower trajectory detector of Y axis. Its reconstruction is improved by removing wire activation that fit worse to straight lines in each detector and axis.

Conclusions

To conclude, the different Smart Tracking techniques and the proportion of events treated by them in this analysis example are summarised. The total acquired events during the studied measurement have been 12021.

Firstly, 847 events with layers with void data have been analysed (7%). Among them, the %34 have been directly retrieved. Therefore, 2.4% of all the acquired events have been recovered for reconstruction. Secondly, 4915 events with not contiguous activated wires have been processed, retrieving 2958 (around %25 of the total acquired). Thirdly, 1454 (12%) events with excessive simultaneous wire activation have been studied. All of them have been retrieved after removing the most significant excessive wire activation clusters. Finally, events whose trajectories fit poorly to straight lines have been removed. Among 5295 events that already fulfilled the 4-MWPC system reconstruction requirements, 996 have been eliminated due to their poor fit trajectories.

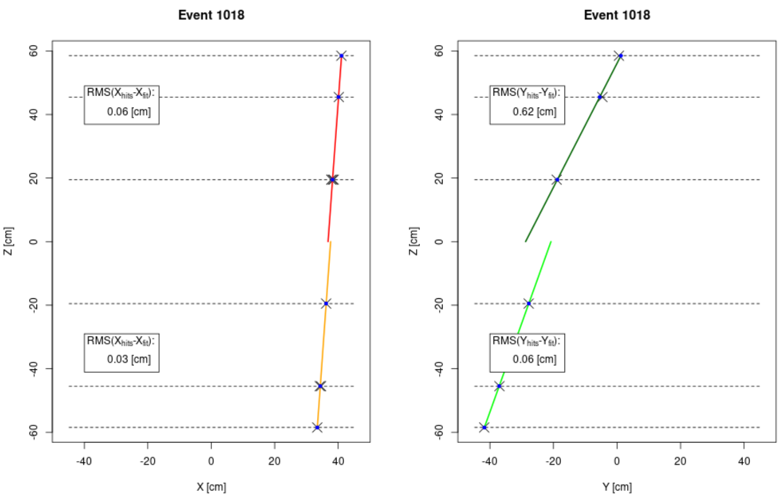

Figure 3.18: Event which fulfils the standard quality requirements for the 4-chamber system, but has a suspicious signal in the lowest layer of the upper detector of Y axis. This trajectory fits to a straight line with RMSE above the specified threshold of 0.5 cm.

Therefore, in total almost 40% of the synchronised events have been assessed, retrieved, and correctly reconstructed by means of the described Smart Tracking techniques. In addition, noise removal based on trajectory goodness of fit has been performed, eliminating around 1000 events (8%). It is worth mentioning that secondary processing could be done to events that have been already treated as described, but still have redundant signals to build trajectories, i.e., more than 2 muon points per track. In any case, the most important group of muons have been analysed above.

3.3.5 Intrinsic resolution of the system

Theoretical expectation

In this subsection, the spatial resolution of muon hits (X, Y), the directions (θ and their projections θ_X and θ_Y), and the angular deviations ($\Delta\theta$, $\Delta\theta_X$ and $\Delta\theta_Y$) are analysed.

In order to assess the spatial resolution of an individual layer, muons are assumed to arrive vertically ($\theta = \theta_X = \theta_Y = 0$), and uniformly distributed. These assumptions are not completely true, since muons can come with some inclination, however it is reasonable to consider them in order to get a theoretical estimation of the intrinsic resolution of the layers. Hence, the probability density function of muon hits in the detection span of a single wire, $P_{hits,\ plane}$, is defined as:

$$P_{hits,\ plane} = P(X) = P(Y) = \begin{cases} 1/W_s & for\ x\ \in [-W_s/2, +W_s/2] \\ 0 & otherwise \end{cases} \tag{3.1}$$

Where W_s is the wire separation, and X and Y the location of the hits in the axes perpendicular to the wires and coincident with their detection planes. The resolution of the reconstructed muon hit locations is defined by the separation of the wires, and since it is assumed that they follow a uniform distribution, their standard deviations $\sigma(X)$, and $\sigma(Y)$ are:

$$\sigma_{hits,\ plane} = \sigma(X) = \sigma(Y) = \frac{W_s}{\sqrt{12}} \tag{3.2}$$

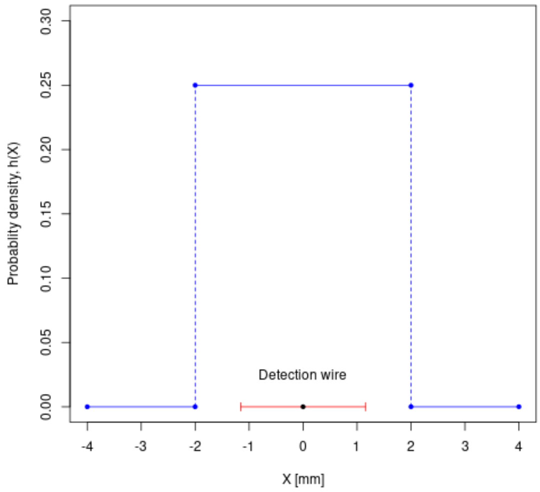

Figure 3.19: The probability density function of muon hits in the detection span of a single wire of the MWPC detector ($W_s = 4$ $[mm]$) assuming that they are uniformly distributed (blue). Detection wire location in X axis (black dot), and standard deviation of the hits in relation to the wire position (red).

Once the spatial resolution of the layers is known, the expected resolution of the muon directions can be obtained. This calculation will be based on detectors with only two layers in each projection. In this situation, assuming that the measurements in upper layer 1, and lower layer 2, are denoted by X_1, Y_1 and X_2, Y_2, muon direction angles can be defined as $\theta_x = \arctan{(X_2 - X_1)/L_s}$ and $\theta_y = \arctan{(Y_2 - Y_1)/L_s}$, where L_s is the separation between the two layers. Under these circumstances the angular resolutions are given by:

$$\sigma(\theta_X) = \frac{\sqrt{2}L_s}{L_s^2 + (X_2 - X_1)^2}\,\sigma(X) \tag{3.3}$$

$$\sigma(\theta_Y) = \frac{\sqrt{2}L_s}{L_s^2 + (Y_2 - Y_1)^2}\,\sigma(Y) \tag{3.4}$$

Assuming now, that the angular resolution of both the upstream and downstream detectors is the same, the uncertainty in the angular difference between the two trajectories measured by them is simply:

$$\sigma(\Delta\theta_X) = \frac{2L_s}{L_s^2 + (X_2 - X_1)^2}\,\sigma(X) \tag{3.5}$$

$$\sigma(\Delta\theta_Y) = \frac{2L_s}{L_s^2 + (Y_2 - Y_1)^2}\,\sigma(Y) \tag{3.6}$$

To finish the study on the theoretical intrinsic resolution of the detectors, the *minimum measurable projected deviation* is defined and calculated. This quantity is the the minimum projected deviation higher than zero, that can be measured with this detection system, assuming single wire activation. It corresponds to the angle obtained when a muon activates two consecutive wires in layers 1 and 2. The corresponding expression is:

$$\Delta\theta_{\theta=0,min} = \arctan(\frac{W_s}{L_s}) \tag{3.7}$$

In a typical configuration of the MWPC detectors, wire and layer separation could be of $W_s = 4\ mm$ and $L_s = 200\ mm$, in such a way that $\Delta\theta_{\theta=0,min} =\ 20\ mrad$. In this case, the expected standard deviation for muon position determination in a single detection coordinate ($\sigma_{hits,plane}$) is approximately 1.15 mm (see equation 3.2 and figure 3.19), while the standard deviations of the projections of detected trajectories $\sigma(\theta_X)$ and $\sigma(\theta_Y)$, assuming vertical incidence, is around 8.2 $mrad$. These and the rest of the uncertainties defining the intrinsic resolution of the system, for this specific example, are summarised in table 3.8.

	W_s = 4 mm, L_s = 200 mm
$\sigma_{hits,\ plane}$	1.15 mm
$\sigma(\theta_{X/Y})$	8.16 mrad
$\sigma(\Delta\theta_{X/Y})$	11.55 mrad
$\Delta\theta_{\theta=0,min}$	20.00 mrad

Table 3.8: The intrinsic resolution of the system configured with a wire separation of $W_s = 4\ mm$, and a layer separation of $L_s = 200\ mm$.

Effects of wire granularity on measured deviations

The fact that there is a finite number of wires in every layer implies that the position measurements are intrinsically discrete. Since angular variables are obtained from the positions, the angles are also discrete.

In order to understand the effect, only muons coming vertically are considered, since there is a dependency of the minimum measurable angles on the incident angle of the muon. Events with multiple-wire activation are also taken into account. Under these conditions, the possible angular measurements for a two layer detector can be expressed as:

$$\Delta\theta_{Meas} = \theta_{out} - \theta_{in}\ =\ \arctan(\frac{w_{in}\ W_s}{L_s}) - \arctan(\frac{w_{out}\ W_s}{L_s}) \tag{3.8}$$

where W_s is the wire separation, L_s is the distance between layers, and w_{in} and w_{out} are the distance in number of wires from the wire activated in the upper layer to that activated in the lower layer, for each of the trajectory detectors (in, out). Note that, in this expression, the trajectory angles are specified depending on the detector construction parameter W_s, as well as on w_{in} and w_{out}.

Since in this analysis events with multiple-wire activation are considered, the distances w_{in}, and w_{out} can actually be semi-integer to take into account hit reconstructions in the intermediate locations between wires. Regarding muon deviation distributions, the most probable case is $w_{in} = w_{out}$, followed by other combinations. The next most likely corresponds to the half of the spacing of wires, which can be measured in the case of simultaneous multiple-wire activation ($|w_{out} - w_{in}| = 1/2$). Thirdly, one wire spacing deviations are expected ($|w_{out} - w_{in}| = 1$). After, one and a half wire spacing intermediate deviations again ($|w_{out} - w_{in}| = 1 + 1/2$), subsequently two wire spacing deviations ($|w_{out} - w_{in}| = 2$), etc.

The described effect can be observed in the projected deviation distributions of fig. 3.20. $\Delta\theta_{Meas}$ angles for $w_{in} = 0$, and $w_{out} = 0, 1/2, 1, 1 + 1/2, 2, 2 + 1/2$ are marked with blue arrows, and they match with deviation distribution peaks measured with a simulation detector. The detector has been configured with $W_s = 4\ mm$, and $L_s = 233\ mm$.

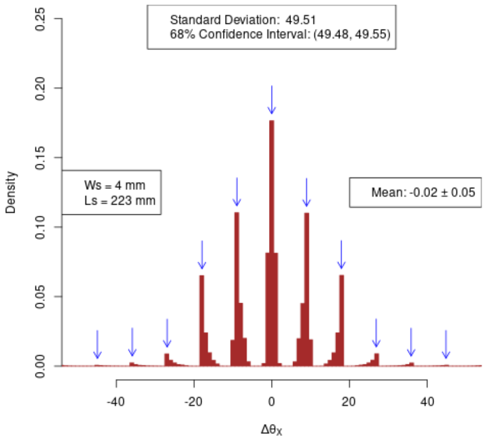

Figure 3.20: Projected deviation distribution for a simulated detector with $W_s = 4\ mm$, and $L_s = 233\ mm$. $\Delta\theta_{Meas}$ angles for $w_{in} = 0$, and $w_{out} = 0,\ 1/2,\ 1,\ 1 + 1/2,\ 2,\ 2 + 1/2$ are marked with blue arrows.

Resolution as a function of the number of detectors

In order to estimate the intrinsic resolution of the detector system, and compare it for 4, and 6-chamber configurations, a simulation study has been performed. Note that in these simulations, the upper and lower detectors have been fixed to exactly the same height in Z, so that their angular resolution is only affected by the change of the number of chambers utilised (see table 3.9). It should be mentioned that in all the cases considered in this simulation study, only muons which cross all the chambers of the detection system have been analysed.

Before estimating the resolution of the deviations for the full detector, the estimation of the X and Y in each of the detectors, upper and lower, is provided. These coordinates are obtained from the projection of the muon trajectories in each detector to the horizontal plane marking the middle of the detector. For this reason they are refer to as the detector midpoints. The resolution provided

	Z location of the chambers [cm]					
	Ch1	Ch2	Ch3	Ch4	Ch5	Ch6
4 chambers		45.5	19.5	-19.5	-45.5	
6 chambers	45.5	32.5	19.5	-19.5	-32.5	-45.5

Table 3.9: Location of the detector chambers in the two simulations (4 and 6-chamber detection).

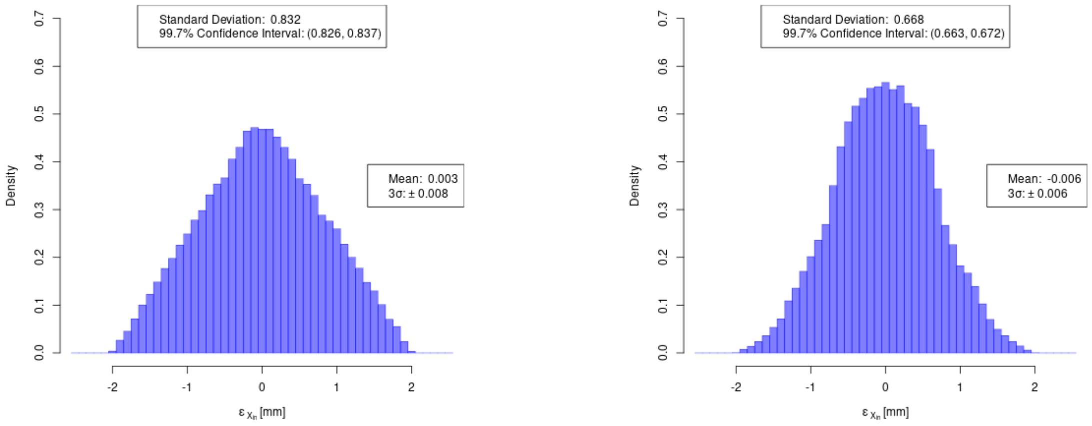

(a) 4 chambers.

(b) 6 chambers.

Figure 3.21: Error of reconstructed detector midpoint X coordinates measured with simulated 4, and 6-chamber detector configurations. The errors are the difference of the reconstructions performed using realistic resolution ($W_s = 4\ mm$), and unreal perfect resolution ($W_s = 0\ mm$) MWPCs.

by the 6-chamber system improves that of the 4 chamber measurement, as shown in fig. 3.24. As can be seen, the distribution of the estimated midpoints errors, that is, the difference between the midpoint coordinate reconstructed using a realistic resolution ($W_s = 4\ mm$) and the true position assuming perfect resolution ($W_s = 0\ mm$) MWPCs are detailed. The spread of the errors for 6-chamber configuration is smaller comparing to the 4-chamber system, and the difference is much greater that their 3σ confidence intervals.

Therefore, it can be concluded that the midpoint resolution is improved with the addition of two chambers to the detector. Note that only one coordinate is analysed, since in ideal chamber alignment conditions they should be statistically equivalent. The errors obtained in this last analysis are consistent with the theoretical intrinsic resolution expectation, which has been studied in the previous section 3.3.5 for the case of 4-MWPC detectors. As the detector midpoint coordinate is determined using 2 (4-chamber system) and 3 layer data (6-chamber system), their expected error can be estimated as follows:

$$\sigma_{Xin,\ N\ chambers} = \sigma_{Yin,\ Nchambers} = \frac{\sqrt{\sum_{i=1}^{N/2} \sigma^2_{hits,\ plane\ i}}}{N/2} \tag{3.9}$$

$$\sigma_{Xin,\ 4\ chambers} = \sigma_{Yin,\ 4chambers} = \frac{\sqrt{\sigma^2_{hits,\ plane} + \sigma^2_{hits,\ plane}}}{2} = 0.81\ [mm] \tag{3.10}$$

$$\sigma_{Xin,\ 6\ chambers} = \sigma_{Yin,\ 6chambers} = \frac{\sqrt{\sigma^2_{hits,\ plane} + \sigma^2_{hits,\ plane} + \sigma^2_{hits,\ plane}}}{3} = 0.67\ [mm] \tag{3.11}$$

Where $N/2$ is the number of detection layer used to measure Xin or Yin. The hit uncertainty $\sigma_{hits,\ plane}$ is of around 1.5 mm for $W_s = 4\ mm$, as specified in **??**.

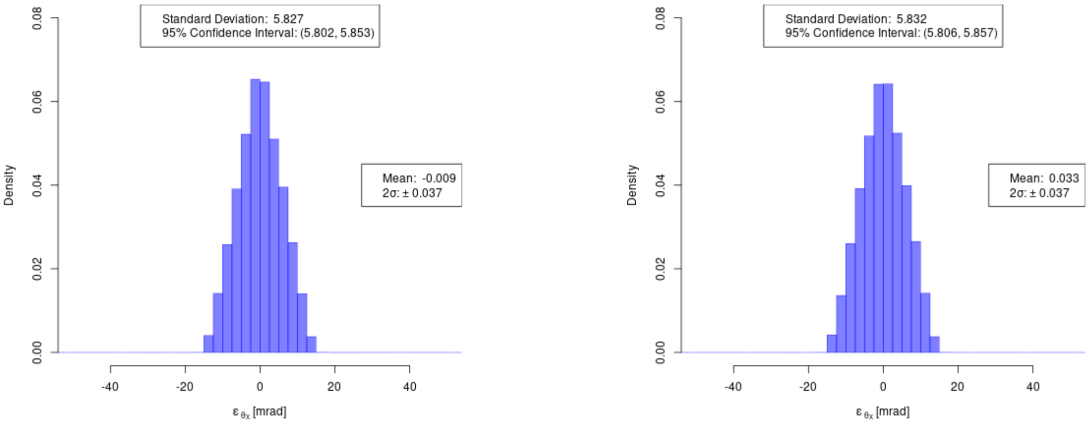

(a) 4 chambers.

(b) 6 chambers.

Figure 3.22: Errors of projected muon trajectories measured with simulated 4, and 6-chamber detector configurations. The error is calculated based on the difference between reconstructions performed using realistic resolution ($W_s = 4\ mm$), and unreal perfect resolution ($W_s = 0\ mm$) MWPCs.

In the fig. 3.24 the errors of projected muon trajectory angles measured with simulated 4, and 6-chamber detector configurations are shown. The error calculation is obtained subtracting the trajectories reconstructed with a perfect resolution ($W_s = 0\ mm$) to those obtained with realistic resolution ($W_s = 4\ mm$) MWPCs. The spread of errors for the two configurations are within their confidence intervals, meaning that they reproduce the same tracking resolution.

The resolution of the incident muon trajectory angles measured with the upper trajectory detector θ_{in} is statistically equivalent for systems using 4 and 6 chambers.

Compared to the theoretical intrinsic resolution expectations discussed in section 3.3.5, the trajectory angle determination errors obtained in this simulations are slightly smaller. The expected angular resolution for a trajectory projected to a plane, i.e., θ_X and θ_Y, is 6.28 mrad (see equation 3.3) for this setup with $W_s = 4\ mm$ and $L_s = 45.5 - 19.5 = 26\ cm$ (see table 3.10). Differences between theoretical calculation assumptions and simulation approach are probably responsible of this small change in the resolutions.

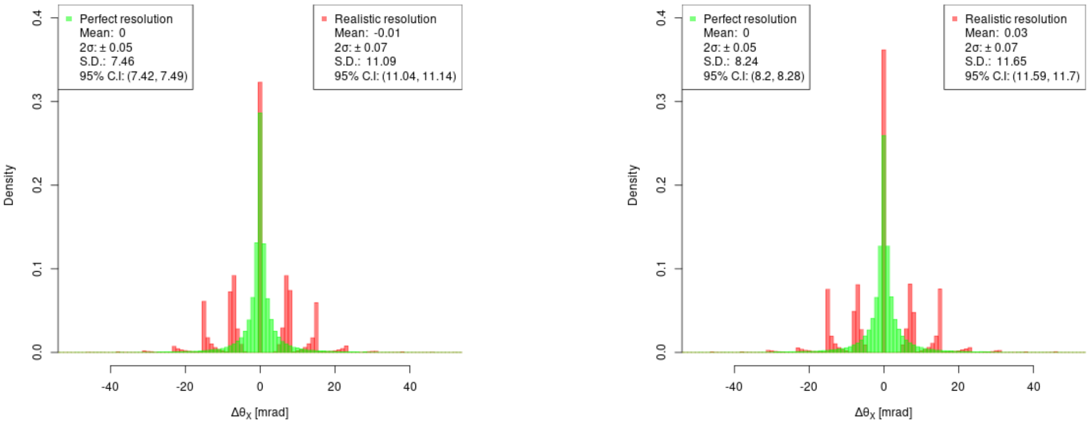

(a) 4 chambers. (b) 6 chambers.

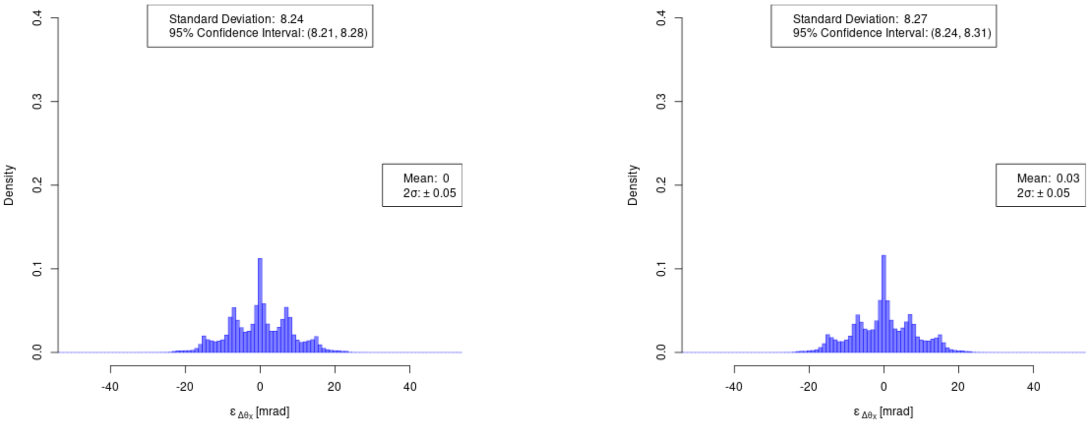

(c) 4 chambers. (d) 6 chambers.

Figure 3.23: Projected muon deviations ($\Delta\theta$) measured with simulated 4, and 6-chamber detector configurations using realistic resolution ($W_s = 4\ mm$), and unreal perfect resolution ($W_s = 0\ mm$) MWPCs. Their errors ($\epsilon_{\Delta\theta}$) are also represented, which have been calculated as the difference between realistic and perfect resolution deviations.

In the fig. 3.23 projected muon deviations $\Delta\theta$ measured with simulated 4, and 6-chamber detector configurations using realistic resolution ($W_s = 4\ mm$), and perfect resolution ($W_s = 0\ mm$) MWPCs are shown. Their errors are also represented, which have been calculated subtracting the deviations reconstructed with perfect resolution ($W_s = 0\ mm$) to those obtained with realistic resolution ($W_s = 4\ mm$) MWPCs. Note that the statistics of the distributions have been calculated for muons fulfilling the condition $|\Delta\theta| < 100\ mrad$.

As in the case of upper detector trajectories (θ_{in}), the spread of projected muon deviation errors for the two configurations are within their confidence intervals, meaning that their deviation resolution is equivalent. As an interesting fact, it should be mentioned that the spread of deviations reconstructed with perfect resolution is statistically smaller for the case of 4-chambers. This could be due to an slight increase of muon scattering produced by the material of the two additional chambers used in the 6-chamber simulation.

Compared to the theoretical intrinsic resolution expectation, the deviation errors obtained in this simulations are slightly smaller. The expected angular resolution for deviations projected to a plane, i.e., $\Delta\theta_X$ and $\Delta\theta_Y$, is 8.88 mrad (see equation 3.5) for this setup with $W_s = 4\ mm$ and $L_s = 26\ cm$. Differences between theoretical calculation assumptions and simulation approach are probably responsible of this small change in the resolutions.

Laboratory measurements: muon deviations ($\Delta\theta$)

The laboratory measurements were carried out with the configuration utilised in previous studies, detailed again in table 3.10. It is worth mentioning that the analysed correspond to events that have triggered simultaneous signals in all the chambers.

	Z location of the chambers [cm]					
	Ch1	Ch2	Ch3	Ch4	Ch5	Ch6
4 chambers		45.5	19.5	-19.5	-45.5	
6 chambers	58.5	45.5	19.5	-19.5	-45.5	-58.5

Table 3.10: Location of the detector chambers in the two laboratory measurements (4 and 6-chamber detection).

The muon deviations measured with 4 and 6-chamber detection systems have been compared. The muon deviations measured with the 4-chamber detection system show slightly lower standard deviations. It should be mentioned that the standard deviations have been calculated for absolute value deviations below 100 mrad, which is a broad enough range to represent almost the whole distribution of muons, but removing possible outliers produced by misleading wire activation, such as hits of other charged particles that are not muons. The previous simulation analyses show that muon deviations slightly increase in 6-chamber measurements, probably due to the material of the two additional chambers. The laboratory experiments seem to confirm that fact, as they also show slightly higher deviations in the case of 6 chambers. Note that the deviations reconstructed with the 4-chamber system are not affected by the scattering in the material of the exterior chambers Ch1, and Ch6 (see table 3.10).

Compared to the theoretical intrinsic resolution expectations discussed in section 3.3.5, the measured standard deviations of muon scattering angles are clearly higher. For the 4-chamber detection system configuration utilised in the measurement analysed in this section ($W_s = 0.4cm$, $L_s = 26cm$), the expected deviation measurement intrinsic resolution is of 8.9 mrad, while the actual resolution is around 14.8 mrad. This difference could be caused by the assumptions made in the theoretical calculations (no consideration of simultaneous multiple-wire activation, only vertically incident muons in relation to wire planes, and uniform distribution of hits), and to a lesser degree by misalignment of the chambers, since the X axis deviations show a very precise alignment in the studied scale (the distribution is almost symmetric, its mean is close to 0, and it is

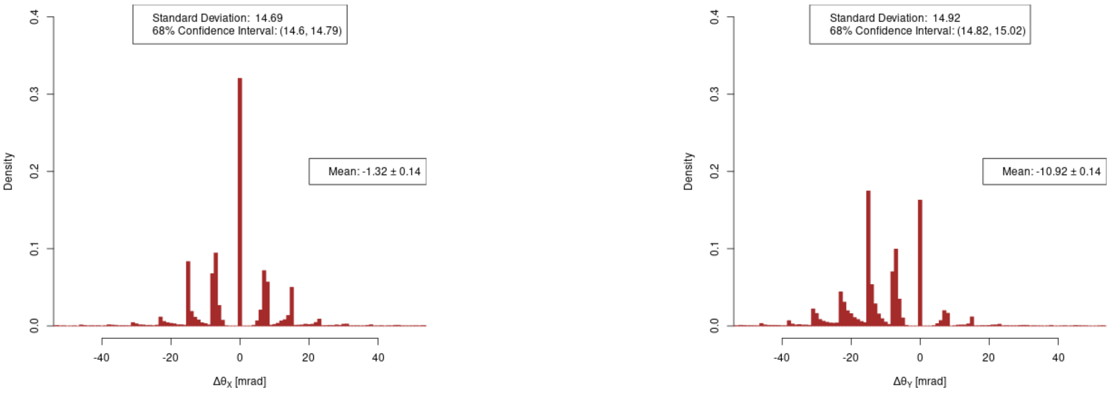

(a) 4 chambers (b) 4 chambers

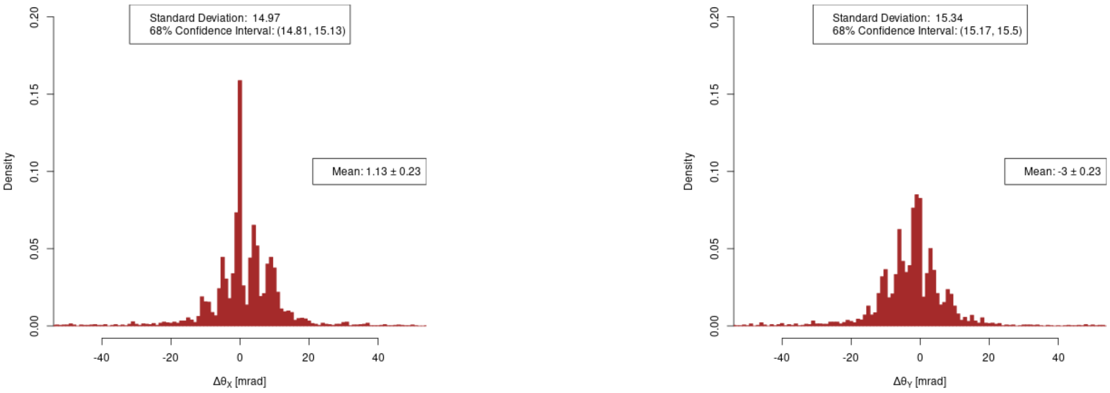

(c) 6 chambers (d) 6 chambers

Figure 3.24: Muon deviations measured in the laboratory with 4 and 6-chamber detection systems. Mean and standard deviation, as well as their confidence intervals for each probability distribution are specified.

very similar to perfectly aligned simulation deviations). It should be also taken into account that in laboratory measurements noisy events can be present, and also low momentum muons, which can undergo significant deviations, although they only traverse air and the material of the detectors.

With regard to chamber alignment, it is again observed a higher distortion and displacement of deviation distributions belonging to Y axis, while X axis distributions are practically centred. It is also worth mentioning that the Y-axis deviation distribution of the 4-camera measurement is clearly more skewed than that of the Y-axis of the 6-camera data. The mean of the distributions is an indicator of this bias. In 6-chamber measurements, the mean of the distributions is also smaller for the X axis, meaning that probably it is better aligned. Additionally, the shapes of the X axis deviation distributions are sharper, and the studied characteristic accumulations due to the finite resolution of the wires (see section 3.3.5) can be observed, particularly well in the case of 4 chambers.

3.4 Alignment of the chambers

The alignment of the chambers influences the reconstruction of the muon trajectories detected by the system, an thus, alters the analyses derived from them. It is a key aspect to achieve high precision measurements. The effect of the alignment has been studied using simulated samples. It should be noted that Muon Systems has devised strategies to mitigate misalignments and algorithms to estimate them using a system of external references and muon tracks.

In order to study the effect of misalignments a set of simulated samples has been produced adding artificially displacements to the layers measuring the Y coordinate. A total of five cases has been analysed: four cases in which layers 2, 4, 6 and 8 have been displaced by 1 mm, each at a time, and a case, in which layers 2, 4, 6 and 8 have been displaced by -1 mm, -0.76 mm, +0.76 and +1 mm respectively. It should be noted, that the latter case, corresponds to a so-called alignment weak-mode configuration. Indeed, layers have been shifted by an amount proportional to their Z position in the detector. This kind of configuration should not introduced any effect on the reconstructed distributions, since this kind of misalignment would be perfectly absorbed by the direction fit of the muon reconstruction.

In this simple study, the RMS and the mean of the projected muon deviations are studied, together with the tangent of the actual angle. fig. 3.25 shows the effect that the misalignments have on these estimators. It can be seen how the individual layer displacements impacts the RMS in the same way. For the means of the muon deviation and the tangent of the angle, a pattern emerges due to the definition of the angles, which always consider the same layer ordering. It should be noted as well, that, as expected the weak mode configuration does not produce any significant effect.

3.4.1 Alignment residuals monitoring

The alignment of the chambers has been monitored during a long campaign to collect 35 datasets with an exposure time of several hours. During this campaign some of the detectors were removed and inserted back.

The magnitude used to monitor the alignment has been the so-called residuals. Alignment residuals are defined as the difference between the actual hit position in a given layer, and the projected position using the fitted track. In fig. 3.26, the mean of the residuals for each chamber are shown. The main fact that the results indicate is the practically constant mean errors in the X coordinate, compared to the variability shown in the Y coordinate. This is due to the fact that the chamber movement is limited by the supporting structure in the X axis providing a good positioning, while along the Y axis, there is not any mechanical constraint, to allow to insert and remove the detectors. In particular, Y axis layers belonging to the upper chambers ("Capa 1", and "Capa 2") have undergone the most important variations. It is also noted that the alignment in the coordinate X, is worse compared to the initial Y axis configuration.

3.4.2 Alignment correction using the alignment residuals

A simple alignment correction method has been performed by using the residual distributions. Only the horizontal displacement of the layers has been considered in this analysis, neglecting vertical displacement and possible slight rotations. Residual distributions have been calculated for

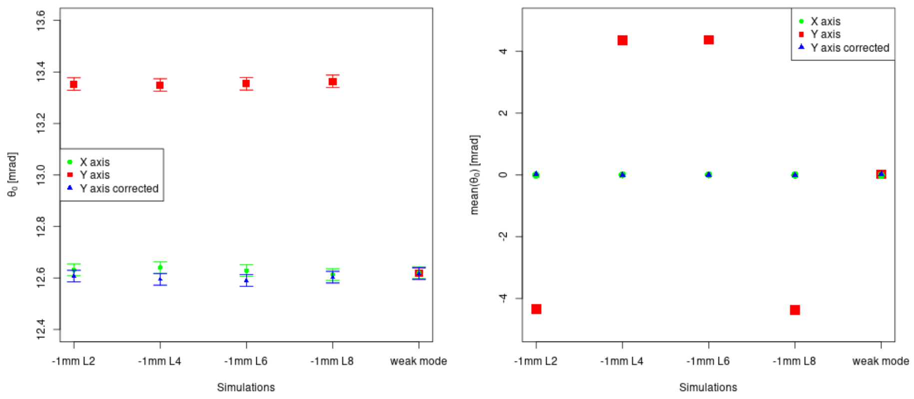

(a) $\Delta\theta$: root-mean-square (θ_0)

(b) $\Delta\theta$: mean

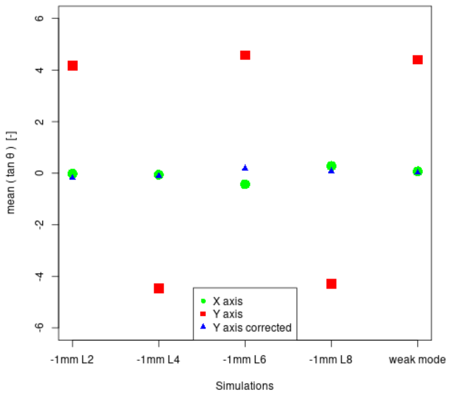

(c) θ: mean

Figure 3.25: Characterisation of measured projected muon deviations ($\Delta\theta$) and incidence angles (θ) for the different simulated cases. For the two first cases (-1 mm L2, and L4), the θ measured with chambers 1 and 2 are plotted, while chamber 3-4 θ are used in the 3rd and 4th cases (-1 mm L6, and L8). For the weak mode case, the mean of the tangents of both θ is shown. The statistical errors of the mean calculation are negligible.

every layer and the median has been used as an indicator of the layer misalignment. The choice is the median has been made in order to mitigate the effect of events in the tails of the distributions, probably coming from poorly reconstructed muons. Once calculated, the medians of the distributions are used as estimators of the misalignment.

In fig. 3.27, the residual distributions are shown for an experimental dataset collected with a 4-chamber setup. The X coordinate distributions are more centered that the distributions in the Y coordinate, indicating a better alignment. It is worth mentioning that this method is not able to account for all the possible misalignments. In particular, weak modes, as the one mentioned in the previous subsection are essentially invisible for this technique. The values of the layer misalignments obtained with this methodology can be seen in table table 3.11 using a 4-chamber and a 6-chamber setup. The data taking time of both measurements is approximately of 15 minutes.

The projected muon deviations ($\Delta\theta$) of 4 and 6-chamber measurements obtained with alignment

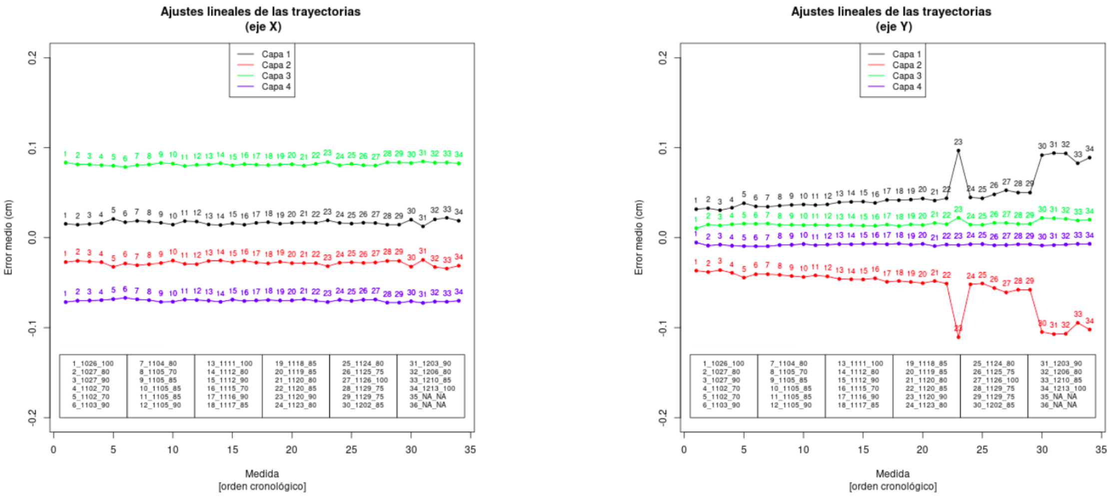

Figure 3.26: Chronological evolution of the mean error of fitted straight trajectories with respect to the reconstructed point coordinates (vertical axis), for a campaign of 35 measurements (horizontal axis). All the chambers of the detector (4-chamber system) are monitored.

		Alignment corrections [cm]					
		Ch1	Ch2	Ch3	Ch4	Ch5	Ch6
4 chambers	X axis		+0.00	+0.02	-0.05	+0.02	
	Y axis		+0.00	-0.17	-0.16	-0.00	
6 chambers	X axis	-0.09	+0.00	+0.01	-0.06	-0.01	-0.06
	Y axis	-0.32	+0.00	-0.22	-0.29	-0.19	-0.15

Table 3.11: Alignment corrections of the 4, and 6-chamber measurements in X and Y axes.

corrections and without them are shown in fig. 3.28. In both X and Y axis of the two measurements, after the alignment corrections the distributions are more centred, and also their width is slightly reduced. It should be remembered that all the distributions have been evaluated up to an absolute value of 100 mrad, removing only a small quantity of events that are probably due to noise, background, and low momentum muons.

The most noticeable correction is performed in the Y axis of the 4-chamber test, where the centre of the distribution is displaced around 11 mrad. Note that the estimated alignment corrections indicate almost 2 mm misalignment, in opposite direction, for the Y layers of upper and lower detectors. That is to say, between the two upper Y layers of Ch2 and Ch3, and also between the two lower Y layers of Ch4 and Ch5 (see table 3.11). In the Y axis of the 6-chamber measurement also important alignment corrections up to 3 mm have been estimated, but in this case the upper and lower detectors are less unbalanced. Estimated corrections indicate misalignment in the same direction for both detectors, i.e., the lower chambers of each trajectory detector are displaced towards the positive side (this configuration would be close to a weak mode). Probably the 6-chamber trajectory fitting also helps to smooth the chamber misalignment.

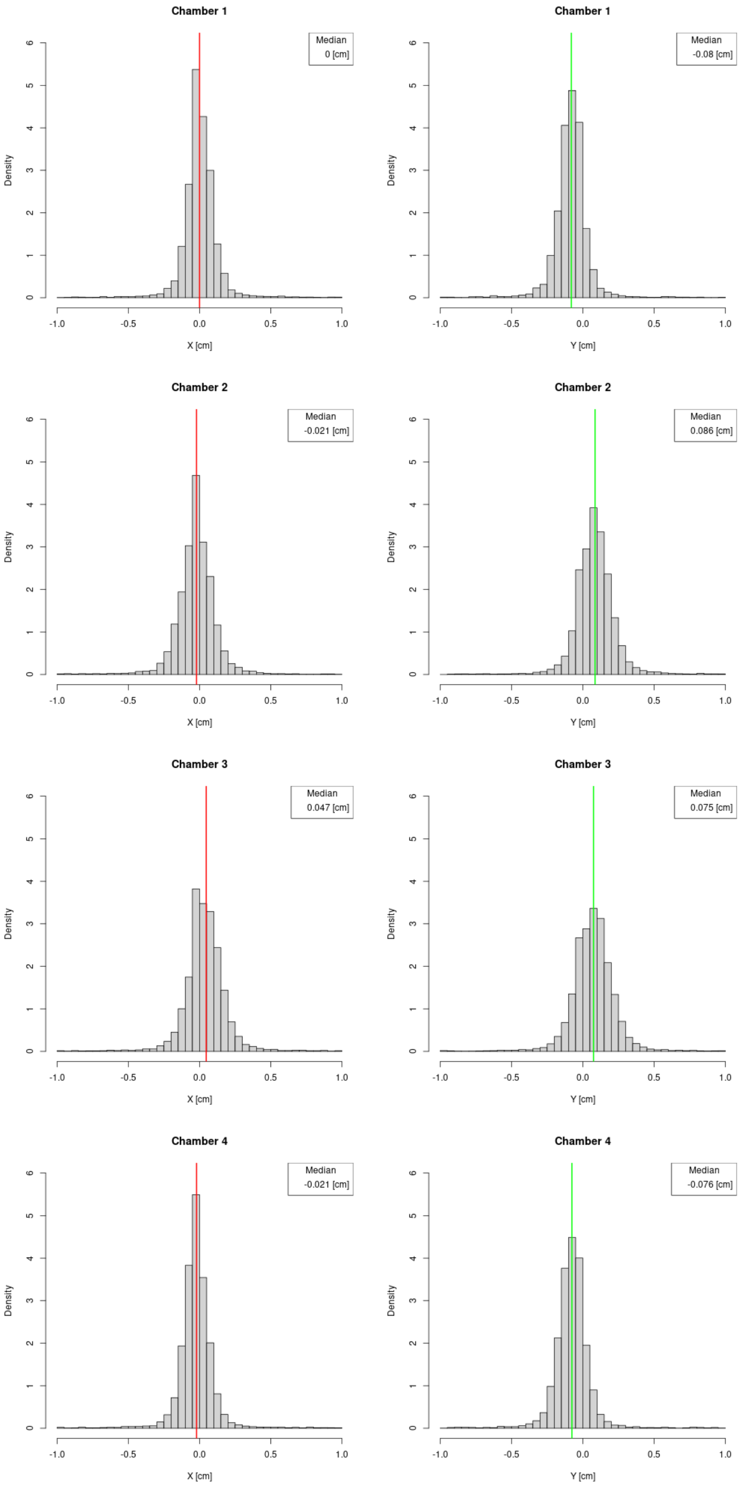

Figure 3.27: Errors of muon trajectories with relation to their fitted linear trajectories for all the detection layers. X axis data are in the 1st column (red) and Y axis data in the 2nd (green).

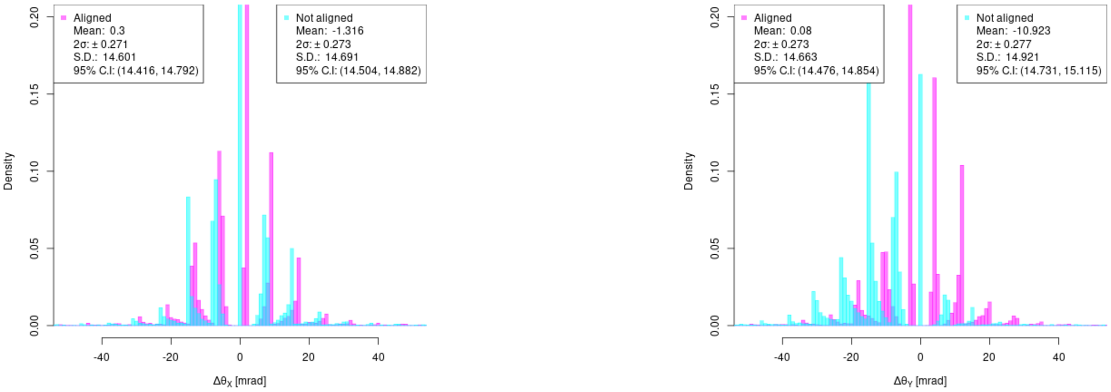

(a) 4 chambers

(b) 4 chambers

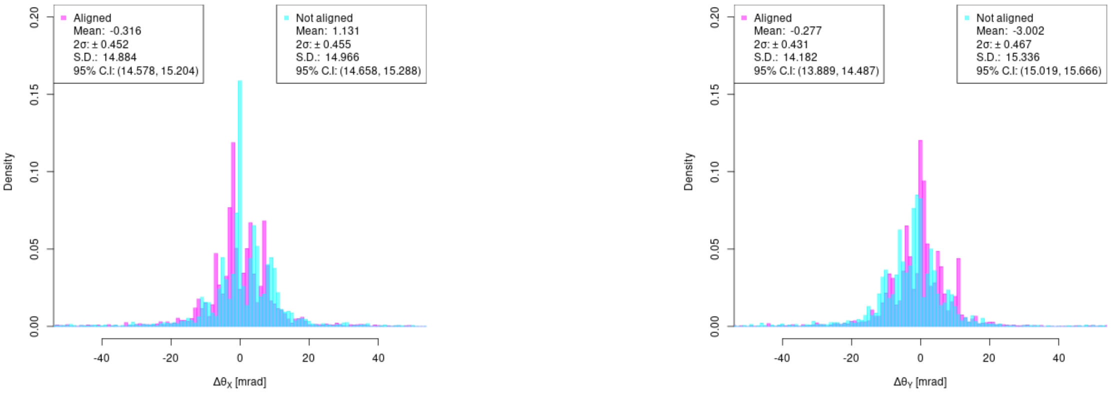

(c) 6 chambers

(d) 6 chambers

Figure 3.28: Muon deviations measured with 4 and 6-chamber detection systems, both with alignment correction and without it. Not aligned deviations have been already shown in fig. 3.24.

Chapter 4

Detection feasibility and imaging of cracks in concrete cylinders through muon scattering

This chapter summarizes the work performed in the context of a civil engineering muography application. In particular, the feasibility to detect cracks in concrete structures using MSR is explored. The results of this work have been shown and presented as a conference article [169].

4.1 Introduction

Since the introduction of muon radiography (MR) in the early 1950s, both absorption and scattering of muons have been used to map structures in archaeological sites and more modern buildings of civil use. Several successful experiments have been completed that have revealed important information about them. In those measurement and analysis campaigns, varied elements such as shafts, voids and cavities have been detected. Furthermore, important information about the stability of buildings and the condition of structural elements has also been obtained. Applications of the technique in the fields of civil engineering and archaeology, which are part of the background and motivation for this work, are reviewed in section 2.3.5.

In summary, it can be argued that MR is a valid technique for non-destructively exploring the condition of buildings and structures and may perform better than other techniques in certain environments and applications.

The following pages present a feasibility study of detection and imaging of cracks in scenarios composed of concrete cylinders. Using MSR, 15 cm diameter samples with full transverse cracks (2 cm and 1 cm of aperture) and with no crack, have been measured. The detection hardware described in section 3.1 was used to perform these experiments. The aim of the research is to assess the limits of the technique and the hardware, in a challenging situation with subtle detection targets. The nature and performance of the novel imaging algorithm are also explained, analysed, and discussed.

4.2 Experimental setup

The detectors used in this research were composed of four Multi-Wire Proportional Chambers (MWPCs), the simplest detection setup that allows muon scattering to be measured. As already explained in this thesis, each chamber consists of two perpendicular layers with 224 wires, all separated by 4 mm. In the lower part of the detector there are three chambers, but one of them is not active. The hardware can be seen in fig. 4.1 and detects four points of the muon trajectories, two points before, and two points after crossing the target. With these points, upstream and downstream trajectories can be reconstructed, and muon deviations can be calculated. The electronic synchronization system triggers the detection data readout when all chambers receive a signal within the detection time window. This condition distinguishes signals produced by muons from signals produced by other charged particles that can activate the anode wires. For additional information about the electronic readout and trigger systems consult section 3.1.2.

Figure 4.1: The MWPC detectors located in their structure with the concrete samples placed in between.

Two concrete cylinders (A and B) have been used to carry out the experiments. Both are cylindrical in shape, with 15 cm diameter and 30 cm height. Their mass, volume and density are specified in table 4.1.

Sample	Mass $[Kg]$)	Volume $[cm^3]$	Density $[g/cm^3]$
A	11.35	5300	2.14
B	12.90	5300	2.43

Table 4.1: Mass, volume and bulk density of the two concrete cylinders utilised in the experiments.

The investigated scenarios have been created with the two concrete samples. The first scenario, which is represented on the left photograph of fig. 4.2, consists of a unique concrete cylinder (sample A) that represents an intact concrete structure. On the other hand, the other scenario, which is shown in the right photograph of fig. 4.2, as well as in fig. 4.1, recreates a cracked concrete structure with the two cylinders. This scenario has been used to measure 2 cm and 1 cm aperture cracks. The purpose of the study presented in this document is to analyze the 20 central centimeters along the longitudinal axis of the cylinders and find out if the cracks can be detected. Note that the analysed volume is smaller than the dimensions of a unique concrete cylinder (30 cm).

Figure 4.2: On the left, the scenario used to emulate an intact concrete structure. On the right, the scenario of the cracked concrete structure.

4.3 Dedicated reconstruction algorithm

The reconstruction algorithm used to obtain the results shared in this paper was tested in previous studies with simulations of these type of scenarios. The simulations were computed with the simulation software described in section 2.3.3, using CRY particle generator and Geant4. One of the most widely used algorithms in scattering muography is POCA (Point Of Closest Approach), which assumes that all the scattering of a muon occurs in a single interaction point. In these previous studies, the POCA algorithm was also evaluated but results were not encouraging in terms of the performance of the crack detection. Motivated by this, an alternative reconstruction algorithm has been developed, that makes use of roughly the double of muon flux compared to POCA. This difference is due to the lack of precision of reconstructed POCA scattering centres, mainly for muons of low angular deviations. The estimation of POCA centres in this type of muons, usually leads to noticeable imprecision. Therefore, the scattering of an important amount of muons that actually cross the target, is not located accurately by POCA algorithm. This new algorithm exploits the fact that the relative position of the detectors and the samples is known a priori. Because of that, it is possible to identify in a precise way which muons cross the space where the sample is located. In fig. 4.3, the points where the muon presumably enters and exits the target volume are shown in red and green, respectively. These calculations are made according to the detected trajectories, and the data shown in the figure have been extracted from one of the datasets collected with the concrete samples. Since the objective in this application is to detect vertical cracks, a specific way of segmenting the sample space is used. The muons are allocated into vertical sections (slices) of 1 cm width based on the zone where they cross the approximate location of the concrete sample. Its volume is divided in slices of 1 cm width, and muons crossing each of them are selected. Note that non-vertically incident muons can cross and form part of the statistics gathered by various slices. Then the amount of scattering in each vertical section is analyzed.

Under these conditions, small muon deviations are expected in the slices where the cracks are

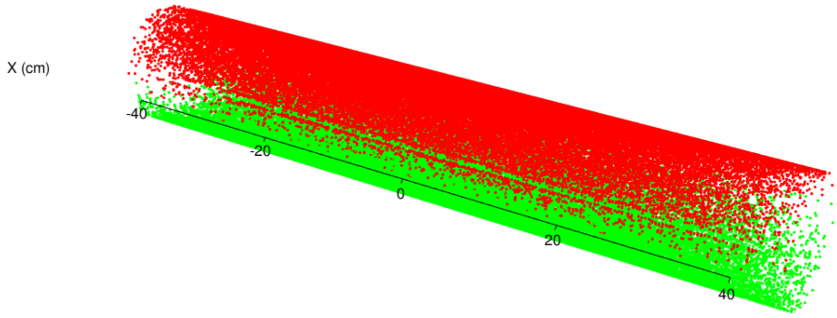

Figure 4.3: Estimation of the points where muons enter (red) and leave (green) the volume occupied by the concrete samples.

located. According to the multiple scattering (section 2.2.5) undergone by muons, their deviations projected onto a plane result in a Gaussian distribution with approximately 0 mean, whose width indicates the amount of scattering. Density images have been built quantifying the width of the muon deviation distributions crossing each vertical section. Particularly, the median of the absolute value of the deviations is calculated. This statistical measure behaves in a stable manner in measurements with noisy events that introduce large deviations. The background noise affecting muography has been already discussed in section section 2.2.3.

4.4 Results

According to the scenarios mentioned in section 4.2, three datasets have been collected: the first, using a non-cracked concrete structure, and the second and third, with full transverse cracks of 1 cm and 2 cm, respectively. Both cracks were roughly centred in the detection volume covered by the detectors. Regarding the measurement efficiency, the presence of background noise has been identified. Taking into account this situation, the detected events have been filtered using the *post-processing function* described in section 3.2.2, probably losing part of the muon flux passing through the detectors. Specifically, the 4-MWPC filtering strategy has been applied, in this case, not imposing a maximum scattering angle limit.

The reconstruction obtained using the algorithm described in section 4.3 is presented in fig. 4.4. The origin of the coordinates is referenced to the center of the scanned space, which is determined by the position of the detector. Both cracks are detected, reconstructing them slightly off-centred, about 1 cm from the positive side of the longitudinal axis. These deviated reconstructions of the locations of the cracks suggest that the samples were also displaced. This fact was later confirmed by direct measurements of the cylinders performed in the laboratory. As shown in the reconstructed images, the vertical sections where the cracks are located have statistically smaller muon deviations compared to all others. In the case of the 2 cm crack, these differences are more pronounced. The data taking time of each muography was 15 hours.

To confirm these results, a fourth measurement has been performed. In this case, a 2 cm crack

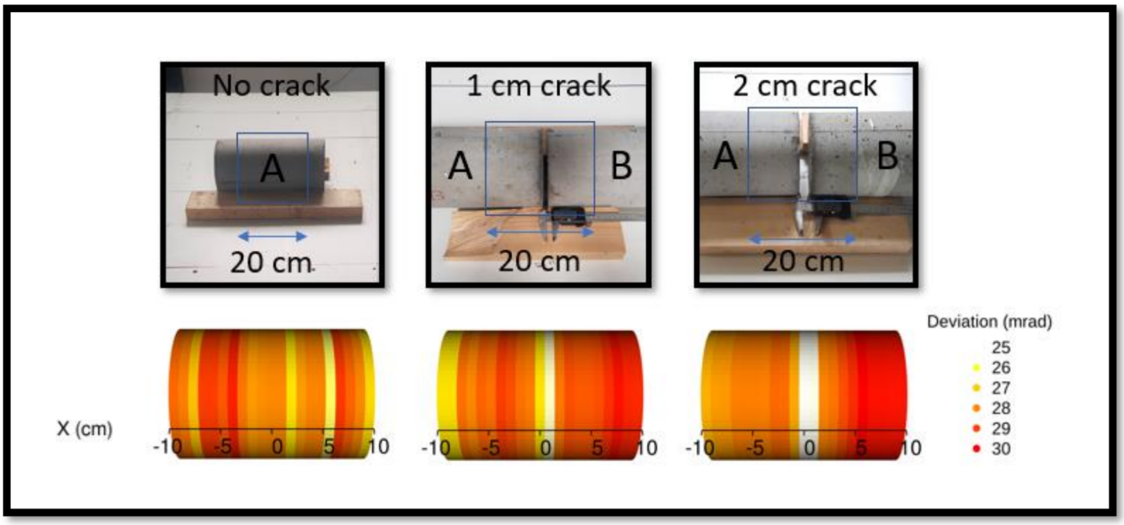

Figure 4.4: Reconstructed images of the scenarios with the concrete cylinders. On the left, intact structure. On the centre, the 1 cm crack. On the right, the 2 cm crack. The scanned space is marked in blue.

has been scanned, but its location has been moved 3 cm to the negative side of the longitudinal axis, compared to the previous cracks. In this fourth reconstruction, the crack has been once again clearly imaged, although its aperture appears to be of 1 cm. It is also worth mentioning that the highest deviations are obtained on the negative side of the X axis, where the concrete sample B is located (fig. 4.5). Note that the cylinder B is heavier than cylinder A (table 4.1). The highest deviations in the reconstruction of the previous measurements of the 1 cm and 2 cm cracks also highlight the location of sample B (fig. 4.4).

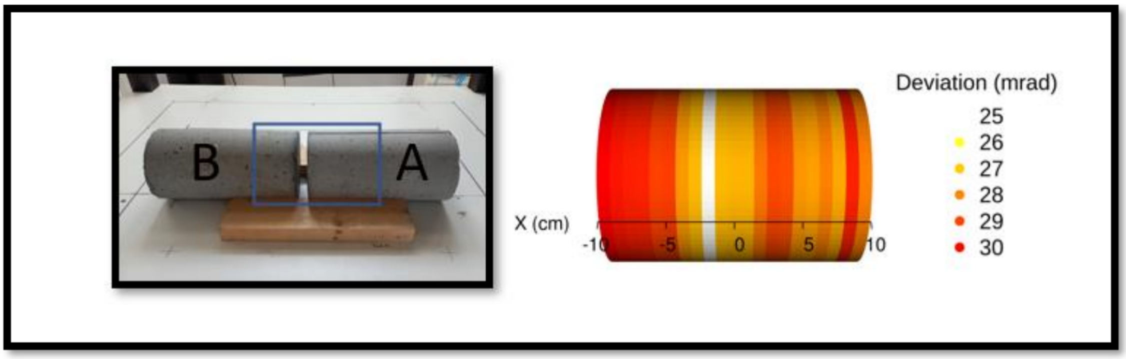

Figure 4.5: The concrete structure with a displaced 2 cm aperture crack. It has been moved 3 cm to the negative side of X axis.

4.5 Discussion

Cracks between the concrete cylinders and their locations are detected in all the datasets. However, the estimation obtained for the aperture of the crack of the fourth measurement has not been correct. The reconstruction shows a 1 cm crack instead of 2 cm. It should be noted that the width and position of the slices have not been optimised for the application. A more narrow slicing would provide higher granularity on the detection of the cracks, at the cost of sacrificing statistics in the number of muons assigned to each slice. On the other hand, the position of the slices can also affect the results, since they can cover completely, or only partially, the area of the cracks. This fact could yield misleading results.

In any case, the presence and location of the cracks have been correctly assign for all the datasets. As shown in the preliminary analyses of section 3.3.4, the use of a detector with six MWPCs could contribute to improve the reconstruction efficiency. This detector configuration has a better spatial and angular resolution, and would surely provide a more accurate estimation of the cracks.

4.6 Conclusions

The presence of cracks of 1 cm and 2 cm width has been detected with the MSR technique. The absence of about 0.4 kg of concrete is reflected in muon deviations and the detector can measure this change. A dedicated algorithm has been implemented to detect cracks and estimate their size. Additionally, the high density of one of the cylinders is clearly imaged in the measurements. The density of the light cylinder is 2.14 g/cm^3 (sample A), while the density of the heavy cylinder is 2.43 g/cm^3 (sample B). It is worth mentioning that the proposed algorithm makes efficient use of the information contained in all muon events, even in the less scattered, which are difficult to reconstruct properly with the POCA algorithm.

This study is an additional proof of the potential of MSR as a Non-Destructive Testing technique to detect defects in concrete structures. It has been shown that the technique is capable of finding small defects at the centimetre scale. These detection capabilities along with its penetration power make the muography useful in civil constructions and buildings. Future progress in the detection hardware and reconstruction algorithms can significantly improve the performance of the technique. The development of algorithms based on maximum likelihood estimation and adapted to the studied application could improve the results obtained in the presented research.

Chapter 5

Snow Water Equivalent monitoring by means of scattering muography

In this chapter, the research performed related to the estimation of the *Snow Water Equivalent* (SWE) using MSR is summarised. It should be noted that the work presented in this chapter has been already published in a high-impact factor journal [107]. Preliminary investigations were also presented in an important European geoscience congress [171].

5.1 Introduction

Seasonal snowpack plays a major role in the hydrology of areas where it is present and beyond [172], but its real-time monitoring is still a big challenge for the scientific community and water management agencies. Real-time monitoring systems rely heavily on remote sensing and numerical modelling. However, to date, there is still no effective approach to retrieve the *Snow Water Equivalent* (SWE) from orbital sensors, especially over complex terrain [173]. The SWE is usually measured as the depth of water that the snowpack would be transformed into if it melted completely. It can be measured over a specific region or within a limited surface. It is calculated as the product of the vertically-integrated density times the snow height, and is usually measured in millimetres. Furthermore, even the most sophisticated physically based snowpack models suffer from limitations [174], and uncertainty due to wind and avalanche snow redistribution [175].

Direct observations of snowpack are highly appreciated for water management purposes, long-term climatology studies, as well as model and remote sensing product building and validation. Nevertheless, as a result of the difficulties and increased costs of snowpack monitoring, available SWE time series are often scarce, incomplete, or simply non-existent [176]. Furthermore, although snow depth retrieval is nowadays possible using relatively cost-effective techniques [177], monitoring of SWE remains elusive.

Traditionally, SWE monitoring techniques have been based on snow pillows. These sensors are able to measure the SWE based on the pressure increase caused by snow on the surface below. Snow pillows exhibit a number of limitations that prevent their use in certain environmental conditions, and in many applications. Their installation requires very complex logistics and, in addition, these devices require frequent manual re-calibration [178]. Moreover, their accuracy is very limited in transient or shallow snowpacks. Direct and invasive measurements of SWE using snow core samplers also have uncertainties of more than 10%, which are even more pronounced for deeper snowpacks [179]. In this context, the use of cosmic-ray neutron-based sensors is not uncommon, which is the solution chosen by many water agencies for their operational networks. It is possible to deploy neutron-based monitoring networks even in mountainous or remote regions [180]. However, their precision is still limited and requires proper calibration. Despite the relative success of neutron-based techniques, there is still a need for scientific innovation in the field of SWE sensors. For this reason, the development of technologies with the ability to measure SWE is an active area of research, where new designs based on different physical principles have been proposed [181].

As explained in section 2.2.4, muons are leptons, elementary particles similar to electrons but with about 207 times more mass. Cosmic rays, i.e., very high-energy particles and nuclei that constantly reach the earth from deep space, collide with the upper layers of the atmosphere. In these collisions, showers containing several types of secondary particles are produced (see section 2.2.1). Some manage to reach the Earth surface, and among them, muons are the most abundant charged particles at sea level (see section 2.2.3). More information on the nature of cosmic rays, and muons in particular, can be found in section 2.2.

Thus, cosmic muon production is a very common natural phenomenon. Muons exhibit high penetration capabilities, making them interesting candidates for the development of SWE sensors. Although they have great potential, their use as a resource for measuring SWE remains largely unexplored. Consequently, there is a lot of scope for research and development in this area.

There are two different ways to perform a muography: quantifying muon absorption or muon scattering. The Muon Absorption Radiography (MAR) method, as explained in section 2.3.1, utilises muon counts to extract information about the matter in the line of sight of the detector. On the other hand, the Muon Scattering Radiography (MSR) is based on the measurement of muon deviations (see section 2.3.1). Recently, Gugerli et al. [134] applied MAR and proved the potential of muon counters to estimate SWE in the field, comparing muon count rates with in situ SWE measurements. It is also worth mentioning that MAR has been used in other applications to hydrology, such as the study of ice-rock interfaces in glaciers [70, 71].

The MAR approach presents some practical advantages with respect to MSR. For example, the application of MAR only requires one detector to measure the muon flux below the snow, although a reference of the flux above it is also needed. In contrast, MSR requires the continuous measurement of two detectors to collect the muon deviations: one detector would be placed on the ground before the snow season, and the other would be located above, considering the expected snow levels, and using some artificial or natural structure. Nevertheless, the MSR technique is, in general, more precise than the MAR and would allow additional and interesting features, such as the estimation of the density profile of the snowpack.

This study has two main objectives. The first one is to estimate the SWE through detailed analysis using the SNOWPACK model and muon numerical simulations. The second consist in testing the capabilities of the real-world hardware described in section 5.2 to measure the SWE of artificial snow samples. It should be mentioned that this work focuses on the scientific proof-of-concept of the technique, but does not develop the practical details of its application to the relevant environment.

5.2 Experimental Setup

The muon data analysed in this research have been collected with the muon detection system already described thoroughly in this thesis, which is shown with the box used to build the snow samples in fig. 5.1 (c). During this study, a 4-MWPC configuration has been used, forming a similar setup to the one applied in the experiments of the previous chapter 4. It is worth mentioning that in the statistical analysis of this chapter, the projection of muon deviations in two planes perpendicular to the anode wires has been used, in agreement with the deviations represented by θ_0 in eq. (2.21).

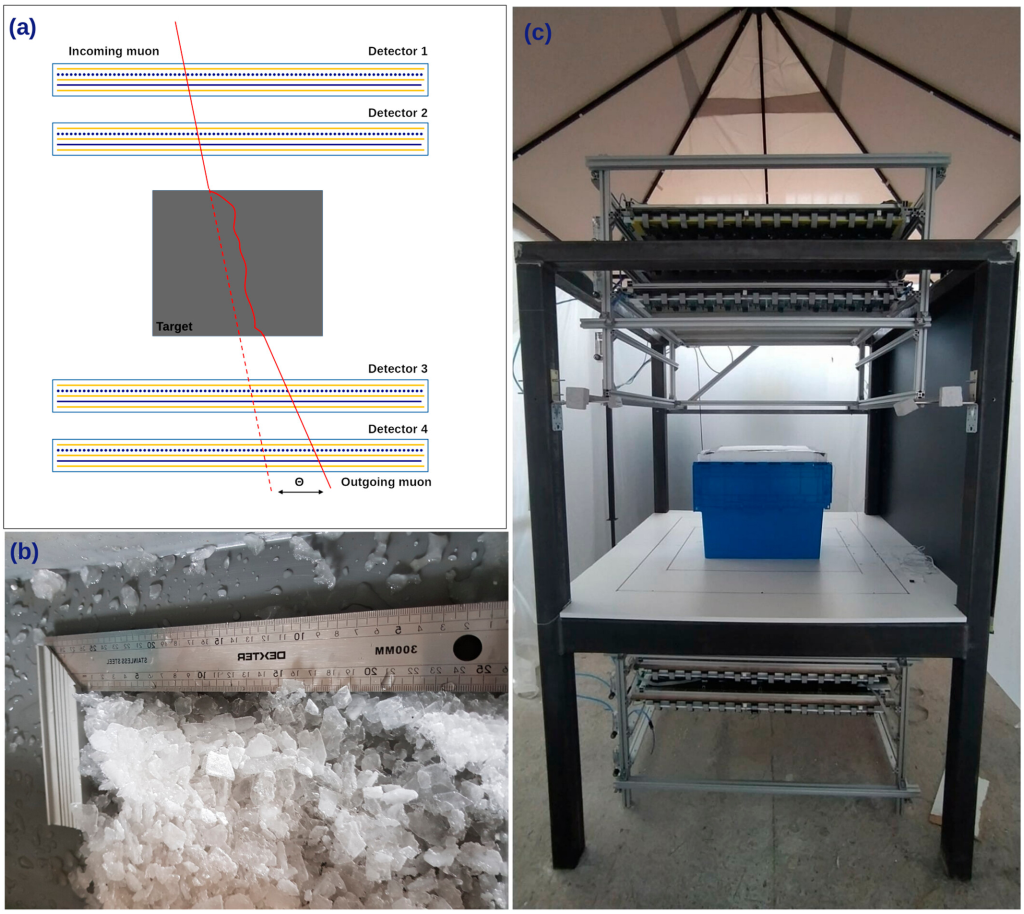

Figure 5.1: (a) Explanatory drawing of the MSR setup: the muon trajectory is deviated while crossing a dense target. (b) Detail of the crushed ice used to build the artificial snow laboratory samples. The dimensions of the pieces of crushed ice are around few millimetres. (c) The laboratory MSR detection setup, with a sample in between the upper and lower chambers.

It should also be mentioned that muons with projected deviations higher than 100 mrad have been rejected, aiming to reduce the noise sources discussed earlier in this thesis in section 2.2.3. The proportion of rejected muons has been maximum for the highest SWE samples. However, even in these cases, it has not exceeded the 2.5% of detected muons in simulation, and the 3.7% of the events acquired in the laboratory. Note that among the events collected by the laboratory detector there may be signals that are not due to synchronous muons.

5.3 Simulation Setup

The snowpack has been simulated using a one-dimensional snow model which considers surface meteorological data. The SNOWPACK model [182] [183] [184] has been used to realistically generate the snow cover behaviour during two seasons, 2015/2016 and 2015/2016. SNOWPACK is a physics-based multi-layer model that simulates snowpack conditions and micro-structure. It is based on snow energy and mass balance, and is widely used for both research and operational snow avalanche prediction. For this study, SNOWPACK has been forced by the ERA5-land surface reanalysis [185]. The simulations have been performed considering a location in the Pyrenees, specifically the ERA5-Land cell which is closer to the Monte Perdido massif (42.7°N, -0.1°E), at an elevation of 2041 m above sea level. The main objective of these simulations has been to compute detailed snowpack state variables that evolve realistically with time. They have provided information on the different conditions in both accumulation and melting periods, as well as on its internal structure. Once the SNOWPACK simulations were done, the snow, liquid water, and air content of each variable-thickness snow layer forming each snowpack sample have been collected.

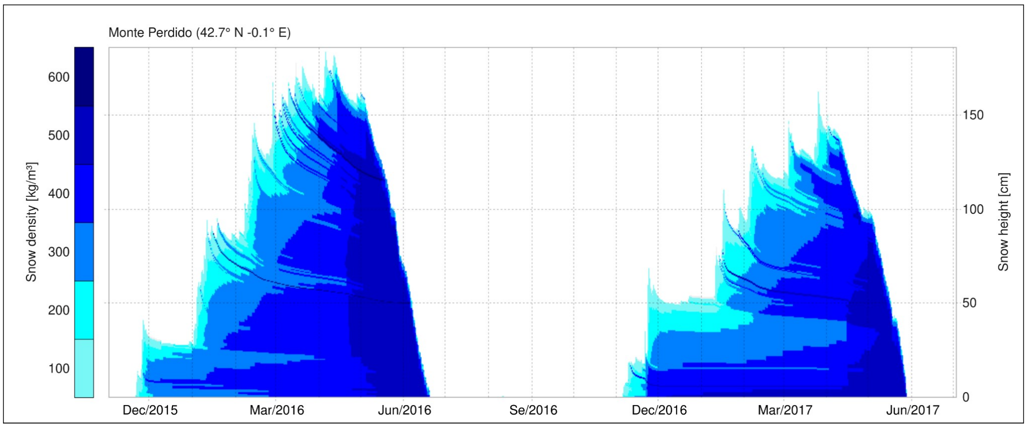

Figure 5.2: Snow cover time evolution simulated with SNOWPACK model for 2015/2016 and 2016/2017 hydrological seasons. Different colors indicate the density of each snow layer composing the snowpack.

The data generated by SNOWPACK model have been coupled with the Geant4-based simulation setup described in section 2.3.3. CRY has been used to generate the muon flux. After the completion of numerical SNOWPACK simulations, the data have been extended to a 1 m^2 snow column, assuming uniform snow layers in longitude and latitude dimensions. Then, muons passing through the detectors and penetrating the snow column have been propagated and measured, virtually reproducing the detection process and obtaining θ_0 for different snow accumulations during the two simulated seasons.

5.4 Analysis strategy

The angular resolution is crucial in MSR application [186]. It is determined by the spacing of the wires, and by the separation of the layers of each trajectory detector, as already explained in section 3.3.5.

To demonstrate the ability to predict SWE and explore the previously discussed influence of detector resolution and materials, MSR data generated under different conditions have been analysed. Four simulation scenarios have been created to study in detail the factors affecting the resolution and the changes produced by the detector material. The first scenario considers an ideal muon detector with unlimited spatial resolution, and neglects the effect of the detector material. In the second scenario, the effect of the material has been taken into account, but still assuming an unlimited spatial resolution. The third scenario also considers the detector material, and the spatial resolution is degraded by setting the wire spacing to 4 mm. These three scenarios have been configured with a detector layer spacing of 257 mm. The layer spacing represents the vertical distance between upper and lower chambers of both trajectory detectors, the one above the target, and the one below. The intrinsic angular resolution for the scenario 3 is about 9 mrad. The fourth scenario is similar to the previous, but using a reduced detector layer spacing of 130 mm, which is consistent with the configuration of the laboratory experimental setup. Finally, measurements on ice blocks of different heights have been performed in order to to assess the functioning and ability of our hardware, and to confirm the simulation results. In the case of the fourth and fifth scenarios the intrinsic angular resolution is about 18 mrad. For each of the explained scenarios the correlation between measured muon deviations and SWE has been quantified.

For each of the generated simulation scenarios (1, 2, 3, and 4), weekly measurements of 5 hours taken during the hydrologic year 2015/2016 (fig. 5.2) have been analysed. These simulations have been used to model the relationship between θ_0 and SWE under different conditions. The aim has been to study the effect of the wires and the separation of the chambers on the intrinsic spatial resolution of the detection system, as well as the influence of detector material. Finally, additional validation data have been produced, considering resolution and conditions of the scenario 3. Measurements for the entire hydrologic season 2016/2017 have been simulated, collecting continuous measurements of 5 hours.

The laboratory experimental setup has been used to scan artificial snow samples of known density and volume. The samples were composed of crushed pieces of ice, imitating real snow (fig. 3.12 (c)). The different granularity of the material has no significant influence on these experiments, given that what it is measured, is the total angular deviation produced by the multiple scattering of muons. Note that this magnitude depends mainly on the composition and bulk density of the traversed material (see section 2.2.5).

The first measurement has been used to quantify the intrinsic θ_0 observed in the setup. The target used in this test consisted only of the box used to prepare the samples, with no material in its interior. In the second measurement, 10.60 Kg of material have been introduced, with a bulk density of 448.70 Kg/m^3 and reaching a height of about 22.3 cm. Its SWE was roughly of 99.8 mm. In the last and third laboratory sample, 21.20 Kg of material have been used, with a bulk density of 494.92 Kg/m^3. It has reached a height of 40 cm and summed 197.97 mm of SWE. A single 5-hour measurement has been performed for each sample.

Mathematical models have been built linking the known SWE of the snow samples to the *root-mean-square* (RMS) value of the muon angular deviations (θ_0). Those models consist in the addition of two terms: A constant term (p_0), which absorbs the offset produced by the intrinsic resolution of the system, and a second term which is proportional to the square root of the SWE. The latter component responds to the hypothesis of proportionality between SWE and the number of radiation lengths of the target.

$$\theta_0 \;=\; p_0 \;+\; p_1\sqrt{SWE} \tag{5.1}$$

The equation 5.1 has been applied and fitted to all the scenarios, expecting to obtain different adjusted parameters p_0 and p_1 for each of them. These differences would be related to the characteristics and configuration of the detectors considered in each case. Other functional forms have been tested to fit the data, but the one explained here and represented in the equation 5.1 provided the best results. It has been considered optimal, taken into account this application, and also the current limits of the muography technique.

5.5 Results

θ_0 has been modelled as a function of the SWE using equation 5.1. All the described scenarios of simulated and laboratory artificial snow samples have been characterised. Figure 5.3 shows the results, including the parameters of the fitted functions and a measure of the correlation.

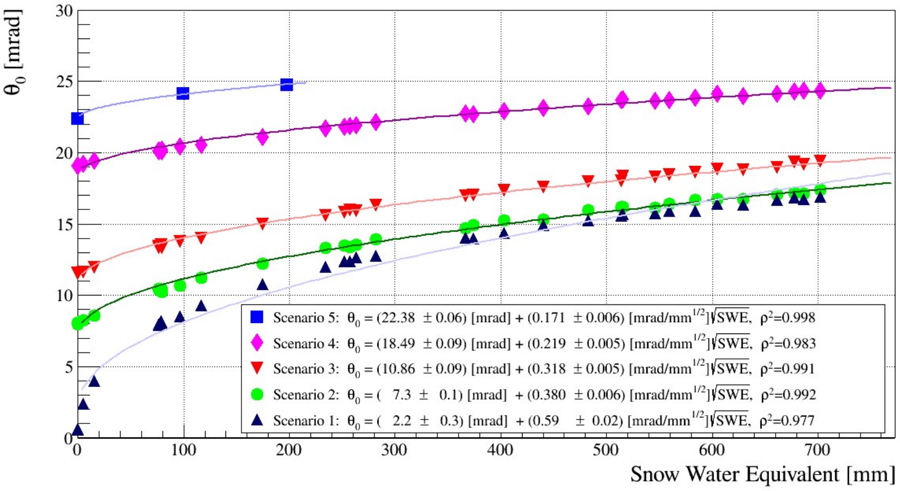

Figure 5.3: RMS of muon scattering angles (θ_0) as a function of Snow Water Equivalent (SWE) in the studied scenarios. The fit parameters p_0 and p_1, as well as the coefficient of determination for each case are specified.

As expected, the observed data are in accordance with the mathematical model defined, fitting accurately to different root square functions. The coefficient of determination between the two variables is around 0.98 in all cases. Only in the scenarios 1 and and 4, a slight reduction is noticed. As mentioned above, all the scenarios follow the expected square root relationship, but each of them has different function parameters p_0, and p_1. There is a noteworthy bias at 0 mm of SWE (p_0 variation), and also changes on the intensity of the increment of θ_0 in relation to the SWE (p_1 variation) depending on the scenario. These results show an increase of θ_0 linked to the material of the detectors, and to the reduction of their resolution. The rise of θ_0 due to detector material decreases significantly when the SWE of the measured sample is incremented. In contrast, the increase of θ_0 produced by detector resolution is almost constant in the simulated SWE range.

In the results obtained with the two setups using unlimited resolution (scenarios 1 and 2), the increase of θ_0 due to the detector material has been be observed. Note that it is more significant in lower SWE measurements. Scenarios 2 and 3 show the θ_0 increase produced by the limited resolution of the detection wires. Furthermore, between scenarios 3 and 4, a rise of θ_0 produced by the change of the detector separation is noticed. And finally, laboratory measurements show the highest θ_0 values for samples with SWE up to roughly 200 mm. The main differences between the laboratory setup and simulation scenario 4 are the accuracy of detector alignment, the presence of additional structures made of steel and wood, noise and effects not considered in simulation, and the snow samples themselves. Some of these factors are probably responsible for the high θ_0 values obtained in the laboratory. It is also important to mention that the laboratory measurements were performed inside an industrial building, which has a concrete roof of about 10 cm thick. This detail was not included in the simulation, and it could slightly affect the muon flux.

To estimate the SWE of additional unknown snowpack samples, a SWE estimation function for scenario 3 has been specified, derived from its fitted model (fig. 5.3):

$$SWE_{\mu}\ [mm] \ = \left(\frac{\theta_0\ [mrad]\ \ -\ \ (10.86 \pm 0.09)\ [mrad]}{(0.318 \pm 0.005)\ \left[\frac{mrad}{mm^{1/2}}\right]} \right)^2 \tag{5.2}$$

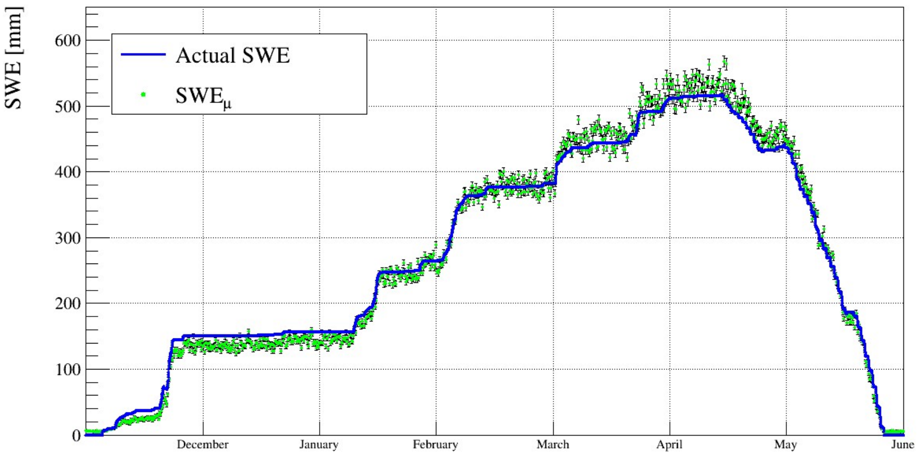

Figure 5.4: Validation of the SWE estimation in the scenario 3 with data of the season 2016/2017. The green dots represent the estimated values using eq. (5.2), while the blue line indicates the actual SWE. The black bars are the uncertainty of the model, which is based on the propagation of the fitted parameter variance. In the horizontal axis, the beginning of each month is signalled.

Where SWE_{μ} is the SWE estimate obtained by means of MSR, and θ_0 is the RMS value of the muon deviations collected, both in the same measurement. To validate the SWE estimation function, it has been tested with independent simulations of snow measurements. For that purpose, data from the season 2016/2017 has been used. The results are shown in fig. 5.4. They yielded a *Root-Mean-Square Error* (RMSE) of 11.5 mm, underestimating the SWE during the minimum accumulation periods, and overestimating it in the highest snow accumulations. An average underestimation of 9.4% (14.3 mm SWE) has been obtained during the month of December, while the overestimation in April has been of 3.3% (15.7 mm SWE).

5.6 Discussion and Conclusions

This work demonstrates that MSR can be used to determine the SWE, and therefore, can be a viable technique to contribute to solving the existing challenges in real-time snowpack monitoring.

Precise snowpack simulations have been computed, and with them, a simulation model that identifies the relationship between muon deviations and SWE have been developed and validated. The theoretical reference of muon scattering represented by eq. (2.21), and existing studies analysing similar relations [187] also agree with the results obtained in this research. Furthermore, the simulation model is consistent with the three snow measurements performed in the laboratory, proving the agreement of the simulations with reality.

The larger values of θ_0 obtained with the laboratory measurements can be explained by the presence of the detection structure shown in fig. 5.1 (b), by slight millimetre-scale misalignment of the chambers (see section 3.4), and by noise detection. The background noise influence can be minimised with particular detector designs, such as configurations including redundant chambers. A demonstration of noise filtering and reconstruction efficiency improvement using 6 MWPCs has been presented in the previous section 3.3.4. The real-world factors discussed at the beginning of this paragraph are not included in the simulations, and they affect the muon deviations measured in the laboratory. The structure can produce additional deviations in some of the muons used to scan the snow sample, while poor alignment and background noise produce misleading and usually augmented measurements of the deviations. It should be also mentioned that the laboratory measurements have been made inside a building with a concrete roof of about 10 cm thick. This fact influences the momentum distribution of the muon flux measured. The simulations do not include the building roof. As minimum ionising particles, muons lose roughly an average energy of 2 $MeVg^{-1}cm^2$, which corresponds to 48 MeV considering that they traverse 10 cm of concrete with a density of 2.4 g/cm^3. This loss of energy is negligible, since it is roughly the 1% of the average cosmic muon momentum at sea level. Minor differences related to the composition and granularity of the target material could also have a slight influence. In any case, and despite the subtle differences and uncertainties mentioned, the consistency achieved is a very promising point regarding the possibility of using simulation data for SWE detection modelling, calibration and testing.

Although the agreement and coherence of data initially obtained matched the expectations, additional studies in order to analyse various factors that affect the SWE modelling process have been performed. Specifically, detector resolution and material influence on measured muon deviations has been quantified. The quality of deviation measurements depend on detector resolution, and in these experiments most of the muons undergo slight deviations (on the order of tens of milliradians). Therefore, when the resolution gets worse, the measured deviations increase significantly. On the other hand, the detector material produces an increase of the actual scattering undergone by the detected muons. In conclusion, both detector resolution and material influence the relationship between measured deviations and SWE. This fact makes necessary a specific modelling depending on the detection setup. But above all, it is significant that the coefficient of determination between the two variables is 0.98 or higher in all the measurement scenarios. In relation to measurements performed in the laboratory with the hardware, it would be desirable to make progress in exploring the potential of MSR and to test the technique in the field.

The simulation model has been also validated assessing its predictions for additional and independent continuous measurements simulated for the hydrologic year 2016/2017. The assessment yielded successful SWE estimates, with an average RMSE of 11.5 mm considering the whole year. This last validation demonstrates the ability of the technique to continuously monitor the SWE using a model built with weekly measurements of a unique season.

Features of muon radiation, such as its penetrating power, innocuousness, and the nature of scattering, make MSR a promising technique for real-time SWE monitoring. The technique has also the ability to infer the density and composition of its target, allowing to identify physical properties of the materials [188], as well as their internal density distribution [189]. The described potential may eventually lead to the estimation of the density profile of the inner layered structure of the snowpack. By studying the characteristics of muon scattering through their trajectories, and applying advanced muography algorithms the snowpack internal density distribution estimation could be eventually achieved, and voids or weak layers could be identified. Algorithms which have been already described in this thesis such as those based on maximum likelihood expectation maximisation (section 2.3.4) and machine learning (section 2.3.4) could be suitable options for this task. The results of this proof-of-concept are a source of encouragement, and invite to additional research on the practical use of MSR as a tool to monitor the SWE.

Chapter 6

Estimation of the liquid steel fill level in a ladle furnace

This chapter studies other muon tomography application in the context of the heavy industry. A solution based on MSR is provided for the so-called problem of the ladle furnace. These objects, ladle furnaces, are large containers in which melting minerals are transported from a place to another in a factory. Because of the impurities of the minerals, usually, a layer of slag appears on top of the mixture. This layer is opaque and makes difficult to estimate the actual level of melted mineral below, which ends up causing inefficiencies in the factory workflows. The studies performed in this chapter are all based on simulated data. In addition to the MSR itself, this work has been done in the context of a new technique to determine the best possible detector configuration and geometry for this particular problem. This technique is encoded in the so-called TomOpt software, being developed by the MODE collaboration. Through the work presented in this chapter, a contribution has been made to the project.

TopmOpt is a muography simulation-optimisation software which is still in development. It represents the first step within the MODE collaboration to apply a fully differentiable particle detector optimisation pipeline. The approach consists in using the scattering muography as a use case, but the optimisation algorithm itself could be useful in the future for further applications and experiments of particle physics. At the same time, it is an attractive idea for the field of muography, as the algorithm allows to find optimal detector configurations.

6.1 TomOpt: scattering muography optimisation by means of differential programming

The TomOpt framework is composed of different software modules which simulate all the aspects of muography, and at the same time optimise the detector parameters of a specific scenario based on a loss function which takes into account the performance of the detection. The loss function can also consider additional parameters, such as the financial cost of the detectors or constraints in the scenario. The main goal of TomOpt is, thus, to optimise detector parameters (position, efficiency, spatial resolution, span) in relation to a defined cost function, whose main objective is to ensure an optimal prediction of properties of the volume of interest. The optimisation is performed utilising python's PyTorch libraries [190], which ease the computation of the gradient of the whole simulation-optimisation pipeline. In order to compute the gradient descent, it is essential that the effect of the optimisation parameters is differentiable with relation to the loss function. Additional and detailed information about TomOpt optimisation algorithm can be consulted in [111].

The general workflow of TomOpt is shown in figure fig. 6.1. The workflow is composed of seven modules:

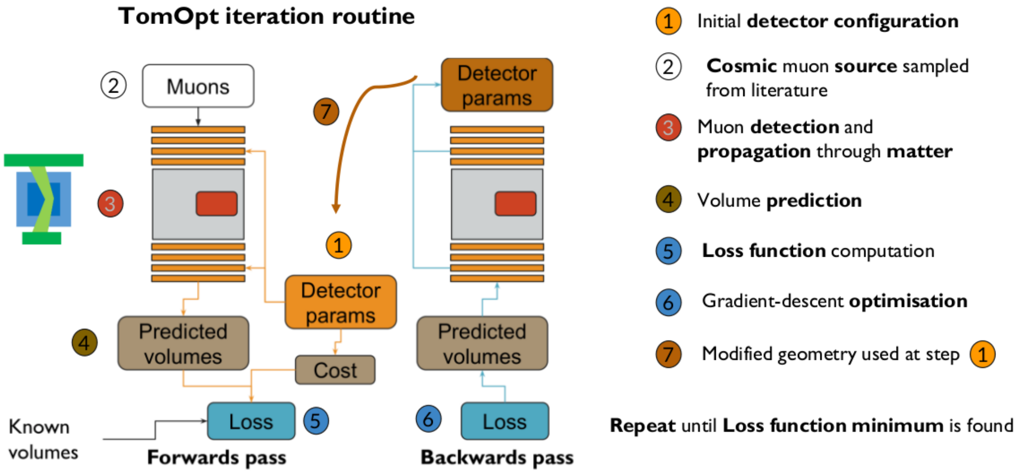

Figure 6.1: Illustration of TomOpt iteration routine and the seven modules composing the software. Figure extracted from [112].

1. Initial detector and volume of interest configuration

In this first step, the user defines the initial detector parameters (x) and the distribution of the materials which are within the volume of interest. In the context of TomOpt, this volume is also named passive volume. The volume is modelled as a group of voxels forming a rectangular parallelepiped. Some of the detector features may remain constant during the optimisation, such as the number of detector layers, and the resolution, while others, like the detector position and size are variable during optimisation.

Regarding the passive volume, several samples with different material distributions can be used within a single optimisation step, or epoch, of the algorithm. This allows to compute a loss averaged over all the samples, reducing bias and reflecting the variability of the scenario. Some parts of the passive volumes can remain as defined in the initial configuration, while the materials of other parts, or voxels, are variable, depending on the application. For example, in the furnace ladle analysed below in this chapter, the voxels forming the walls are always made of the same material, while those in the interior, which represent the filling level, are variable.

2. Cosmic muon source

Cosmic muon generation is based on models extracted from literature [191] [48]. A fixed generation surface is currently used, with flat and squared shape.

In this thesis, the use of a squared dynamic generation surface to set the data taking time during optimisation is proposed, and it has been also provisionally implemented, as a result of the work and research performed together with other TomOpt collaborators. The aim is to maintain constant the data taking time during all the epochs of the optimisation process, regardless of the surface of the detection layers. In this way, detector parameters would be optimised taking into account a specific data taking time. As x, the detector parameters, are dynamic during the optimisation process, the generation surface of each iteration k, should be adapted to them in order to not affect the optimisation. For example, if the surface of the detectors is enlarged, the muon generation surface should be increased too, in order to provide full coverage of muons for all the detection surface. In particular, the generation surface has been set to a coefficient $\alpha > 1$ times the surface of the detectors itself. Initially the value of α has been $\alpha = 1.2$.

The relation between the number of muons and the exposure time t, is given by the muon flux intensity $I^{(k)}$, which could be modified by the user, and the generation surface S.

$$\mu^{(k)} = t \; I^{(k)} \; S^{(k)} \tag{6.1}$$

3. Muon detection and propagation through matter

Muon detection is performed depending on detector resolution, introducing Gaussian errors in the three spatial dimensions. Propagation through matter is based on models extracted from literature [43]. Muon detection and propagation implementation as fully differentiable modules has required to add different features to the code, such as a muon efficiency model depending on the points where muons cross the detectors. It assigns higher efficiencies to muons crossing the detector central part, while muons passing through the edges or outside the detector panels are less determining during the optimisation.

4. Volume prediction

This module handles the inference of properties of the volume of interest. This calculations are based on classical algorithms like POCA. Maximum Likelihood algorithms as well as deep learning methods are in development and could be a potential upgrade (see section 2.3.4). The standard approach of TomOpt is to infer the radiation length voxel-wise distribution within the volume of interest using the POCA algorithm. After this first step, a second stage of task-specific inference to get the final goal of the muography is also considered. In this thesis, an alternative method of direct inference is proposed. The method is also based on the calculation of the points of closest approach of the muons, but in a way that only the parameter of interest, the level of the melted mineral, is estimated. More information is given in the following sections.

5. Loss function computation

The loss function calculation is composed of two main factors that depend on detector parameters, x, which can be named as error, $E(x)$, and cost, $C(x)$. The error is related to the inference predictions, and it is computed as a function of the difference between the predicted value of the parameter of interest, and the simulated truth. On the other hand, the cost represents both financial cost of detection panels, $C_f(x)$, and other technical constraints $C_t(x)$, such as the power consumption. The limitations to define all these parameters accurately within a loss function should be also taken into account. For example, different detection technologies would probably require specific loss functions. In addition, the loss function calculation is application dependent, and it has to be performed with analytic and differentiable functions that allow gradient descent optimisation.

$$\mathcal{L}(x) = f(E(x), C(x)) = f(E(x), C_f(x), C_t(x)) \tag{6.2}$$

For the performance component $E(x)$, TomOpt uses the mean squared error (MSE) of the X_0 predictions of the voxels of which the passive volume is composed, and a cost $C(x)$ depending on the detection surface. The proportion of the two mentioned factors is also crucial for a balanced optimisation of the muography scenario. In this thesis, analyses are made about the performance component of the loss function, which are detailed in section 6.4.

6. Gradient-descent optimisation

The detector parameters are updated at each iteration according to a gradient descent scheme:

$$x^{(k+1)} = x^{(k)} - \eta_k \ \nabla_x \ \mathcal{L}(x^{(k)}) \tag{6.3}$$

where k represents the optimisation iteration, η_k is the step size of iteration k, which can be set in advance or adapted in each step, and $\nabla_x \mathcal{L}$ is the gradient of the Loss function with respect to the detector parameters x at iteration k. The minimisation of the loss function continues until a minimum is found.

6.2 Ladle furnace simulation scenarios

A simplified description of a generic industrial furnace ladle can be found in [192]. Furnace ladles are structures used to transport melted metal produced in an industrial plant. A typical example of the part of the manufacturing process which involves the use of the ladle could be described in a general way as follows: firstly the metal is melted in a furnace, then it is transported with a furnace ladle, and finally it is poured into moulds to create metal parts with a predefined shape. These parts can be post-processed later, in order to get the final product.

In this process, the amount of melted metal inside the furnace is a key parameter. The lack of metal in the ladle can result in moulds that are not completely filled. Therefore, they may not be used to produce the final product correctly. On the other hand, an excessive charge of metal in the ladle leaves remnants and scraps, causing problems and losses in the manufacturing process. It has to be mentioned that in the top of the melted metal inside the ladle, there is a lighter layer of slag produced in the melting process itself. This layer, prevents the use of optical methods to determine the liquid metal level. The resolution needed by the industry to optimise the manufacturing process is of the order of a few centimetres, although it depends on the distinctive features of each case.

For the current analysis in the TomOpt framework, a rectangular furnace ladle is considered, filled with liquid steel as shown in figure fig. 6.2. The yellow volume corresponds to the ladle walls, made of solid steel, the green represents the maximum filling-level, which could be only liquid steel or liquid steel with slag, and the blue is the remaining void volume over the melted materials. The definition of materials is detailed in table 6.1.

Muon detectors are assumed to be located on top and below the laddle furnace. The number of panels of each detector is constant (3 per trajectory detector), but the separation between the panels, and the horizontal positions of the detectors have been varied during the analyses.

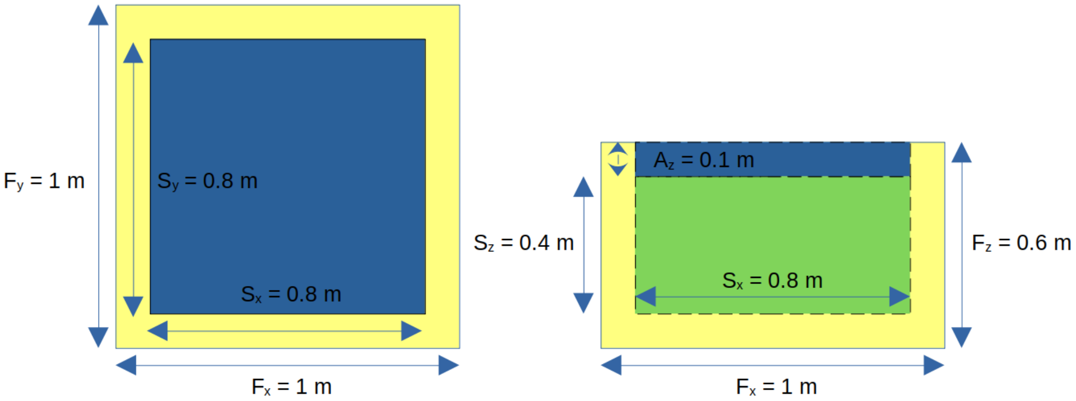

Figure 6.2: Top view (left), and front view (right) of the rectangular furnace ladle simulated in TomOpt. It is composed of walls (yellow), liquid steel (green), and the void volume over the liquid steel (blue).

Material	Density, d $[g/cm_2]$	Radiation length, X_0 $[cm]$	Composition
Solid steel	7.818	1.782	Fe (99%), C (1%)
Liquid steel	7.000	1.991	Fe (99%), C (1%)
Slag	2.700	8.211	CaO (53.5%), Al_2O_3 (33.5%)
Air	0.001205	30390	N_2 (78%), O_2 (20%)

Table 6.1: Density, radiation length and composition of the simulated furnace ladle materials.

6.3 Estimation of the fill level

The volume prediction module of the TomOpt software has been modified for this problem to include a simplified algorithm that focuses on the determination of the level of melted mineral inside the ladle. Instead of making a full reconstruction voxel by voxel, this algorithm estimates just one quantity indicating the position of the interface between the melted mineral and the slag.

This method uses the points of closest approach of the muons. For a given block of steel, the vertical coordinate of the POCA points is distributed around the centre of mass of the block. This fact has been extensively crosschecked using simulated data. Figure 6.3 (left) shows the distribution of the POCA points for a ladle furnace filled with steel up to 0.4 meters. The lower wall of the ladle starts at 0.2 meters and ends at 0.3 meters. Since the density of the solid steel of the bottom wall is very similar to the density of the liquid steel, both form approximately a unique steel block, whose centre of mass is ocated at 0.3 meters. Figure 6.3 (right), shows the distribution of the vertical coordinate of the POCA points for this scenario. It can be seen that the distribution is centred close to the expected position, 0.3 m.

The next model assumption has to do with the influence of the layer of slag. Since its density is very small compared with the density of steel, and usually the thickness of the layer is much smaller than the height of the liquid steel (typically of the order of 5%), its effect on the method is considered to be negligible. Under these circumstances, the level of the steel can ideally be obtained from the following equation:

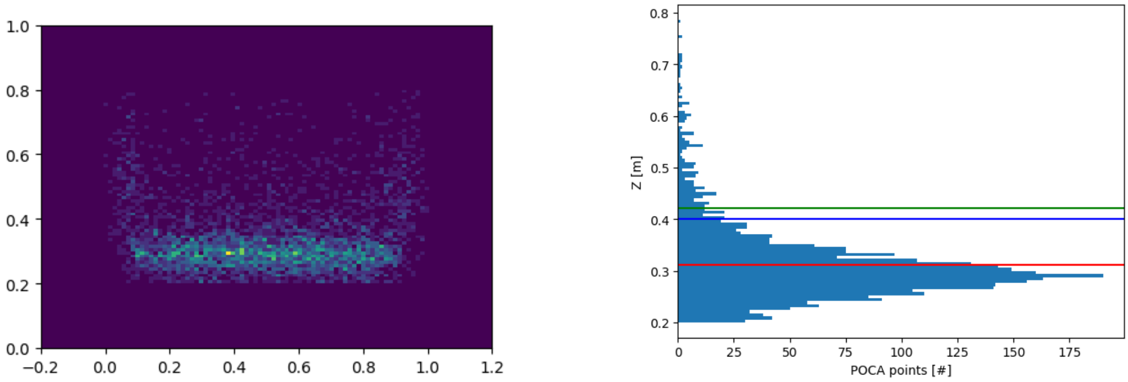

Figure 6.3: TomOpt muography of the ladle furnace filled with steel up to 0.4 m. The bottom wall of the furnace goes from 0.2 to 0.3 m in Z axis. On the left, the front view of POCA reconstruction. On the right, POCA distribution in the vertical axis and filling level inference representation: $\overline{Z_{POCA}}$ (red), true steel level (blue), and estimation of the steel level (green).

$$L = Z_{bottom} + 2\,(\hat{Z}_{POCA} - Z_{bottom}) \tag{6.4}$$

Where Z_{bottom} is the position of the bottom surface of the lower wall of the ladle, and $\hat{Z}_{POCA}$ the estimator of the centre of the POCA distribution in the vertical axis. This method apparently provides a simple and fast procedure to estimate the level of the liquid steel without having to divide the volume of interest in voxels, and favouring the execution of the TomOpt optimisation algorithm.

6.3.1 Validation of the method assumptions

The assumptions made by the algorithm have been validated using simulated data. First of all, in order to check that the centre of the liquid steel can be extracted from the centre of vertical coordinate distribution of the POCA points, several simulations have been computed. Data of different scenarios with varying levels of liquid steel and no slag layer have been generated. The liquid steel level has been determined using eq. (6.4) and it has been confronted with the true simulated level.

A squared 2×2 m^2 generation surface has been used, with 20000 muons generated in each simulation. Assuming the approximation in eq. (2.5) for the muon flux intensity, the data taking has been equivalent to half a minute. Considering a typical flux generated with CRY simulations, it would be roughly of 0.73 minutes. In this set of simulations, the slag layer has been removed, since as explained above, normally its thickness is around a 5% of the thickness of the steel, and it can be deprecated without decisively affecting the results. In total, 1200 simulations have been part of this second study, 100 per scenario. The simulated 12 scenarios are the result of combining small gap, not centred, and big gap detector panel configurations, two simulated detection surfaces, and two simulated detector resolutions: $\sigma_{hits} = 0.01$ mm, and $\sigma_{hits} = 1$ mm (see table 6.2).

The figure 6.4a shows the method predictions and the ground truth for a spatial resolution of 0.01

		Panel surface [m^2]	
		0.49	0.81
	Detector panels, Z [m]	Detected flux [μ]	
Small gap	0.90, 0.85, 0.80, 0.20, 0.15, 0.10	2737	5340
Not centred	0.90, 0.85, 0.80, 0.20, 0.10, 0.00	2537	4993
Big gap	1.00, 0.90, 0.80, 0.20, 0.10, 0.00	2390	4745

Table 6.2: Positions of the horizontal detection panels in Z axis and flux crossing the detectors for the different panel configurations, the two simulated detection surfaces, and $\sigma_{hits} = 1mm$ resolution.

mm, a detector size of 0.81 m^2, and a big gap detector configuration. Detector configurations are specified in table 6.2. As it can be observed, the method works fairly well for a detector with an almost perfect spatial resolution. On the other hand, fig. 6.5b shows the method predictions and the ground truth for a realistic spatial resolution of 1 mm. In this case, although biased, the method is still accurate for high steel levels. However, it undergoes a progressive error increment when decreasing the steel level.

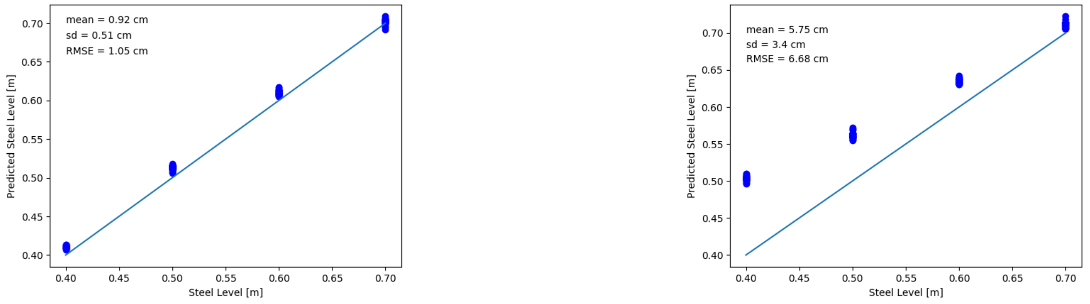

(a) $\sigma_{hits} = 0.01$ mm resolution, 0.81 m^2, big gap.

(b) $\sigma_{hits} = 1$ mm resolution, 0.81 m^2, big gap.

Figure 6.4: Steel level predictions and ground truth for a detector with almost perfect spatial resolution (left) and with realistic spatial resolution (right).

These figures suggest that even if the method is very precise for a detector with extremely high resolution, changes on detector characteristics and configuration have a strong impact on the predictions. On the other hand, it can be extracted from the figures that this estimator has a very low variance and a high repeatability, which opens the ground to perform a calibration in order to get an adaptable estimator.

Effect of the slag layer

An additional simulation study has been performed in order to analyse the effect of the slag layer on the top of the liquid steel. For that purpose, the estimations of the steel level have been assessed, comparing cases where slag is not present, with scenarios containing slag. The liquid steel level has been determined in the same way as in the previous study, using eq. (6.4).

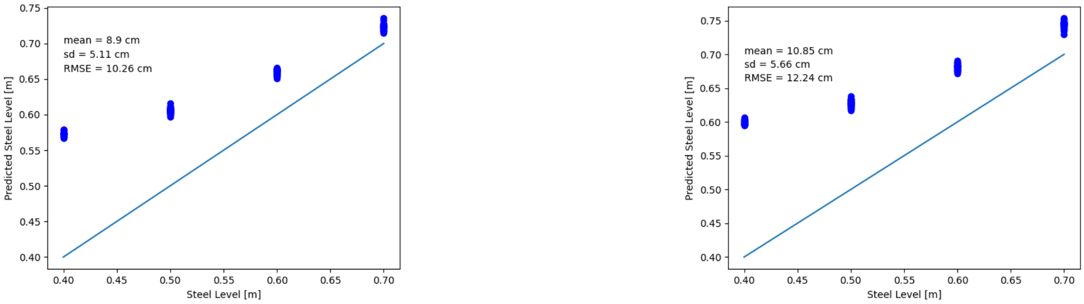

(a) σ_{hits} = 0.01 mm resolution, 0.81 m², small gap.

(b) σ_{hits} = 1 mm resolution, 0.81 m², not centered.

Figure 6.5: Steel level predictions and ground truth for a realistic detector with different detector geometry configurations: small gap (left) and not centered (right).

In fig. 6.6, the results of the inference method for TomOpt simulations of 10000 muons crossing the volume of interest are illustrated in a confusion matrix format. On the left, the results of 100 simulations with variable slag layer on the top of the steel (0, 0.1, 0.2, 0.3 m). On the right, the results of 100 simulations without slag. It should be noted that it is not realistic the presence of such thick slag layers, that in some of the simulated cases are even thicker that the steel layer itself. Usually, the slag layer thickness is around the 5% of the steel layer thickness, having little influence in muon scattering due also to its lighter materials (table 6.1). The steel layer thickness, or in other words, the steel level, is usually close to the top of the furnace, as it is desired to transport the maximum amount of liquid metal with the ladle. Therefore, in this TomOpt ladle scenario, a typical and representative case could be a ladle filled up to 0.70 m with a 0.50 m thick layer of steel, and with a thin layer of slag on the top, of approximately 0.025 m. Small variations on the steel level, of the order of a few centimetres, are the kind of disturbances needed to be measured in the industry in order to improve the manufacturing process efficiency. However, in this initial development phase of TomOpt the inference method has been tested for a wider range of steel levels, from 0.1 m (ladle filled from 0.30 m up to 0.40 m) to 0.4 m (ladle filled from 0.30 m up to 0.70 m) .

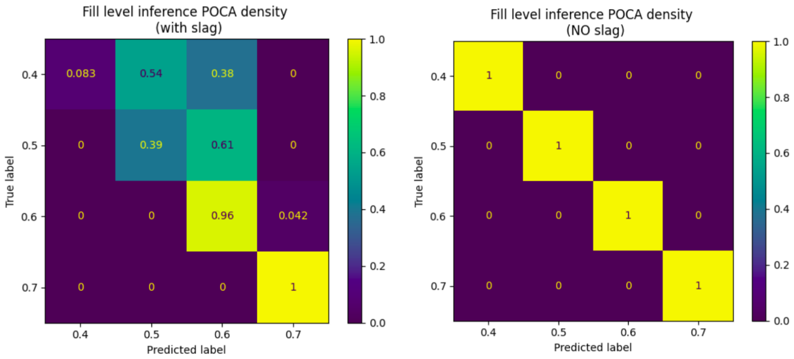

Figure 6.6: Results of the inference method for simulations of 10000 muons crossing the volume of interest. The horizontal axis, the true steel level is represented and in the vertical axis, Y, the predicted level. On the left, the results of 100 simulations with variable slag layer on the top of the steel (0, 0.1, 0.2, 0.3 m). On the right, the results of 100 simulations without slag.

6.3.2 Calibration of the estimator

According to what has been mentioned in the previous subsection, a calibration of the estimator has been performed by fitting a second order polynomial. The results can be seen for the four scenarios in fig. 6.7.

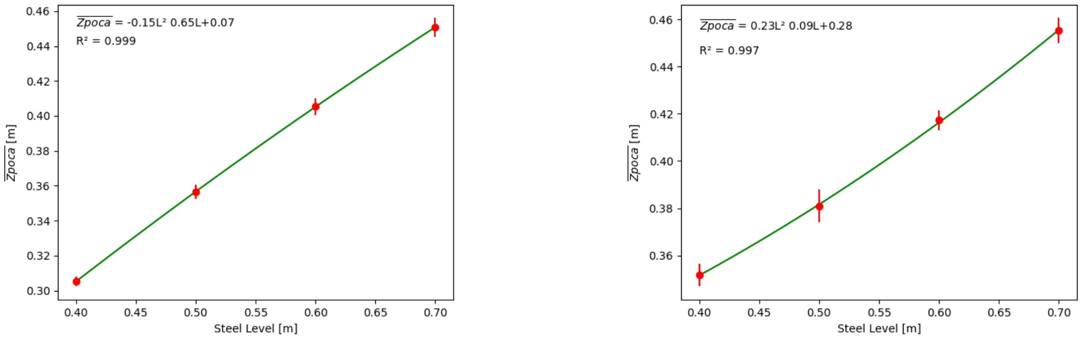

(a) σ_{hits} = 0.01 mm resolution, 0.81 m², big gap.

(b) σ_{hits} = 1 mm resolution, 0.81 m², big gap.

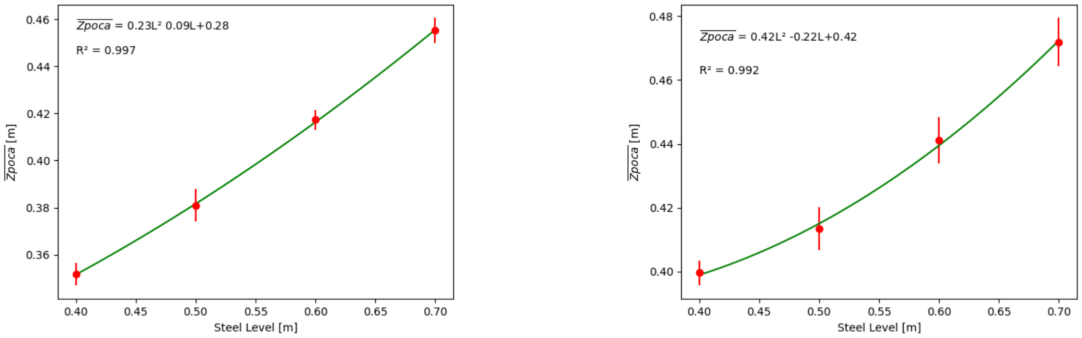

(c) σ_{hits} = 1 mm resolution, 0.81 m², small gap.

(d) σ_{hits} = 1 mm resolution, 0.81 m², not centred.

Figure 6.7: Calibration curves for the predictors obtained in four different scenarios. Fitted parameters, and error metrics are specified. Error bars correspond to 3σ intervals.

The fits have been performed using only a 70% of the simulations and the remaining 30% have been performed to estimate the corresponding uncertainties. The standard deviations for the 4 scenarios are respectively 4 mm, 6 mm, 9 mm and 12 mm. These values represent a high accuracy in terms of the specification of the problem. Knowing the position of the steel level with a couple cm precision can provide very useful information to the industry for the process efficiency optimisation.

This estimator, including its calibration, has been introduced within the TomOpt software in such a way that, at every iteration and considering different geometries, a fit is performed to produce it. The estimator is later used to make the final prediction and the minimisation. It should be mentioned that TomOpt can help finding more optimal detector configurations which could provide even better muography results.

6.4 Evaluation of the estimator in the TomOpt loss function

In this section, the calibrated estimator previously described has been analysed for different detection surfaces and detector configurations. The evolution of the RMSE of the predictions is assessed. As explained in section 6.1, the loss function is composed of two main terms, the error, $E(x)$, and the cost, $C(x)$. Here, the error component is studied, which is usually computed as a function of the difference between the predicted value of the parameter of interest, and the simulated truth.

For that purpose, simulation data with different detector configurations (see table 6.2) have been utilised. To get the filling level predictions, the method based on quadratic function fitting explained in the previous section 6.3.2 has been used. The results are shown in fig. 6.8. As seen in the graph on the left, the RMSE of the predictions is reduced sharply roughly until 1 m^2 detection surface, for both training and test datasets. However, further increment of detection surface does not seem productive for this application and inference method. Training data correspond to the samples used to fit the model, while test data are independent samples. Note that, as expected, the test error is higher. The graph on the right shows the training RMSE of the models fitted in section 6.3.2 with a panel span of 0.9, as well as an equivalent analysis performed for a panel span of 0.7. The data illustrates how detector configurations considered more optimal in terms of symmetry of the panels, and angular and hit resolution have better performance.

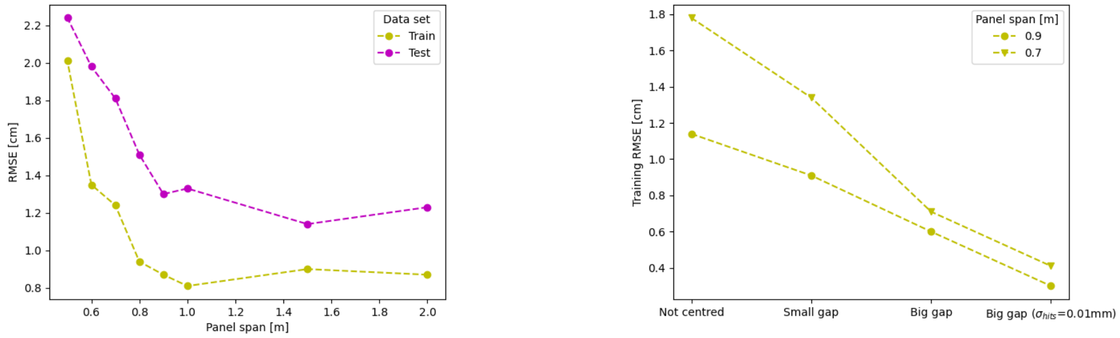

Figure 6.8: Evolution of train and test RMSE for “big gap” configuration depending on panel span (left). Evolution of train RMSE for different detector configurations and two panel spans (right).

It should also be mentioned that the data taking time simulated to obtain the data of the left graph of fig. 6.8 have been approximately three times shorter compared to the simulations analysed in section 6.3.2. The results of the right graph of the figure fig. 6.8 correspond with the larger data taking time considered in the aforementioned section 6.3.2. In that previous section, a reference of the expected errors has been set. The defined expectations correspond with the data on the right graph, but due to the shorter data taking time simulated, the errors shown in the left graph of this analysis are higher.

The RMSE values could be used within TomOpt as the error loss function component $E(x)$, providing the minimisation gradients and guiding the optimisation depending on the quality of the predictions of the fitted model.

6.5 Conclusions

The problem of the ladle furnace has been considered as benchmark case to test the capabilities of the TomOpt optimization software. The proposed filling level inference technique based on the POCA points has been used within the TomOpt software as an estimator of the fill level. The simplicity and generalist nature of the proposed inference method ensure an adequate performance in a wide variety of cases. This has been demonstrated in different simulation analyses, where inference values behave as expected. However, the proposed approach, do not involve inferring characteristics of the materials, such as the X_0, which is a more complex task. To optimise muography cases using a voxel-wise inference of material X_0 is other of the TomOpt objectives for the near future. In any case, the estimation technique based on POCA point densities has demonstrated to be useful for industrial cases like the one studied in this work, the steel furnace ladle. The ability to infer the steel level with a low number of muons is also beneficial, since it allows to run optimisation with lower computing requirements, a factor that make easier the first applications of TomOpt in this initial phase. Note that when running optimisation, the scenario is dynamic, and the detectors undergone small changes in each iteration that have to be simulated in order to get the cost, calculate the gradients, and continue optimising the scenario to the next iteration. This process is usually a demanding task in terms of computing.

To sum up, in this work a scattering muography estimation technique useful for differential programming is proposed. The method is based on POCA point spatial distributions, and it can be used to optimise a scenario where the objective is to estimate the height of a volume filled with a specific material. It is a simple, effective and efficient procedure, adequate for the differential optimisation of industrial muography scenarios. It is already being tested, and its implementation has contributed to the last results published by the collaboration.

Chapter 7

Conclusions

Muon tomography, usually referred to in the field as muography, is a technique capable of determining the density distribution of matter using the data provided by the muons passing through it. It can be applied by means of muon attenuation, but this thesis focuses on scattering muography. This modality makes use of the multiple scattering of muons to infer the properties of the material traversed by measuring their deflections. Therefore, compared to absorption, scattering muography is suitable for applications on targets with more limited dimensions and requiring higher resolution.

In the application of muon tomography, a thorough understanding of the functioning of the muon detectors used is indispensable. In addition, their correct calibration and tuning are of utmost importance. In this thesis, the design of detectors based on Multi-Wire Proportional Chambers (MWPCs), specifically those developed and built by Muon Systems, is analysed. The procedure used for event reconstruction is also explained, and the efficiencies and resolution of the detectors are studied, among other aspects. Their efficiencies have been characterised by means of several experiments, in which it has been observed that under optimum conditions the efficiency at camera level is higher than 95%. In addition, it is worth mentioning the analyses performed about intelligent event reconstruction algorithms, and chamber alignment, which can have a direct impact on the reconstruction quality of muon trajectories.

Since the introduction of muon radiography in the early 1950s, both muon absorption and scattering have been used to map the density of structures in archaeological sites and more modern buildings of civilian use. Muography is a valid technique for non-destructive inspection of the condition of buildings and structures, and it can work better than other technologies in certain environments and applications. In this thesis, a feasibility study of the detection and imaging of cracks in scenarios made of concrete cylinders is presented. Measuring the multiple scattering of muons and applying an original algorithm adapted to the problem, density maps have been reconstructed. By means of this reconstruction technique, cracks of 1 and 2 centimetres have been detected and located in concrete samples of 15 centimetres in diameter. These defects are equivalent to the absence of about 0.5 kg of concrete. To perform these experiments, the detection hardware described above has been used, thus evaluating the limits of the technique and the performance of the hardware in a demanding situation, with subtle detection objectives. The developed research has been published in a conference paper, whose presentation was also made.

The research performed on the estimation of the *snow water equivalent* (SWE) has been focused on two distinct objectives. The first corresponds to a detailed analysis of numerical simulations, while the second consisted of assessing the capabilities of the hardware to measure the *snow water equivalent* of artificial snow samples. The results obtained by simulating a whole year of snowpack evolution have yielded average errors of around one centimetre. On the other hand, the measurements made in the laboratory are in agreement with the expected values and are compatible with the models built in simulation. This work has been the first proof-of-concept of the use of scattering muography in the estimation of the *snow water equivalent*. The research has served to demonstrate that this technique provides relevant information and could be used to monitor the evolution of the snowpack. Mention should also be made of the potential of this type of muography to estimate the density distribution of the inner layers of the snowpack, being able to identify voids or weak layers. This information would be of great interest in the area and could help to prevent avalanches and contribute to the knowledge of the internal structure of the snowpack. It should be noted that work related to this research has been presented at an European geoscience conference, and also recently published in a high-impact journal.

Without forgetting the two studies in the appendices on cargo detection and material characterisation, the last application thoroughly studied in this thesis has been the estimation of the filling level of liquid steel in a ladle furnace. This type of industrial furnace is actually a large container used to transport melted metal from one part of a factory to another. The quantification of its filling level can contribute to the optimisation of the manufacturing process, avoiding for example an incomplete filling of moulds, or leftovers that could cause problems or loss of material. This study has been carried out in the context of an international collaboration which works on the development of a software capable of optimising the configuration and geometry of detectors in muon tomography applications (TomOpt). Using this software, the problem has been simulated and analysed, resulting in the implementation of a method to estimate the liquid steel filling level. The proposed algorithm has been integrated into the TomOpt software thanks to the collaboration of other members of the project. The results obtained are in the process of being published as a journal article, and a previous version has already been published in a repository.

To conclude, it is worth mentioning that this work has had a significant impact on the company Muon Systems. Intensive research has been carried out, including tasks dedicated to the characterisation and fine-tuning of the hardware, as well as the implementation of reconstruction algorithms. As a consequence of these research lines, muography techniques with novel approaches have been developed, which in many cases have been put into production in different industrial projects of the company. In addition, new applications of muon tomography have been explored, such as the monitoring of the *snow water equivalent*. Muon tomography is an emerging technology that will undoubtedly become a standard in the future. This thesis aims to contribute a small step towards the realisation of that path.

Chapter 8

Conclusiones

La tomografía muónica, usualmente conocida en el campo como muografía (muography, en inglés), es una técnica capaz de determinar la distribución de la densidad de la materia, valiéndose de los datos aportados por los muones que la atraviesan. Es posible aplicarla por medio de la atenuación de los muones, pero esta tesis está enfocada en la muografía de scattering. Esta modalidad hace uso del scattering múltiple que sufren los muones para, mediante la medición de sus desviaciones, inferir las propiedades del material atravesado. Por ello, y en comparación con la modalidad de absorción, la muografía de scattering es idónea en aplicaciones sobre objetivos de dimensiones más limitadas y que requieren una mayor resolución.

En la aplicación de la tomografía muónica resulta indispensable la comprensión profunda del funcionamiento de los detectores de muones utilizados. Además, su correcta calibración y puesta a punto son factores de suma importancia. En esta tesis se analiza el diseño de detectores basados en cámaras multi-hilo (MWPCs, por sus siglas en inglés), en concreto los desarrollados y construidos por la empresa Muon Systems. Se explica también el procedimiento utilizado para la reconstrucción de eventos y se estudian las eficiencias y resolución de los detectores, entre otros aspectos. Sus eficiencias se han caracterizado mediante varios experimentos, en los cuales se ha observado que en condiciones óptimas la eficiencia a nivel de cámara es superior al 95%. Además, cabe mencionar los análisis realizados en cuanto a algoritmos inteligentes de reconstrucción de eventos, y alineamiento de las cámaras, los cuales pueden repercutir directamente en la calidad de reconstrucción de las trayectorias de muones.

Desde la introducción de la radiografía de muones a principios de la década de 1950, tanto la absorción como la desviación de los muones se han utilizado para mapear la densidad de estructuras en yacimientos arqueológicos y edificios más modernos de uso civil. Se podría decir que la muografía es una técnica válida para explorar de forma no destructiva el estado de edificios y estructuras y que puede funcionar mejor que otras tecnologías en determinados entornos y aplicaciones. En esta tesis, se presenta un estudio de viabilidad de la detección y obtención de imágenes de grietas en escenarios compuestos por cilindros de hormigón. Utilizando el scattering múltiple de los muones, se han reconstruido mapas de densidad mediante un original algoritmo adaptado al problema. Esta reconstrucción ha servido para detectar y localizar grietas de 1 y 2 centímetros en probetas de hormigón de 15 centímetros de diámetro. Dichos defectos, equivalen a la ausencia de en torno a 0,5 kg de hormigón. Para realizar estos experimentos se ha utilizado el hardware de detección anteriormente descrito, evaluando así en una situación exigente, con objetivos de detección sutiles, los límites de la técnica y el funcionamiento del hardware. La investigación realizada, ha sido redactada en un artículo de congreso, cuya presentación fue también llevada a cabo.

La investigación realizada sobre la estimación del equivalente de agua de la nieve se ha centrado en dos objetivos diferenciados. El primero se corresponde con un análisis detallado de simulaciones numéricas, mientras que el segundo ha consistido en evaluar las capacidades del hardware para medir la equivalente de agua de muestras de nieve artificial. Los resultados obtenidos mediante la simulación de un año completo de evolución del manto han arrojado errores promedio de en torno al centímetro. Por otro lado, las medidas realizadas en el laboratorio se corresponden con los valores esperados y son compatibles con los modelos construidos en simulación. Este trabajo ha sido la primera prueba de concepto del uso de la muografía de scattering en la estimación del equivalente de agua de la nieve. La investigación ha servido para demostrar que dicha técnica aporta información relevante y podría ser utilizada para monitorizar la evolución del manto. También debe ser mencionado el potencial que posee este tipo de muografía para llegar en un futuro a poder estimar la distribución de la densidad de las capas internas del manto, pudiendo identificar huecos o capas débiles. Esta información sería de gran interés en el área y podría ayudar a prevenir avalanchas y contribuir al conocimiento de la estructura interna del manto de nieve. Cabe señalar, que los trabajos relacionados con esta investigación han sido presentados en una conferencia europea de geociencias, y también publicados recientemente en una revista de alto impacto.

Sin olvidar los dos estudios de los apéndices sobre detección de mercancías y caracterización de materiales, la última aplicación estudiada en profundidad en esta tesis ha sido la estimación del nivel de llenado de acero líquido en un horno cuchara. Este tipo de horno industrial, en realidad es un gran recipiente con el que se transportan minerales en fusión de un lugar a otro de una fábrica. La cuantificación de su nivel de llenado permite optimizar el proceso de fabricación, evitando por ejemplo un incompleto llenado de moldes, o restos que puedan causar problemas o suponer la pérdida del material. Este estudio ha sido realizado en el contexto de una colaboración internacional que trabaja en el desarrollo de un software capaz de optimizar la configuración y geometría de los detectores en aplicaciones de tomografía muónica (TomOpt). Usando este software, se ha simulado y analizado el problema, resultando en la implementación de un método de estimación del nivel de llenado de acero líquido. El método propuesto ha sido integrado dentro del algoritmo TomOpt gracias a la colaboración de otros miembros del proyecto. Los resultados obtenidos están en proceso de publicación como artículo de revista, y ya existe una versión previa publicada en un repositorio.

Para concluir, cabe mencionar que este trabajo ha tenido un impacto destacable en la empresa Muon Systems. Se ha llevado a cabo un intenso desarrollo de diversas investigaciones, incluyendo tareas dedicadas a la caracterización y puesta a punto del hardware, así como a la implementación de algoritmos de reconstrucción. Como consecuencia de dichas lineas de investigación, técnicas de muografía con novedosos enfoques han sido desarrolladas, las cuales han pasado a estar, en muchos casos, en producción dentro de diferentes proyectos industriales de la empresa. Adicionalmente, nuevas aplicaciones de la tomografía muónica han sido exploradas, como por ejemplo la monitorización de la cantidad de nieve en el manto. La tomografía muónica es una tecnología emergente que sin duda será un estándar en el futuro. Con esta tesis se pretende contribuir con un pequeño paso a la realización de ese camino.

Appendix A

Deviations of muons retrieved by means of Smart Tracking techniques

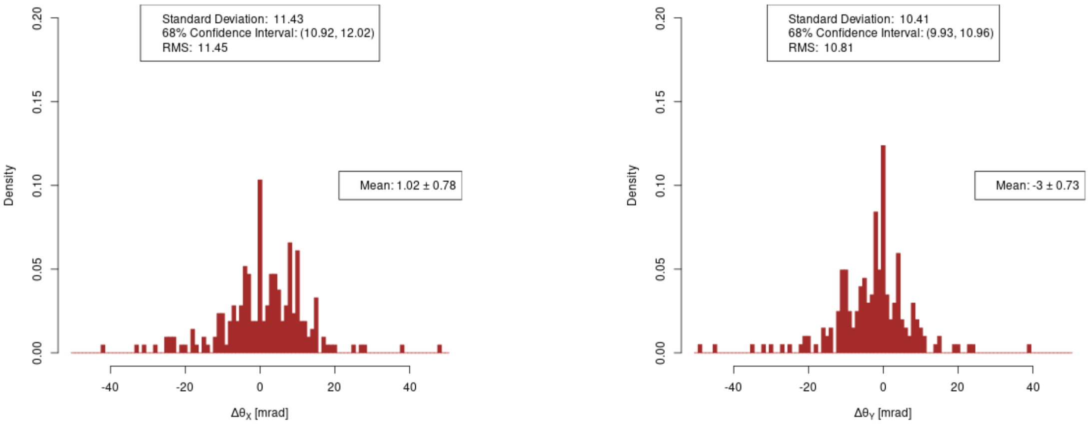

Figure A.1: Deviations ($< 50\ mrad$) of retrieved events with void data in at least one of the detection layers. None of them has simultaneous multiple wire activation above 4 wires.

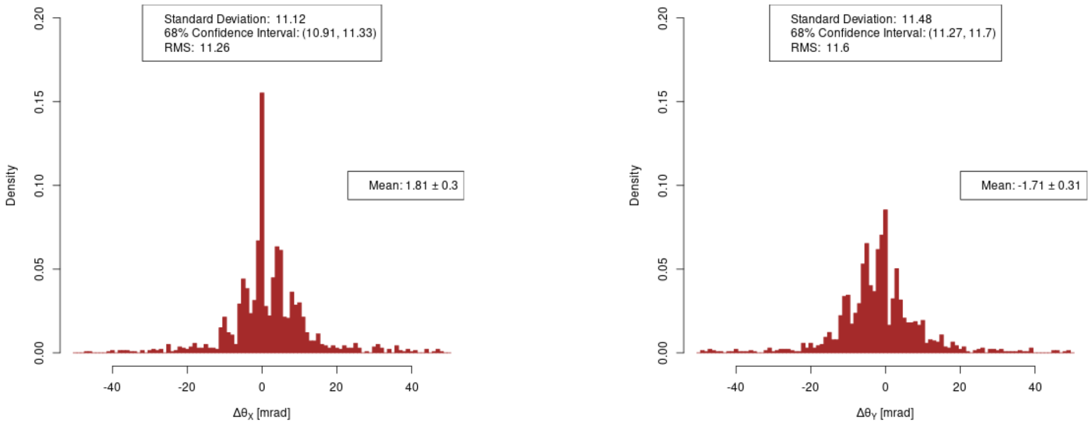

Figure A.2: Deviations (< 50 $mrad$) of retrieved events that initially had not contiguous wires in at least one of the detection layers. None of them has simultaneous multiple wire activation above 4 wires.

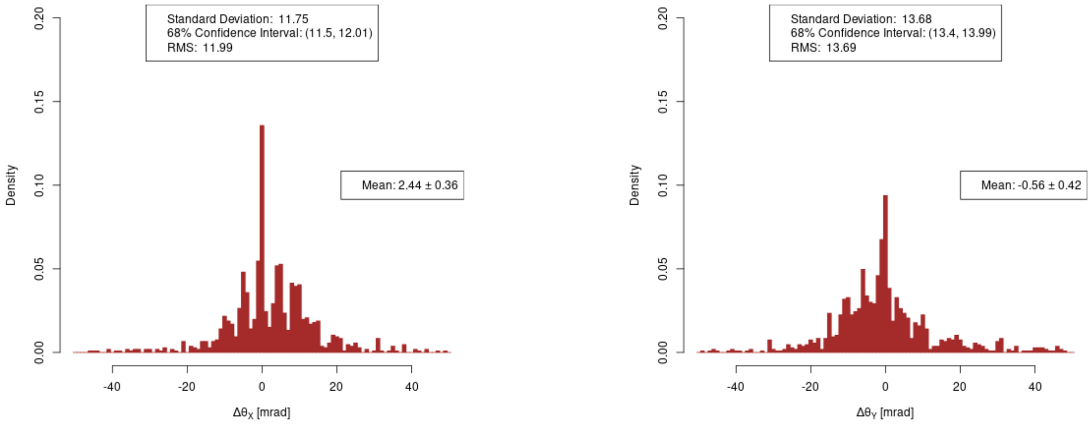

Figure A.3: Deviations (< 50 $mrad$) of retrieved events that initially had excessive wire activation in at least one of the detection layers. None of them has simultaneous multiple wire activation above 4 wires.

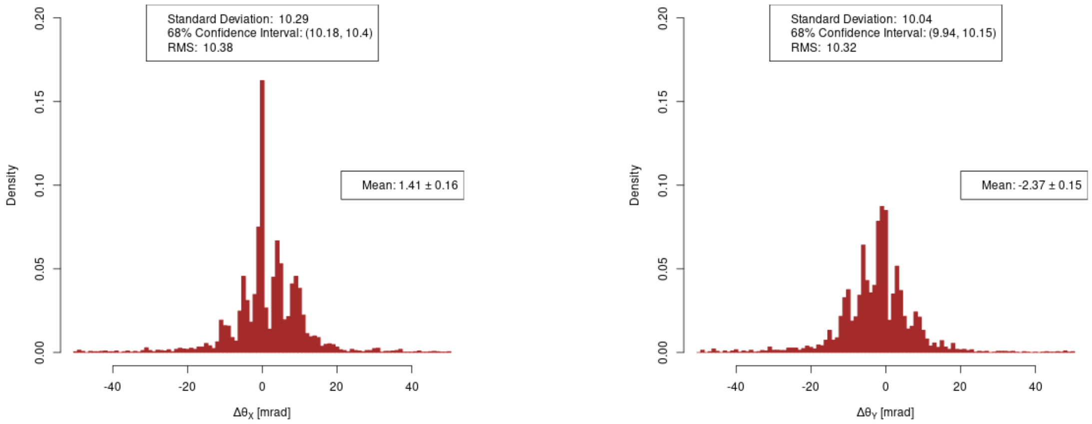

(a) Initial.

(b) Initial.

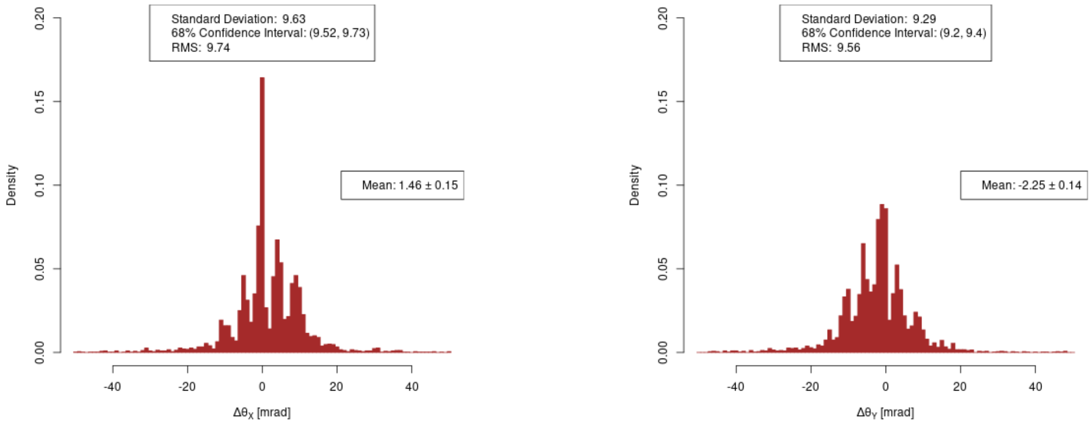

(c) Noise removal.

(d) Noise removal.

Figure A.4: Deviations ($< 50\ mrad$) of events before and after noise removal based on trajectory goodness of fit to straight lines.

Appendix B

Material characterisation using Neural Network models

During this PhD, the use of neural networks (NN) models for material characterisation has been explored too. The quantiles of muon scattering angles have been used as inputs of the applied NNs, as specified in section 2.3.4. The NNs have been trained with both simulation and laboratory samples of the same mass, but composed of several materials, including air, that mixed sum different total X_0. The materials filled different volumes with variable and random spatial distributions within the limits of the detection volume between the detectors. Due to the exponential increase of X_0 that elements and materials approximately follow when density is linearly decreased (see bottom right graph of fig. B.1), columns of the same surface and mass made of different materials contain different number of radiation lengths along their height, or in other words along their thickness (see bottom left graph of fig. B.1). This is also directly expressed by the characteristic radiation length in relation to a unit of mass, which is measured in g/cm^2 (see section 2.2.5). Consequently, the X_0 of the mentioned samples, which have a constant x including air, varied, showing larger values when they were composed of less dense material mixtures. Therefore, as specified by eq. (2.21), and deprecating geometric and other kind of secondary effects, the expected θ_0 for samples of the same mass, but composed of less dense materials, are smaller.

After being trained, the simulation NNs have been tested with simulated unknown samples, showing the ability to estimate the amount of up to three different materials which composed the samples. The estimation error varied depending on the number of training samples, their data taking time, as well as the differences between the X_0 per unit of mass of the materials, and their proportion by weight within the mixture. The total X_0 of the less dense samples, has been of roughly the 88% of the densest samples. Ongoing work is under development in order to understand the level of compatibility between laboratory samples and simulations. Other approaches are also being explored, such as the creation of neural networks with laboratory data.

Through NN training, the performance of classical models derived from eq. (2.21) has been improved, allowing a better material characterisation. The training process also learns the effect that detector configurations and resolution produce in the measurements of muons, removing the bias it usually introduces in traditional models, even if all uncertainties, noise sources, and phenomena are intended to take into account. However, NNs normally require a larger amount of data to be appropriately trained, a fact that limits the application with real world measurement data.

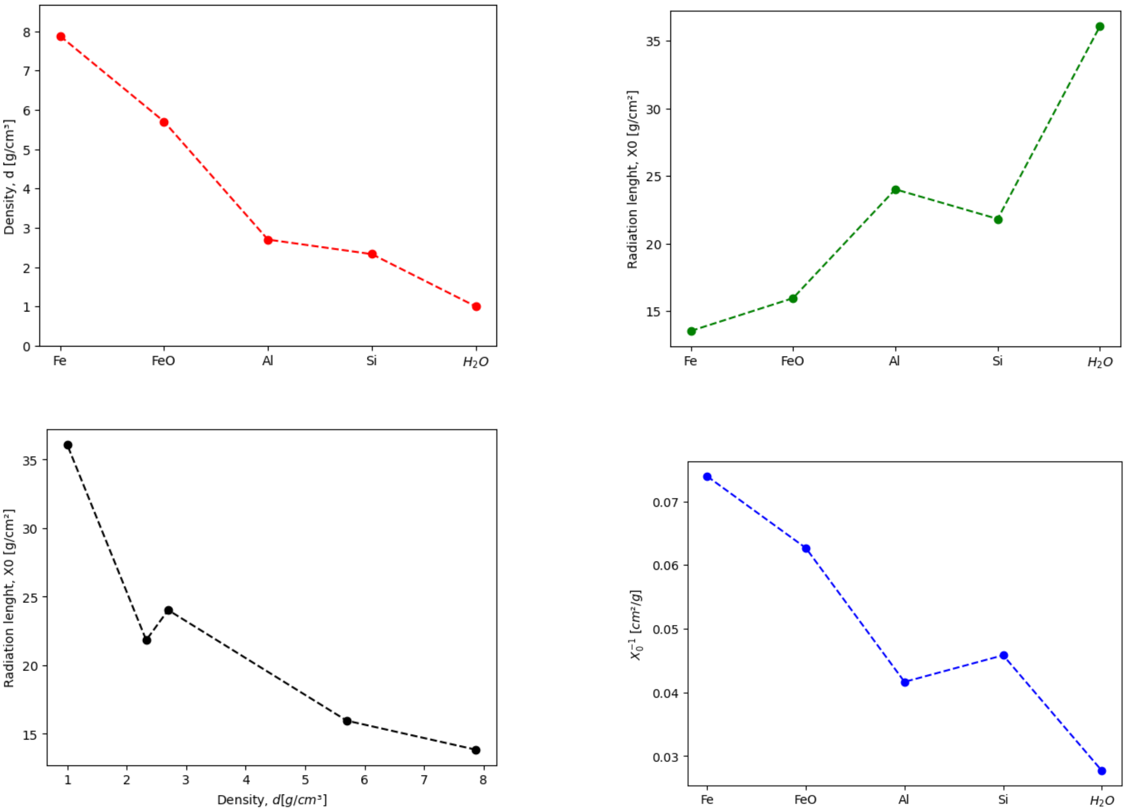

Figure B.1: Analysis of main properties of iron (Fe), ferrous oxide (FeO), aluminium (Al), silicon (Si), and liquid water (H_2O). The thickness x/X_0, is measured in radiation lengths, and corresponds for each material to that of a column of 1 g, with a base of 1 $\mathbf{cm^2}$.

Appendix C

MUON CARGO project: anomaly detection in cargo containers

The MUON CARGO project [193], consists on the development of industrial research, both in hardware, and software areas, in order to implement a detection system able to perform maritime transport container and vehicle inspection using muon scattering tomography. The project is co-financed by Puertos del Estado [194] (public business entity under the Spanish Ministry of Transport, Mobility and Urban Agenda). The collaboration of IFCA (Instituto de Física de Cantabria - Universidad de Cantabria) is also included. The three main activities of MUON CARGO are the work related to software and detection algorithms, manufacturing of a 3x3 m^2 modular detector based on previous designs, and field tests. The final result of the project will be a specialised and intelligent muography scanner prototype, which will be installed in the Port of Santander (see fig. C.1).

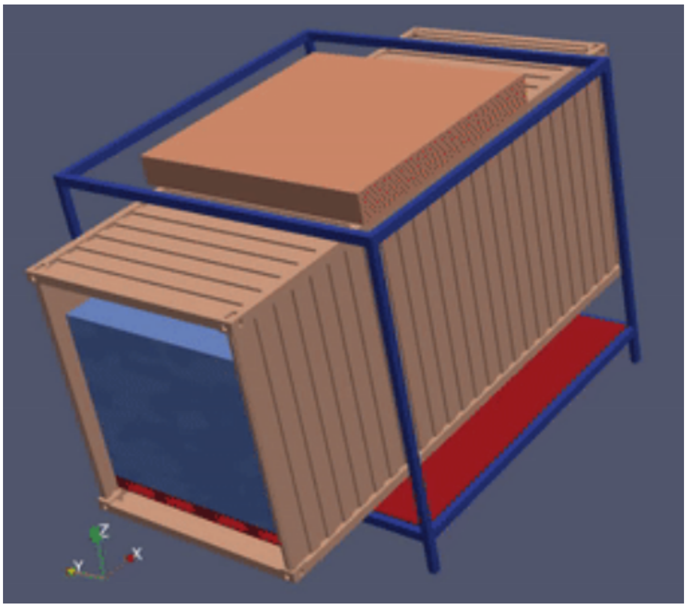

Figure C.1: Sketch of the MUON CARGO 3x3 m^2 scanner prototype.

The software part of the project involves development of AI and scattering muography algorithms, on the basis of previous work [61]. POCA and other muography algorithms will be used to feed autoencoders for anomaly detection. The application of variants of classic MLEM algorithm are also considered (see section 2.3.4). This work is ongoing within the project planning. In addition to muography algorithm outputs, complementary data about the mass of the cargo, declared goods, and other available information will be exploited.

In this thesis, a preliminary analysis of simulation results of the MUON CARGO prototype is presented. POCA imaging algorithm has been applied to simualtions containing several anomalies, differing in their material and location. A simulation scenario has been built in Geant4 [195], consisting of an active detection surface of 268.8 x 268.8 cm^2, in line with that of the MUON CARGO prototype. This surface is covered with 4 Multi Wire Proportional Chambers (MWPCs), i.e, 2D detection grids. Each chamber is able to detect the horizontal coordinates (X, Y) of the points where muons cross it with a precision of 1.15 mm, since the detection wires are placed 4 mm apart from each other (see equation **??**). The vertical coordinate (Z) is given by the chamber position itself.

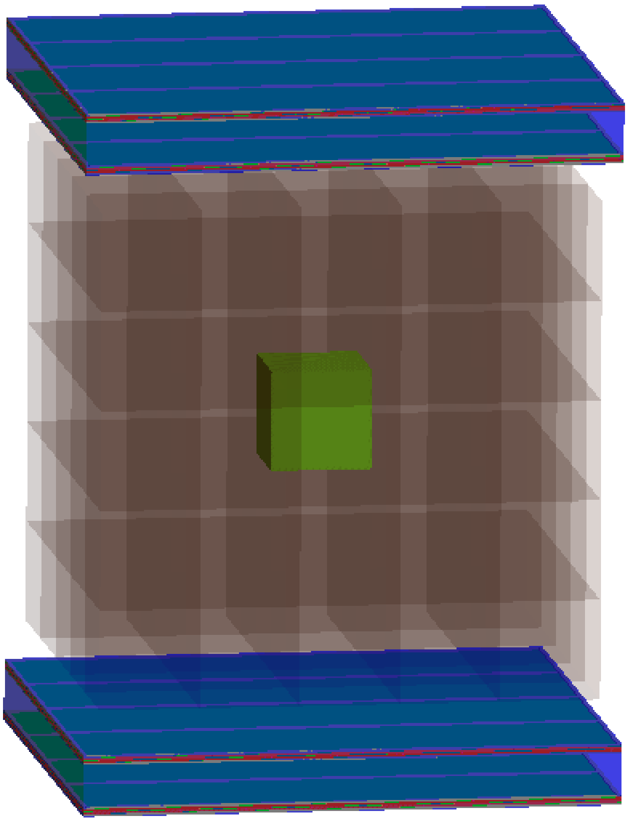

Figure C.2: MUON CARGO prototype simulation (active detection surface of 268.8 x 268.8 cm^2). The volume of the cargo (250 x 250 x 250 cm^3) is composed of 125 voxels (50 x 50 x 50 cm^3). The green voxel contains an anomaly, i.e, a different material.

The volume of the cargo is 250 x 250 x 250 cm^3, and it is composed of 125 voxels of 50 x 50 x 50 cm^3. A unique voxel containing an anomaly (green voxel in fig. C.2) has been simulated, meaning a material with different properties compared to the base material, which is the declared material, or in other words, the material of which the shipment should be composed. All the other voxels are filled with the base material. In this preliminary analysis, POCA reconstructions of 10 minute muographies are shown. In this case, the anomaly is a voxel with guns, which is composed of a mixture of steel and air. The other voxels, are made of the base material, an organic mixture (see table C.1).

Material	Density, d $[g/cm_2]$	Radiation length, X_0 $[cm]$	Composition
Organic	0.100	364.3	Organic (10%), Air (90%)
Guns	3.925	3.533	Steel (50%), Air (50%)

Table C.1: Density, radiation lenght and composition of the simulated cargo materials.

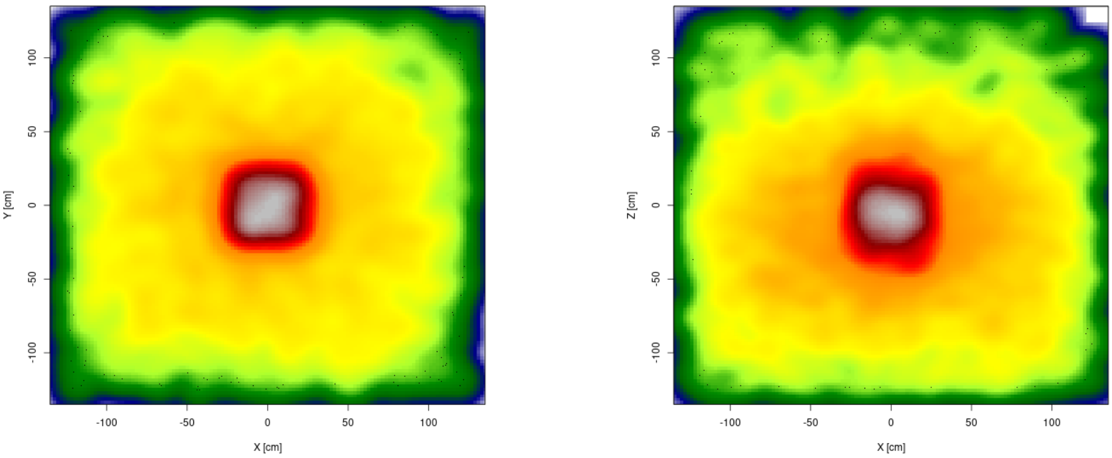

(a) Top view.

(b) Front view.

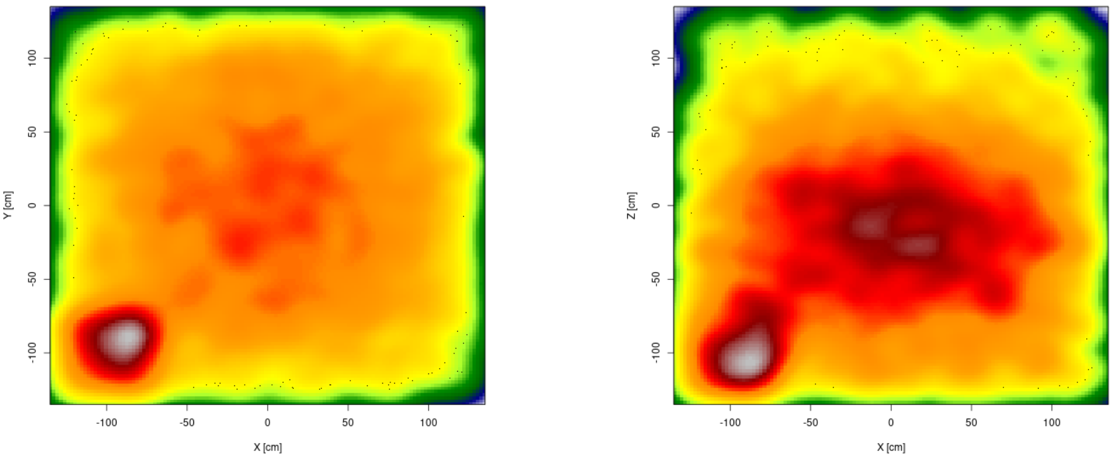

(c) Top view.

(d) Front view.

Figure C.3: POCA tomographies of the simulated cargo, which is composed of organic material, containing an anomaly of 50 x 50 x 50 cm^3 filled with guns. In the first row, the anomaly is placed in the centre of the cargo. In the second, it is in the front bottom left corner.

Extracted results are shown in fig. C.3. The top and front view of POCA tomographies can be observed, which infer the scattering density within the cargo volume, based on the POCA point density. The anomaly voxel produces a very clear higher concentration of muon scatters, as reconstructed by POCA algorithm. In the tomographies, its location is highlighted by white areas surrounded by reddish colours, that indicate high concentrations of POCA interaction points. The images of the first row belong to a simulation where the anomaly voxel is located in the centre of the cargo, while in the second row it can be observed the muography of a cargo with the anomaly in the front bottom left corner. In this second simulation, the reconstruction is not so clear, due to detector configuration effects, such as the smaller flux of detected muons which traverses the location of the anomaly.

These preliminary results show a case where a POCA muography algorithm is able to image the contrast between a base material and an anomaly inside it. As mentioned above, the data extracted with POCA reconstructions will be used to feed AI algorithms. Other approaches are also being explored. In this thesis, a preliminary analysis has been explained, which is the basis upon which the additional software research will be developed.

Figure references and licenses

[1] [196], https://creativecommons.org/licenses/by-nc-nd/3.0/deed.en, no changes have been made.
[2] [197], https://creativecommons.org/licenses/by-nc-nd/3.0/deed.en, no changes have been made.
[3] [43], https://creativecommons.org/licenses/by-nc/4.0/, no changes have been made.
[4] [47], https://creativecommons.org/licenses/by/3.0/, no changes have been made.
[5] [43], https://creativecommons.org/licenses/by-nc/4.0/, no changes have been made.
[6] [43], https://creativecommons.org/licenses/by-nc/4.0/, no changes have been made.
[7] [43], https://creativecommons.org/licenses/by-nc/4.0/, no changes have been made.
[8] [62], http://creativecommons.org/licenses/by-nc-nd/4.0/, no changes have been made.
[9] [51], http://creativecommons.org/licenses/BY-NC-ND/4.0/, no changes have been made.

Bibliography

[1] Charles Augustine Coulomb. “Troisieme memoire sur l’Electricite et le magnetisme”. In: *Histoire de l’Académie royale des sciences* (1785), pp. 612–638.

[2] Michael Faraday. “Experimental researches in electricity”. In: 2 (1844).

[3] William Crookes. “On Electrical Insulation in High Vacua”. In: *Proceedings of the Royal Society of London* 28 (1879), pp. 347–352.

[4] H Becquerel. “Sur les radiations émises par phosphorescence”. In: *Comptes Rendus de l’Académie des Sciences* 122 (1896), pp. 420–421.

[5] P Curie, M Curie, and G Bémont. “Sur une nouvelle substance fortement radio-active, contenue dans la pechblende”. In: *Comptes Rendus de l’Académie des Sciences* 127 (1898), pp. 1215–1217.

[6] Julius Elster and Hans Geiter. “Ueber Elektricitätszerstreuung in der Luft”. In: *Annalen der Physik* 2 (1900), p. 425.

[7] Charles Thomson Rees Wilson. “On the ionisation of atmospheric air”. In: *Proceedings of the Royal Society of London* 68 (442-450 Sept. 1901), pp. 151–161. ISSN: 0370-1662. DOI: `10.1098/rspl.1901.0032`.

[8] Franz Linke. “Luftelektrische Messungen bei zwölf Ballonfahrten”. In: *Abhandlungen der Königlichen Gesellschaft der Wissenschaften zu Göttingen. Mathematisch-physikalische Klase. Neue Folge.* 3 (5 1904). URL: `https://gdz.sub.uni-goettingen.de/id/PPN251726223_0003?tify=%5C%7B%22pages%22:[421]%5C%7D`.

[9] Theodor Wulf. “Über die in der Atmosphäre vorhandene Strahlung von höher Durchdringungsfähigkeit”. In: *Physikalische Zeitschrift* 10 (1909), pp. 152–157.

[10] Theodor Wulf. “Beobachtungen über die Strahlung höher Durchdringungsfähigkeit auf dem Eiffelturm”. In: *Physikalische Zeitschrift* 11 (1910), pp. 811–813.

[11] Karl Bergwitz. “Die Gammastrahlung des Erdkörpers und ihr Anteil an der spontanen Ionisierung der Atmosphäre”. In: *Jahresbericht des Braunschweiger Vereins für Naturwissenschaft* 10 (1910), pp. 196–239.

[12] Albert Gockel. “Luftelektrische Beobachtungen bei einer Ballonfahrt”. In: *Physikalische Zeitschrift* 11 (1910), pp. 280–282.

[13] Albert Gockel. “Messungen der durchdringenden Strahlung bei Ballonfahrten”. In: *Physikalische Zeitschrift* 12 (1911), pp. 595–597.

[14] Domenico Pacini. “Penetrating Radiation on the Sea”. In: *Le Radium* 8 (Jan. 1910), p. 307. URL: `http://arxiv.org/abs/1101.3015`.

[15] Victor Franz Hess. “Über Beobachtungen der durchdringenden Strahlung bei sieben Freiballonfahrten”. In: *Physikalische Zeitschrift* 13 (1912), pp. 1084–1091.

[16] Karl Bergwitz. "Untersuchung fiber Störungen am Apparat zur Beobachtung der durchdringenden Strahlung nach Wulf". In: *Physikalische Zeitschrift* 14 (1913), pp. 953–956.

[17] Werner Kolhörster. "Messungen der durchdringenden Strahlung im Freiballon in gröszeren H6he". In: *Physikalische Zeitschrift* 14 (1913), pp. 1153–1155.

[18] Werner Kolhörster. "Messungen der durchdringenden Strahlung bis in Höhen von 9300m". In: *Verhandlungen der Physikalischen Gesellschaft zu Berlin* 16 (1914), pp. 719–721.

[19] R. A. Millikan and G. H. Cameron. "The origin of the cosmic rays". In: *Physical Review* 32 (4 Oct. 1928), pp. 533–557. ISSN: 0031899X. DOI: 10.1103/PhysRev.32.533.

[20] Arthur H. Compton. "A geographic study of cosmic rays". In: *Physical Review* 43 (6 Mar. 1933), pp. 387–403. ISSN: 0031899X. DOI: 10.1103/PhysRev.43.387.

[21] Erich Regener. "Intensity of Cosmic Radiation in the High Atmosphere". In: *Nature* 130 (1932), p. 364.

[22] Erich Regener. "Die Absorptionskurve der Ultrastrahlung und ihre Deutung". In: *Physikalische Zeitschrift* 34 (1933), pp. 306–323.

[23] Erich Regener and Georg Pfotzer. "Intensity of the Cosmic Ultra-Radiation in the Stratosphere with the Tube-Counter". In: *Nature* 134 (1935), pp. 325–325.

[24] Erich Regener and Georg Pfotzer. "Vertical Intensity of Cosmic Rays by Threefold Coincidences in the Stratosphere". In: *Nature* 136 (1935), pp. 718–719.

[25] Bernhard Gross. "Zur Absorption der Ultrastrahlung". In: *Zeitschrift für Physik* 83 (1933), pp. 214–221.

[26] Georg Pfotzer. "Dreifachkoinzidenzen der Ultrastrahlung aus vertikaler Richtung in der Stratosphäre". In: *Zeitschrift für Physik* 102 (1936), pp. 23–40.

[27] I. S. Bowen and R. A. Millikan. "Cosmic Ray Intensity in the Stratosphere". In: *Physical Review* 43 (1933), pp. 695–700.

[28] Carl D. Anderson and Seth H. Neddermeyer. "Cloud chamber observations of cosmic rays at 4300 meters elevation and near sea-level". In: *Physical Review* 50 (4 1936). ISSN: 0031899X. DOI: 10.1103/PhysRev.50.263.

[29] Seth H. Neddermeyer and Carl D. Anderson. "Note on the nature of cosmic-ray particles". In: *Physical Review* 51 (10 1937). ISSN: 0031899X. DOI: 10.1103/PhysRev.51.884.

[30] J. C. Street and E. C. Stevenson. "New evidence for the existence of a particle of mass intermediate between the proton and electron". In: *Physical Review* 52 (9 1937), pp. 1003–1004. ISSN: 0031899X. DOI: 10.1103/PhysRev.52.1003.

[31] Carl D Anderson and Seth H Neddermeyer. "Mesotron (Intermediate Particle) as a Name for the New Particles of Intermediate Mass". In: *Nature* 142 (3602 1938), p. 878. ISSN: 1476-4687. DOI: 10.1038/142878c0. URL: https://doi.org/10.1038/142878c0.

[32] Bruno Rossi. "On the Magnetic Deflection of Cosmic Rays". In: *Physical Review* 36 (3 Aug. 1930), p. 606. DOI: 10.1103/PhysRev.36.606. URL: https://link.aps.org/doi/10.1103/PhysRev.36.606.

[33] Thomas H Johnson. "The Azimuthal Asymmetry of the Cosmic Radiation". In: *Physical Review* 43 (10 May 1933), pp. 834–835. DOI: 10.1103/PhysRev.43.834. URL: https://link.aps.org/doi/10.1103/PhysRev.43.834.

[34] Luis Alvarez and Arthur H Compton. “A Positively Charged Component of Cosmic Rays”. In: *Physical Review* 43 (10 May 1933), pp. 835–836. DOI: 10.1103/PhysRev.43.835. URL: https://link.aps.org/doi/10.1103/PhysRev.43.835.

[35] Bruno Rossi. “Directional Measurements on the Cosmic Rays Near the Geomagnetic Equator”. In: *Physical Review* 45 (3 Feb. 1934), pp. 212–214. DOI: 10.1103/PhysRev.45.212. URL: https://link.aps.org/doi/10.1103/PhysRev.45.212.

[36] Bruno Rossi and David B. Hall. “Variation of the Rate of Decay of Mesotrons with Momentum”. In: *Physical Review* 59 (3 Feb. 1941), pp. 223–228. ISSN: 0031-899X. DOI: 10.1103/PhysRev.59.223. URL: https://link.aps.org/doi/10.1103/PhysRev.59.223.

[37] David H. Frisch and James H. Smith. “Measurement of the Relativistic Time Dilation Using μ-Mesons”. In: *American Journal of Physics* 31 (5 May 1963), pp. 342–355. ISSN: 0002-9505. DOI: 10.1119/1.1969508. URL: http://aapt.scitation.org/doi/10.1119/1.1969508.

[38] J Bailey et al. “Measurements of relativistic time dilatation for positive and negative muons in a circular orbit”. In: *Nature* 268 (5618 1977), pp. 301–305.

[39] R.L Workman and et al. “Review of Particle Physics”. In: 30 (Cosmic Rays 2022). URL: https://pdg.lbl.gov/2022/reviews/rpp2022-rev-cosmic-rays.pdf.

[40] R.L et al Workman and et al. “Review of Particle Physics”. In: 34 (Passage of Particles Trough Matter 2022). URL: https://pdg.lbl.gov/2022/reviews/rpp2022-rev-passage-particles-matter.pdf.

[41] R.L Workman and et al. “Review of Particle Physics”. In: (Muon 2022). URL: https://pdg.lbl.gov/2022/listings/rpp2022-list-muon.pdf.

[42] P. K. F. Grieder. *Cosmic rays at Earth : researcher’s reference manual and data book*. Elsevier Science Ltd, 2001. ISBN: 9780080530055.

[43] R.L et al Workman. “Review of Particle Physics”. In: *PTEP* 2022 (2022), p. 083C01. DOI: 10.1093/ptep/ptac097.

[44] M. P. De Pascale et al. “Absolute spectrum and charge ratio of cosmic ray muons in the energy region from 0.2 GeV to 100 GeV at 600 m above sea level”. In: *Journal of Geophysical Research: Space Physics* 98 (A3 Mar. 1993), pp. 3501–3507. DOI: 10.1029/92ja02672.

[45] P. Achard et al. “Measurement of the atmospheric muon spectrum from 20 to 3000 GeV”. In: *Physics Letters, Section B: Nuclear, Elementary Particle and High-Energy Physics* 598 (1-2 Sept. 2004), pp. 15–32. ISSN: 03702693. DOI: 10.1016/j.physletb.2004.08.003.

[46] J. Kremer et al. “Measurements of ground-level muons at two geomagnetic locations”. In: *Physical Review Letters* 83 (21 Jan. 1999), pp. 4241–4244. ISSN: 10797114. DOI: 10.1103/PhysRevLett.83.4241.

[47] S. Haino et al. “Measurements of primary and atmospheric cosmic-ray spectra with the BESS-TeV spectrometer”. In: *Physics Letters, Section B: Nuclear, Elementary Particle and High-Energy Physics* 594 (1-2 July 2004), pp. 35–46. ISSN: 03702693. DOI: 10.1016/j.physletb.2004.05.019.

[48] Prashant Shukla and Sundaresh Sankrith. “Energy and angular distributions of atmospheric muons at the Earth”. In: (June 2016). URL: http://arxiv.org/abs/1606.06907.

[49] H Jokisch et al. “Cosmic-ray muon spectrum up to 1 TeV at 75º zenith angle”. In: (1979).

[50] Shuhei Tsuji et al. "Measurements of muons at sea level". In: *Journal of Physics G: Nuclear and Particle Physics* 24 (9 Sept. 1998), pp. 1805–1822. ISSN: 09543899. DOI: 10.1088/0954-3899/24/9/013.

[51] L. Bonechi, R. D'Alessandro, and A. Giammanco. "Atmospheric muons as an imaging tool". In: *Reviews in Physics* 5 (2020). DOI: 10.1016/j.revip.2020.100038.

[52] H. A. Bethe. "Molière's theory of multiple scattering". In: *Physical Review* 89 (6 1953), pp. 1256–1266. ISSN: 0031899X. DOI: 10.1103/PHYSREV.89.1256.

[53] Virgil L. Highland. "Some practical remarks on multiple scattering". In: *Nuclear Instruments and Methods* 129 (2 Nov. 1975), pp. 497–499. ISSN: 0029-554X. DOI: 10.1016/0029-554X(75)90743-0.

[54] Gerald R Lynch and Orin I. Dahl. "Approximations to multiple Coulomb scattering". In: *Nuclear Inst. and Methods in Physics Research, B* 58 (1 1991), pp. 6–10. ISSN: 0168583X. DOI: 10.1016/0168-583X(91)95671-Y.

[55] Yung-Su Tsai. "Pair production and bremsstrahlung of charged leptons". In: *Reviews of Modern Physics* 46 (4 Oct. 1974), pp. 815–851. DOI: 10.1103/RevModPhys.46.815. URL: https://link.aps.org/doi/10.1103/RevModPhys.46.815.

[56] *Atomic and Nuclear Properties of Materials (pdf version)*. URL: https://pdg.lbl.gov/2023/reviews/rpp2022-rev-atomic-nuclear-prop.pdf.

[57] *Atomic and Nuclear Properties of Materials (interactive website)*. URL: https://pdg.lbl.gov/2023/AtomicNuclearProperties/.

[58] S. Vanini et al. "Muography of different structures using muon scattering and absorption algorithms". In: *Philosophical Transactions of the Royal Society A: Mathematical, Physical and Engineering Sciences* 377 (2137 2019). ISSN: 1364503X. DOI: 10.1098/RSTA.2018.0051.

[59] S. Pesente et al. "First results on material identification and imaging with a large-volume muon tomography prototype". In: *Nuclear Instruments and Methods in Physics Research, Section A: Accelerators, Spectrometers, Detectors and Associated Equipment* 604 (3 June 2009), pp. 738–746. ISSN: 01689002. DOI: 10.1016/J.NIMA.2009.03.017.

[60] P. Checchia et al. "INFN muon tomography demonstrator: Past and recent results with an eye to near-future activities". In: *Philosophical Transactions of the Royal Society A: Mathematical, Physical and Engineering Sciences* 377 (2137 2019). ISSN: 1364503X. DOI: 10.1098/RSTA.2018.0065.

[61] Pablo Martínez-Ruiz del Árbol et al. "Applications of Muography to the Industrial Sector". en. In: *Journal of Advanced Instrumentation in Science* (Apr. 2022). DOI: 10.31526/jais.2022.267. URL: http://journals.andromedapublisher.com/index.php/JAIS/article/view/267 (visited on 06/24/2022).

[62] V. Anghel et al. "A plastic scintillator-based muon tomography system with an integrated muon spectrometer". In: *Nuclear Instruments and Methods in Physics Research, Section A: Accelerators, Spectrometers, Detectors and Associated Equipment* 798 (July 2015), pp. 12–23. ISSN: 01689002. DOI: 10.1016/j.nima.2015.06.054.

[63] A. Anastasio et al. "The MU-RAY experiment. An application of SiPM technology to the understanding of volcanic phenomena". In: *Nuclear Instruments and Methods in Physics Research Section A: Accelerators, Spectrometers, Detectors and Associated Equipment* 718 (Aug. 2013), pp. 134–137. ISSN: 0168-9002. DOI: 10.1016/J.NIMA.2012.08.065.

[64] Raffaello D'Alessandro et al. "Volcanoes in Italy and the role of muon radiography". In: *Philosophical Transactions of the Royal Society A: Mathematical, Physical and Engineering Sciences* 377 (2137 2019). ISSN: 1364503X. DOI: 10.1098/rsta.2018.0050.

[65] Alain Bonneville et al. "Borehole muography of subsurface reservoirs". In: *Philosophical Transactions of the Royal Society A: Mathematical, Physical and Engineering Sciences* 377 (2137 2019). ISSN: 1364503X. DOI: 10.1098/rsta.2018.0060.

[66] Jon Gluyas et al. "Passive, continuous monitoring of carbon dioxide geostorage using muon tomography". In: *Philosophical Transactions of the Royal Society A: Mathematical, Physical and Engineering Sciences* 377 (2137 2019). ISSN: 1364503X. DOI: 10.1098/rsta.2018.0059.

[67] M. Basset et al. "MGR: An innovative, low-cost and compact cosmic-ray detector". In: *Nuclear Instruments and Methods in Physics Research, Section A: Accelerators, Spectrometers, Detectors and Associated Equipment* 567 (1 SPEC. ISS. Nov. 2006), pp. 298–301. ISSN: 01689002. DOI: 10.1016/j.nima.2006.05.099.

[68] David Mahon et al. "First-of-a-kind muography for nuclear waste characterization". In: *Philosophical Transactions of the Royal Society A: Mathematical, Physical and Engineering Sciences* 377 (2137 2019). ISSN: 1364503X. DOI: 10.1098/rsta.2018.0048.

[69] Kunihiro Morishima et al. "Development of nuclear emulsion for muography". In: *Annals of Geophysics* (2017). ISSN: 2037416x. DOI: 10.4401/ag-7387.

[70] R. Nishiyama et al. "First measurement of ice-bedrock interface of alpine glaciers by cosmic muon radiography". en. In: *Geophysical Research Letters* 44.12 (2017), pp. 6244–6251. ISSN: 1944-8007. DOI: 10.1002/2017GL073599. URL: https://onlinelibrary.wiley.com/doi/abs/10.1002/2017GL073599 (visited on 06/06/2023).

[71] R. Nishiyama et al. "Bedrock sculpting under an active alpine glacier revealed from cosmic-ray muon radiography". en. In: *Scientific Reports* 9.1 (May 2019). Number: 1 Publisher: Nature Publishing Group, p. 6970. ISSN: 2045-2322. DOI: 10.1038/s41598-019-43527-6. URL: https://www.nature.com/articles/s41598-019-43527-6 (visited on 06/06/2023).

[72] Valeri Tioukov et al. "First muography of Stromboli volcano". In: *Scientific Reports* 9 (1 Dec. 2019), pp. 1–11. ISSN: 20452322. DOI: 10.1038/s41598-019-43131-8.

[73] Kunihiro Morishima et al. "Discovery of a big void in Khufu's Pyramid by observation of cosmic-ray muons". In: *Nature* 552 (Dec. 2017), pp. 386–390. ISSN: 14764687. DOI: 10.1038/nature24647.

[74] Sébastien Procureur et al. "Precise characterization of a corridor-shaped structure in Khufu's Pyramid by observation of cosmic-ray muons". In: *Nature communications* 14 (1 Mar. 2023), p. 1144. ISSN: 20411723. DOI: 10.1038/s41467-023-36351-0.

[75] Vishal Kumar. "Comparative study of gas detectors and their suitability for imaging". In: (2022).

[76] O. Catalano et al. "Volcanoes muon imaging using Cherenkov telescopes". In: *Nuclear Instruments and Methods in Physics Research, Section A: Accelerators, Spectrometers, Detectors and Associated Equipment* 807 (Jan. 2016), pp. 5–12. ISSN: 01689002. DOI: 10.1016/j.nima.2015.10.065.

[77] Junghyun Bae and Stylianos Chatzidakis. "Momentum-Dependent Cosmic Ray Muon Computed Tomography Using a Fieldable Muon Spectrometer". In: *Energies* 15 (7 Apr. 2022), p. 2666. ISSN: 1996-1073. DOI: 10.3390/EN15072666. URL: https://www.mdpi.com/1996-1073/15/7/2666.

[78] A. Harel and D. Yaish. “Lingacom muography”. In: *Philosophical Transactions of the Royal Society A: Mathematical, Physical and Engineering Sciences* 377 (2137 2019). ISSN: 1364503X. DOI: 10.1098/rsta.2018.0133.

[79] G. Charpak et al. “The use of multiwire proportional counters to select and localize charged particles”. In: *Nuclear Instruments and Methods* 62 (3 July 1968), pp. 262–268. ISSN: 0029554X. DOI: 10.1016/0029-554X(68)90371-6.

[80] Luigi Rolandi, Werner Riegler, and Walter Blum. *Particle Detection with Drift Chambers.* 2nd ed. Springer Berlin, Heidelberg, 2008. DOI: https://doi.org/10.1007/978-3-540-76684-1. URL: https://link.springer.com/book/10.1007/978-3-540-76684-1.

[81] T. Argyropoulos et al. “Cathode strip chambers in ATLAS : Installation, commissioning and in situ performance”. In: 2008, pp. 2819–2824. ISBN: 9781424427154. DOI: 10.1109/NSSMIC.2008.4774958.

[82] Dezsö Varga et al. “High Efficiency Gaseous Tracking Detector for Cosmic Muon Radiography”. In: *Advances in High Energy Physics* 2016 (2016). ISSN: 16877365. DOI: 10.1155/2016/1962317.

[83] L. Oláh et al. “CCC-based muon telescope for examination of natural caves”. In: *Geoscientific Instrumentation, Methods and Data Systems* 1 (2 Dec. 2012), pp. 229–234. ISSN: 21930864. DOI: 10.5194/gi-1-229-2012.

[84] László Oláh et al. “High-definition and low-noise muography of the Sakurajima volcano with gaseous tracking detectors”. In: *Scientific Reports* 8 (1 Dec. 2018), pp. 1–13. ISSN: 20452322. DOI: 10.1038/s41598-018-21423-9.

[85] László Oláh et al. “Investigation of the limits of high-definition muography for observation of Mt Sakurajima”. In: *Philosophical Transactions of the Royal Society A: Mathematical, Physical and Engineering Sciences* 377 (2137 2019). ISSN: 1364503X. DOI: 10.1098/rsta.2018.0135.

[86] D. Varga et al. “Detector developments for high performance Muography applications”. In: *Nuclear Instruments and Methods in Physics Research, Section A: Accelerators, Spectrometers, Detectors and Associated Equipment* 958 (Apr. 2020), p. 162236. ISSN: 01689002. DOI: 10.1016/j.nima.2019.05.077.

[87] László Oláh et al. “The first prototype of an MWPC-based borehole-detector and its application for muography of an underground pillar”. In: *BUTSURI-TANSA(Geophysical Exploration)* 71 (0 2018), pp. 161–168. ISSN: 0912-7984. DOI: 10.3124/segj.71.161.

[88] László Oláh et al. “Improvement of cosmic-ray muography for Earth sciences and civil engineering”. In: vol. 358. Sissa Medialab Srl, July 2019. DOI: 10.22323/1.358.0377.

[89] R. Santonico and R. Cardarelli. “Development of resistive plate counters”. In: *Nuclear Instruments and Methods* 187 (2-3 Aug. 1981), pp. 377–380. ISSN: 0029554X. DOI: 10.1016/0029-554X(81)90363-3.

[90] A. Samalan et al. *Small-area portable resistive plate chambers for muography.* June 2023. URL: https://indi.to/g5myP.

[91] G. Aielli et al. “Performance of a large-size RPC equipped with the final ATLAS front-end electronics at X5-GIF irradiation facility”. In: *Nuclear Instruments and Methods in Physics Research, Section A: Accelerators, Spectrometers, Detectors and Associated Equipment* 456 (1-2 Dec. 2000), pp. 77–81. ISSN: 01689002. DOI: 10.1016/S0168-9002(00)00966-9.

[92] P. Baesso et al. “A high resolution resistive plate chamber tracking system developed for cosmic ray muon tomography”. In: *Journal of Instrumentation* 8 (8 Aug. 2013), P08006. ISSN: 17480221. DOI: 10.1088/1748-0221/8/08/P08006.

[93] Sophie Wuyckens et al. “A portable muon telescope based on small and gas-tight resistive plate chambers”. In: *Philosophical Transactions of the Royal Society A: Mathematical, Physical and Engineering Sciences* 377 (2137 2019). ISSN: 1364503X. DOI: 10.1098/rsta.2018.0139.

[94] R. M.I.D. Gamage et al. “Portable Resistive Plate Chambers for Muography in confined environments”. In: vol. 357. EDP Sciences, Sept. 2022, p. 01001. DOI: 10.1051/e3sconf/202235701001.

[95] F. Ambrosino et al. “Joint measurement of the atmospheric muon flux through the Puy de Dôme volcano with plastic scintillators and Resistive Plate Chambers detectors”. In: *Journal of Geophysical Research: Solid Earth* 120 (11 Nov. 2015), pp. 7290–7307. ISSN: 2169-9313. DOI: 10.1002/2015JB011969. URL: https://agupubs.onlinelibrary.wiley.com/doi/10.1002/2015JB011969.

[96] Christopher L. Morris et al. “Horizontal cosmic ray muon radiography for imaging nuclear threats”. In: *Nuclear Instruments and Methods in Physics Research, Section B: Beam Interactions with Materials and Atoms* 330 (July 2014), pp. 42–46. ISSN: 0168583X. DOI: 10.1016/j.nimb.2014.03.017.

[97] Serge Duarte Pinto. “Micropattern gas detector technologies and applications the work of the RD51 collaboration”. In: 2010, pp. 802–807. ISBN: 9781424491063. DOI: 10.1109/NSSMIC.2010.5873870.

[98] Ignacio Lázaro Roche et al. “Design, Construction and in Situ Testing of a Muon Camera for Earth Science and Civil Engineering Applications”. In: vol. 88. EDP Sciences, Feb. 2019, p. 01003. DOI: 10.1051/e3sconf/20198801003.

[99] Ignacio Lázaro Roche, J. B. Decitre, and S. Gaffet. “MUon Survey Tomography based on Micromegas detectors for Unreachable Sites Technology (MUST2): Overview and outlook.” In: vol. 1498. Institute of Physics Publishing, June 2020, p. 012048. DOI: 10.1088/1742-6596/1498/1/012048.

[100] Chris Hagmann, David Lange, and Douglas Wright. “Cosmic-ray shower generator (CRY) for Monte Carlo transport codes”. In: vol. 2. 2007, pp. 1143–1146. ISBN: 1424409233. DOI: 10.1109/NSSMIC.2007.4437209.

[101] D. Pagano et al. “EcoMug: An Efficient COsmic MUon Generator for cosmic-ray muon applications”. In: *Nuclear Instruments and Methods in Physics Research, Section A: Accelerators, Spectrometers, Detectors and Associated Equipment* 1014 (Oct. 2021), p. 165732. ISSN: 01689002. DOI: 10.1016/j.nima.2021.165732.

[102] D Pagano et al. “Update on EcoMug cosmic-ray muon generator”. In: June 2023. URL: https://indico.cern.ch/event/1203839/contributions/5332762/.

[103] S. Agostinelli et al. “GEANT4 - A simulation toolkit”. In: *Nuclear Instruments and Methods in Physics Research, Section A: Accelerators, Spectrometers, Detectors and Associated Equipment* 506 (3 July 2003), pp. 250–303. ISSN: 01689002. DOI: 10.1016/S0168-9002(03)01368-8.

[104] Ahmet Ilker Topuz et al. "Preliminaries for muon tracking in GEANT4 simulations". In: (2022). DOI: 10.1002/essoar.10512190.1. URL: https://doi.org/10.1002/essoar.10512190.1.

[105] *Geant4 Documentation - Geant4*. URL: https://geant4.web.cern.ch/docs/.

[106] P.M. Ruiz-Del Arbol et al. "Non-destructive testing of industrial equipment using muon radiography". In: *Philosophical Transactions of the Royal Society A: Mathematical, Physical and Engineering Sciences* 377 (2137 2019). ISSN: 1364503X. DOI: 10.1098/rsta.2018.0054.

[107] Aitor Orio-Alonso et al. "Estimation of the Snow Water Equivalent Using Muon Scattering Radiography". en. In: *Geophysical Research Letters* 50.14 (2023), e2023GL104128. ISSN: 1944-8007. DOI: 10.1029/2023GL104128. URL: https://onlinelibrary.wiley.com/doi/abs/10.1029/2023GL104128 (visited on 07/28/2023).

[108] Nicola Mori et al. "A geant4 framework for generic simulations of atmospheric muon detection experiments". In: *Annals of Geophysics* 60 (1 2017). ISSN: 2037416x. DOI: 10.4401/AG-7383.

[109] William C. Priedhorsky et al. "Detection of high-Z objects using multiple scattering of cosmic ray muons". In: *Review of Scientific Instruments* 74 (10 Oct. 2003), pp. 4294–4297. ISSN: 00346748. DOI: 10.1063/1.1606536.

[110] Stylianos Chatzidakis, Chan K. Choi, and Lefteri H. Tsoukalas. "Analysis of Spent Nuclear Fuel Imaging Using Multiple Coulomb Scattering of Cosmic Muons". In: *IEEE Transactions on Nuclear Science* 63 (6 Dec. 2016), pp. 2866–2874. ISSN: 00189499. DOI: 10.1109/TNS.2016.2618009.

[111] Tommaso Dorigo et al. "Toward the end-to-end optimization of particle physics instruments with differentiable programming". In: *Reviews in Physics* 10 (June 2023). ISSN: 24054283. DOI: 10.1016/j.revip.2023.100085.

[112] G Strong et al. "Detector optimization in Muon Scattering Tomography-22 2023 Naples". In: June 2023. URL: https://indico.cern.ch/event/1203839/contributions/5332772/.

[113] M. Stapleton et al. "Angle Statistics Reconstruction: A robust reconstruction algorithm for Muon Scattering Tomography". In: *Journal of Instrumentation* 9 (11 Nov. 2014). ISSN: 17480221. DOI: 10.1088/1748-0221/9/11/P11019.

[114] Larry Joe Schultz. "COSMIC RAY MUON RADIOGRAPHY". In: (2003).

[115] Larry J. Schultz et al. "Statistical reconstruction for cosmic ray muon tomography". In: *IEEE Transactions on Image Processing* (2007). ISSN: 10577149. DOI: 10.1109/TIP.2007.901239.

[116] Anna Bordignon. "Algoritmo EM per la risoluzione di un problema di imaging nella Tomografia Muonica per scattering". In: (2023). URL: https://thesis.unipd.it/handle/20.500.12608/38802%20https://hdl.handle.net/20.500.12608/38802.

[117] John Aldrich. "R.A. Fisher and the making of maximum likelihood 1912-1922". In: *Statistical Science* 12 (3 Sept. 1997), pp. 162–176. ISSN: 0883-4237. DOI: 10.1214/ss/1030037906. URL: https://projecteuclid.org/journals/statistical-science/volume-12/issue-3/RA-Fisher-and-the-making-of-maximum-likelihood-1912-1922/10.1214/ss/1030037906.full.

[118] A P Dempster, N M Laird, and D B Rubin. *Maximum Likelihood from Incomplete Data via the EM Algorithm*. 1977. URL: https://www.jstor.org/stable/2984875.

[119] George E.P. “Cosmic rays measure overburden of tunnel”. In: *Commonwealth Engineer* (1955), pp. 455–457.

[120] L F Thompson et al. “Muon tomography for railway tunnel imaging”. In: *PHYSICAL REVIEW RESEARCH* 2 (2020). DOI: 10.1103/PhysRevResearch.2.023017.

[121] E. Guardincerri et al. “Imaging the inside of thick structures using cosmic rays”. In: *AIP Advances* 6 (Jan. 2016). DOI: 10.1063/1.4940897.

[122] E. Guardincerri et al. “Imaging the dome of Santa Maria del Fiore using cosmic rays”. In: *Philosophical Transactions of the Royal Society A: Mathematical, Physical and Engineering Sciences* 377 (2019). DOI: 10.1098/RSTA.2018.0136.

[123] Aldo Zenoni. “Historical building stability monitoring by means of a cosmic ray tracking system”. In: *2015 4th International Conference on Advancements in Nuclear Instrumentation Measurement Methods and their Applications (ANIMMA)* (2015). DOI: 10.1109/ANIMMA.2015.7465542.

[124] Kullapha Chaiwongkhot et al. “Development of a portable muography detector for infrastructure degradation investigation”. In: *IEEE Transactions on Nuclear Science* 65 (8 Aug. 2018), pp. 2316–2324. DOI: 10.1109/TNS.2018.2855737.

[125] Ernst Niederleithinger et al. “Muon Tomography of the Interior of a Reinforced Concrete Block: First Experimental Proof of Concept”. In: *Journal of Nondestructive Evaluation* 40 (3 Sept. 2021), pp. 1–14. ISSN: 15734862. DOI: 10.1007/S10921-021-00797-3/FIGURES/8. URL: https://link.springer.com/article/10.1007/s10921-021-00797-3.

[126] Subhendu Das et al. “Muography for Inspection of Civil Structures”. In: *Instruments* 6 (4 Nov. 2022), p. 77. ISSN: 2410-390X. DOI: 10.3390/instruments6040077. URL: https://www.mdpi.com/2410-390X/6/4/77.

[127] Luis W. Alvarez et al. “Search for hidden chambers in the pyramids”. In: *Science* 167 (3919 1970), pp. 832–839. ISSN: 00368075. DOI: 10.1126/science.167.3919.832.

[128] S. Aguilar et al. “Searching for cavities in the Teotihuacan Pyramid of the Sun using cosmic muons: preliminary results”. In: *Proceedings of the 32nd International Cosmic Ray Conference, ICRC 2011* 4 (2011), pp. 325–328. DOI: 10.7529/ICRC2011/V04/1117.

[129] Lucina Melesio. “The pyramid detectives”. In: *Physics World* 27 (12 2014), pp. 24–27.

[130] *Maya Muon*. URL: http://www.hep.utexas.edu/mayamuon/.

[131] G Saracino et al. “Imaging of underground cavities with cosmic-ray muons from observations at Mt. Echia (Naples)”. In: *Scientific Reports* 7 (2017). DOI: 10.1038/s41598-017-01277-3. URL: www.nature.com/scientificreports/.

[132] G Saracino et al. “Applications of muon absorption radiography to the fields of archaeology and civil engineering”. In: *Philosophical Transactions of the Royal Society A: Mathematical, Physical and Engineering Sciences* 377 (2019). DOI: 10.1098/rsta.2018.0057. URL: http://dx.doi.org/10.1098/rsta.2018.0057.

[133] Luigi Cimmino et al. “3D Muography for the Search of Hidden Cavities”. In: *Scientific Reports* 9 (Dec. 2019). DOI: 10.1038/S41598-019-39682-5.

[134] Rebecca Gugerli, Darin Desilets, and Nadine Salzmann. “Brief communication: Application of a muonic cosmic ray snow gauge to monitor the snow water equivalent on alpine glaciers”. English. In: *The Cryosphere* 16.3 (Mar. 2022). Publisher: Copernicus GmbH, pp. 799–806. ISSN: 1994-0416. DOI: 10.5194/tc-16-799-2022. URL: https://tc.copernicus.org/articles/16/799/2022/ (visited on 06/06/2023).

[135] F. Ambrosino et al. “The MU-RAY project: Detector technology and first data from Mt. Vesuvius”. In: *Journal of Instrumentation* 9 (2 Feb. 2014), p. C02029. ISSN: 17480221. DOI: 10.1088/1748-0221/9/02/C02029.

[136] D. Lo Presti et al. “The MEV project: Design and testing of a new high-resolution telescope for muography of Etna Volcano”. In: *Nuclear Instruments and Methods in Physics Research, Section A: Accelerators, Spectrometers, Detectors and Associated Equipment* 904 (Oct. 2018), pp. 195–201. ISSN: 01689002. DOI: 10.1016/j.nima.2018.07.048.

[137] C. Cârloganu et al. “Towards a muon radiography of the Puy de Dôme”. In: *Geoscientific Instrumentation, Methods and Data Systems* 2 (1 Feb. 2013), pp. 55–60. ISSN: 21930864. DOI: 10.5194/gi-2-55-2013.

[138] Kevin Jourde et al. “Muon dynamic radiography of density changes induced by hydrothermal activity at the La Soufrière of Guadeloupe volcano”. In: *Scientific Reports* 6 (1 Sept. 2016), pp. 1–12. ISSN: 20452322. DOI: 10.1038/srep33406.

[139] Y. Le Gonidec et al. “Abrupt changes of hydrothermal activity in a lava dome detected by combined seismic and muon monitoring”. In: *Scientific Reports* 9 (1 Dec. 2019), pp. 1–9. ISSN: 20452322. DOI: 10.1038/s41598-019-39606-3.

[140] Hiroyuki K. M. Tanaka et al. “Detecting a mass change inside a volcano by cosmic-ray muon radiography (muography): First results from measurements at Asama volcano, Japan”. In: *Geophysical Research Letters* 36 (17 Sept. 2009), p. L17302. ISSN: 0094-8276. DOI: 10.1029/2009GL039448. URL: http://doi.wiley.com/10.1029/2009GL039448.

[141] Hiroyuki K.M. Tanaka, Taro Kusagaya, and Hiroshi Shinohara. “Radiographic visualization of magma dynamics in an erupting volcano”. In: *Nature communications* 5 (1 Mar. 2014), p. 3381. ISSN: 20411723. DOI: 10.1038/ncomms4381.

[142] E. Caffau, F. Coren, and G. Giannini. “Underground cosmic-ray measurement for morphological reconstruction of the ”Grotta Gigante” natural cave”. In: *Nuclear Instruments and Methods in Physics Research, Section A: Accelerators, Spectrometers, Detectors and Associated Equipment* 385 (3 Feb. 1997), pp. 480–488. ISSN: 01689002. DOI: 10.1016/S0168-9002(96)01041-8.

[143] L. Malmqvist et al. “Theoretical studies of in-situ rock density determinations using underground cosmic-ray muon intensity measurements with application in mining geophysics”. In: *GEOPHYSICS* 44 (9 Sept. 1979), pp. 1549–1569. ISSN: 0016-8033. DOI: 10.1190/1.1441026. URL: https://library.seg.org/doi/10.1190/1.1441026.

[144] Doug Schouten. *Muon geotomography: Selected case studies.* 2019. DOI: 10.1098/rsta.2018.0061.

[145] Diletta Borselli et al. “Three-dimensional muon imaging of cavities inside the Temperino mine (Italy)”. In: *Scientific reports* 12 (1 Dec. 2022), p. 22329. ISSN: 20452322. DOI: 10.1038/s41598-022-26393-7.

[146] Kanetada Nagamine et al. “Probing the inner structure of blast furnaces by cosmic-ray muon radiography”. In: *Proceedings of the Japan Academy, Series B* 81 (7 2005), pp. 257–260.

[147] L. Bonechi et al. “BLEMAB European project: Muon imaging technique applied to blast furnaces”. In: vol. 17. Institute of Physics, Apr. 2022, p. C04031. DOI: 10.1088/1748-0221/17/04/C04031.

[148] D. Borselli et al. “The BLEMAB European project: Muon radiography as an imaging tool in the industrial field”. In: vol. 45. Italian Physical Society, Nov. 2022. DOI: 10.1393/ncc/i2022-22201-x.

[149] *BLEMAB project*. URL: https://www.blemab.eu/.

[150] M. Furlan et al. “Muons scanner to detect radioactive source hidden in scrap metal containers: Mu-steel EU project”. In: 2013, pp. 601–606. ISBN: 9781479915354. DOI: 10.1109/THS.2013.6699072.

[151] *MU-Steel project*. URL: https://op.europa.eu/en/publication-detail/-/publication/78be2c6e-d54d-40ab-9025-19700131d550/language-en.

[152] Pablo Martínez-Ruiz del Árbol et al. “Non-destructive testing of industrial equipment using muon radiography”. In: *Philosophical transactions. Series A, Mathematical, physical, and engineering sciences* 377.2137 (2018). ISSN: 14712962. DOI: 10.1098/rsta.2018.0054.

[153] F. Riggi et al. “The Muon Portal Project: Commissioning of the full detector and first results”. In: *Nuclear Instruments and Methods in Physics Research, Section A: Accelerators, Spectrometers, Detectors and Associated Equipment* 912 (Dec. 2018), pp. 16–19. ISSN: 01689002. DOI: 10.1016/j.nima.2017.10.006.

[154] Oleg Kamaev et al. “Complementary non-destructive detection of nuclear materials with passive neutron and gamma-ray detectors, and a large-volume muon tomography system”. In: *Nuclear Instruments and Methods in Physics Research, Section A: Accelerators, Spectrometers, Detectors and Associated Equipment* 944 (Nov. 2019), p. 162503. ISSN: 01689002. DOI: 10.1016/j.nima.2019.162503.

[155] *About - Decision Sciences*. URL: https://www.decisionsciences.com/about/.

[156] *SilentBorder Project - Funded by the European Union*. URL: https://silentborder.eu/.

[157] *MUON CARGO — Muon Systems*. URL: https://muon.systems/en/muoncargo.

[158] Aitor Orio et al. “The MUON CARGO project: maritime transport container and vehicle inspection by means of muon scattering tomography”. In: 2023. URL: https://indico.cern.ch/event/1203839/contributions/5332824/.

[159] Sarah Barnes et al. “Cosmic-Ray Tomography for Border Security”. In: *Instruments* 7 (1 Mar. 2023), p. 13. ISSN: 2410390X. DOI: 10.3390/instruments7010013.

[160] G. Jonkmans et al. “Nuclear waste imaging and spent fuel verification by muon tomography”. In: *Annals of Nuclear Energy* 53 (Mar. 2013), pp. 267–273. ISSN: 18732100. DOI: 10.1016/j.anucene.2012.09.011.

[161] A. Clarkson et al. “Characterising encapsulated nuclear waste using cosmic-ray muon tomography”. In: *Journal of Instrumentation* 10 (3 Mar. 2015), P03020. ISSN: 17480221. DOI: 10.1088/1748-0221/10/03/P03020.

[162] F. Ambrosino et al. “Assessing the feasibility of interrogating nuclear waste storage silos using cosmic-ray muons”. In: *Journal of Instrumentation* 10 (6 June 2015), T06005. ISSN: 17480221. DOI: 10.1088/1748-0221/10/06/T06005.

[163] Konstantin Borozdin et al. “Cosmic ray radiography of the damaged cores of the fukushima reactors”. In: *Physical Review Letters* 109 (15 Oct. 2012), p. 152501. ISSN: 00319007. DOI: 10.1103/PhysRevLett.109.152501.

[164] Haruo Miyadera et al. “Imaging Fukushima Daiichi reactors with muons”. In: *AIP Advances* 3 (5 May 2013). ISSN: 21583226. DOI: 10.1063/1.4808210.

[165] N. Kume et al. "Muon trackers for imaging a nuclear reactor". In: *Journal of Instrumentation* 11 (9 Sept. 2016), P09008. ISSN: 17480221. DOI: 10.1088/1748-0221/11/09/P09008.

[166] Hirofumi Fujii et al. "Imaging the inner structure of a nuclear reactor by cosmic muon radiography". In: *Progress of Theoretical and Experimental Physics* 2019 (5 May 2019). ISSN: 2050-3911. DOI: 10.1093/ptep/ptz040. URL: https://academic.oup.com/ptep/article/doi/10.1093/ptep/ptz040/5498281.

[167] Märt Mägi, Madis Kiisk, and Andi Hektor. "Imaging military nuclear reactors with GScan's detector system". In: June 2023. URL: https://indico.cern.ch/event/1203839/contributions/5332832/.

[168] *GScan: Home. Scan anything. Detect everything — 3D Muon Tomography.* URL: https://www.gscan.eu/.

[169] Aitor Orio et al. "Feasibility of defect detection in concrete cylinders by means of Muon Scattering Radiography (MSR)". In: REHABEND 2022, 2022, pp. 1468–1475.

[170] Aitor Orio et al. "The MUON CARGO project: maritime transport container and vehicle inspection by means of muon scattering tomography". In: 2023. URL: https://indico.cern.ch/event/1203839/contributions/5332824/.

[171] Aitor Orio et al. "Exploring the potential of cosmic muon scattering to measure the snow water equivalent". In: May 2022.

[172] T. P. Barnett, J. C. Adam, and D. P. Lettenmaier. "Potential impacts of a warming climate on water availability in snow-dominated regions". en. In: *Nature* 438.7066 (Nov. 2005), pp. 303–309. ISSN: 0028-0836, 1476-4687. DOI: 10.1038/nature04141. URL: http://www.nature.com/articles/nature04141 (visited on 06/21/2022).

[173] Kari Luojus et al. "GlobSnow v3.0 Northern Hemisphere snow water equivalent dataset". en. In: *Scientific Data* 8.1 (Dec. 2021), p. 163. ISSN: 2052-4463. DOI: 10.1038/s41597-021-00939-2. URL: http://www.nature.com/articles/s41597-021-00939-2 (visited on 06/21/2022).

[174] Daniel Günther et al. "Uncertainties in Snowpack Simulations—Assessing the Impact of Model Structure, Parameter Choice, and Forcing Data Error on Point-Scale Energy Balance Snow Model Performance". en. In: *Water Resources Research* 55.4 (2019). _eprint: https://onlinelibrary.wiley.com/doi/pdf/10.1029/2018WR023403, pp. 2779–2800. ISSN: 1944-7973. DOI: 10.1029/2018WR023403. URL: https://onlinelibrary.wiley.com/doi/abs/10.1029/2018WR023403 (visited on 06/22/2022).

[175] Vincent Vionnet et al. "Multi-scale snowdrift-permitting modelling of mountain snowpack". English. In: *The Cryosphere* 15.2 (Feb. 2021). Publisher: Copernicus GmbH, pp. 743–769. ISSN: 1994-0416. DOI: 10.5194/tc-15-743-2021. URL: https://tc.copernicus.org/articles/15/743/2021/ (visited on 06/22/2022).

[176] Esteban Alonso-González et al. "Daily gridded datasets of snow depth and snow water equivalent for the Iberian Peninsula from 1980 to 2014". English. In: *Earth System Science Data* 10.1 (Feb. 2018). Publisher: Copernicus GmbH, pp. 303–315. ISSN: 1866-3508. DOI: 10.5194/essd-10-303-2018. URL: https://essd.copernicus.org/articles/10/303/2018/ (visited on 06/22/2022).

[177] Jesús Revuelto, Juan Ignacio López-Moreno, and Esteban Alonso-González. "Light and Shadow in Mapping Alpine Snowpack With Unmanned Aerial Vehicles in the Absence of Ground Control Points". en. In: *Water Resources Research* 57.6 (2021), e2020WR028980. ISSN: 1944-7973. DOI: `10.1029/2020WR028980`. URL: `https://onlinelibrary.wiley.com/doi/abs/10.1029/2020WR028980` (visited on 06/22/2022).

[178] Juan Ignacio López Moreno et al. "Instalación y uso de un colchón de nieve para la monitorización del manto de nieve. Cuenca Experimental de Izas (Pirineo Central)". spa. In: *Cuadernos de investigación geográfica: Geographical Research Letters* 36 (2010). Publisher: Universidad de La Rioja Section: Cuadernos de investigación geográfica: Geographical Research Letters, pp. 73–82. ISSN: 0211-6820, 1697-9540. URL: `https://dialnet.unirioja.es/servlet/articulo?codigo=3315346` (visited on 06/22/2022).

[179] J. Ignacio López-Moreno et al. "Intercomparison of measurements of bulk snow density and water equivalent of snow cover with snow core samplers: Instrumental bias and variability induced by observers". en. In: *Hydrological Processes* 34.14 (2020), pp. 3120–3133. ISSN: 1099-1085. DOI: `10.1002/hyp.13785`. URL: `https://onlinelibrary.wiley.com/doi/abs/10.1002/hyp.13785` (visited on 07/19/2023).

[180] Anton Jitnikovitch et al. "Snow water equivalent measurement in the Arctic based on cosmic ray neutron attenuation". English. In: *The Cryosphere* 15.11 (Nov. 2021). Publisher: Copernicus GmbH, pp. 5227–5239. ISSN: 1994-0416. DOI: `10.5194/tc-15-5227-2021`. URL: `https://tc.copernicus.org/articles/15/5227/2021/` (visited on 06/22/2022).

[181] Alain Royer et al. "Review article: Performance assessment of radiation-based field sensors for monitoring the water equivalent of snow cover (SWE)". English. In: *The Cryosphere* 15.11 (Nov. 2021). Publisher: Copernicus GmbH, pp. 5079–5098. ISSN: 1994-0416. DOI: `10.5194/tc-15-5079-2021`. URL: `https://tc.copernicus.org/articles/15/5079/2021/` (visited on 06/06/2023).

[182] Perry Bartelt and Michael Lehning. "A physical SNOWPACK model for the Swiss avalanche warning Part I: Numerical model". In: *Cold Regions Science and Technology* 35.3 (2002). ISSN: 0165232X. DOI: `10.1016/S0165-232X(02)00074-5`.

[183] Michael Lehning et al. "A physical SNOWPACK model for the Swiss avalanche warning Part II. Snow microstructure". In: *Cold Regions Science and Technology* 35.3 (2002). ISSN: 0165232X. DOI: `10.1016/S0165-232X(02)00073-3`.

[184] Michael Lehning et al. "A physical SNOWPACK model for the Swiss avalanche warning Part III: Meteorological forcing, thin layer formation and evaluation". In: *Cold Regions Science and Technology* 35.3 (2002). ISSN: 0165232X. DOI: `10.1016/S0165-232X(02)00072-1`.

[185] Joaquín Muñoz-Sabater et al. "ERA5-Land: a state-of-the-art global reanalysis dataset for land applications". English. In: *Earth System Science Data* 13.9 (Sept. 2021). Publisher: Copernicus GmbH, pp. 4349–4383. ISSN: 1866-3508. DOI: `10.5194/essd-13-4349-2021`. URL: `https://essd.copernicus.org/articles/13/4349/2021/` (visited on 12/13/2022).

[186] S. Procureur. "Muon imaging: Principles, technologies and applications". en. In: *Nuclear Instruments and Methods in Physics Research Section A: Accelerators, Spectrometers, Detectors and Associated Equipment*. Radiation Imaging Techniques and Applications 878 (Jan. 2018), pp. 169–179. ISSN: 0168-9002. DOI: `10.1016/j.nima.2017.08.004`. URL: `https://www.sciencedirect.com/science/article/pii/S0168900217308495` (visited on 06/07/2023).

[187] W. Zeng et al. “Principle study of image reconstruction algorithms in muon tomography”. In: *Journal of Instrumentation* 15.2 (Feb. 2020). Publisher: Institute of Physics Publishing. ISSN: 17480221. DOI: 10.1088/1748-0221/15/02/T02005.

[188] E. Åström et al. “Precision measurements of Linear Scattering Density using Muon Tomography”. In: *Journal of Instrumentation* 11 (2016). DOI: https://doi.org/10.1088/1748-0221/11/07/P07010.

[189] S. Vanini et al. “Muography of different structures using muon scattering and absorption algorithms”. In: *Philosophical Transactions of the Royal Society A: Mathematical, Physical and Engineering Sciences* 377.2137 (2019). Publisher: Royal Society Publishing. DOI: 10.1098/RSTA.2018.0051.

[190] Adam Paszke et al. “PyTorch: An Imperative Style, High-Performance Deep Learning Library”. In: ed. by H Wallach et al. Vol. 32. Curran Associates, Inc., 2019.

[191] Mengyun Guan et al. “A parametrization of the cosmic-ray muon flux at sea-level”. In: (Sept. 2015). URL: http://arxiv.org/abs/1509.06176.

[192] Pablo Martínez et al. “Process monitoring: measurement of the metal–slag interface in furnace ladles”. In: *IAEA TECDOC SERIES. Muon Imaging. Present Status and Emerging Applications* 2012 (2022), pp. 34–35. URL: https://www.iaea.org/publications/15182/muon-imaging.

[193] *MUON CARGO project.* URL: https://muon.systems/en/muoncargo.

[194] *Puertos del Estado.* URL: https://www.puertos.es/en-us/nosotrospuertos/Pages/Nosotros.aspx.

[195] *Geant4, a simulation toolkit.* URL: https://geant4.web.cern.ch/.

[196] Alessandro De Angelis and C Guaita. *Original Wulf electroscope used by Wulf around 1912.* Aug. 2012. URL: https://commons.wikimedia.org/wiki/File:Originalwulf.jpeg%20https://upload.wikimedia.org/wikipedia/commons/1/12/Originalwulf.jpeg.

[197] Alicia López. “Multi-year Campaign of the Gamma-Ray Binary LS I +61 303 and Search for VHE Emission from Gamma-Ray Binary Candidates with the MAGIC Telescopes”. In: (2014), p. 14.